BIOIMAGING WITH PHOTONIC CRYSTAL ENHANCED MICROSCOPY

BY

YUE ZHUO

DISSERTATION

Submitted in partial fulfillment of the requirements
for the degree of Doctor of Philosophy in Bioengineering
in the Graduate College of the
University of Illinois at Urbana-Champaign, 2015

Urbana, Illinois

Doctoral Committee:

Professor Brian T. Cunningham, Chair
Professor William P. King
Assistant Professor Brendan Harley
Assistant Professor Sua Myong

ABSTRACT

The work presented in this dissertation addresses the optimization and application of a newly developed imaging modality, named photonic crystal enhanced microscopy (PCEM) for label-free detection of the surface attached biological samples. Photonic crystal, supporting guided-mode resonances and providing local optical modes, can enhance the light-matter interaction on its surface and thus used for label-free detection and biosensing. One dimensional photonic crystal surfaces are designed and utilized as a biosensor, and further integrated with an ordinary bright-field microscope. To demonstrate the validity of the photonic crystal biosensor, a three-dimensional modeling is developed and evaluated with finite-difference time-domain (FDTD) algorithm to predict and visualize the electromagnetic field redistribution upon the device surface.

Applications of the photonic crystal enhanced microscopy are carried out for live cell imaging, nanoparticle detection and protein-protein binding detection. First, label-free detection for live cell with PCEM imaging system is performed. Three different cellular phenomena are involved in this study, including cell adhesion, cell migration and stem cell differentiation. A novel imaging analysis software is developed to dynamically track the cell plasma membrane evolution. This traction software reveals mass redistribution with high resolution during cell migration which is previously difficult to evaluate quantitatively. Furthermore, both dielectric and metallic nanoparticles are examined and proved to be detectable as label-free detection using PCEM imaging system. Another novel imaging analysis software is developed to automatically count the number of nanoparticles attached on the sensor surface within the imaging field of view.

Finally, a newly developed detection modality for protein-protein binding is demonstrated through PCEM imaging system using nanoparticle as tags. This new detection modality can avoid the photobleach problem and may also hold the potential to detect ultra-low concentrations of protein in the future.

In summary, photonic crystal biosensor and its associated imaging system with microscopy developed in this work show great promise to the label-free biosensing and bioimaging. Future work will extend the application of PCEM to broader research and application fields served as the next generation sensing modalities.

ACKNOWLEDGMENTS

First and foremost, I would like to thank my research advisor, Professor Brian Cunningham, for giving me the opportunity to work on this interesting research topic, and also for his great support and guidance throughout the past years. His wisdom, boundless energy and enthusiasm for research play an essential role for my research and will carry me on in my future work. His patience, devotion and continual encouragement to his students have been truly inspirational to me and helped me achieve my professional goals. I truly appreciate him for making this long journey of PhD study fulfilling and enjoyable as well as making my dream come true.

I am sincerely grateful to my dissertation committee members, Professor William King, Professor Brendan Harley, and Professor Sua Myong. Their deep insight and constructive feedback have been particularly valuable for me in improving and advancing my research work.

Special thanks to my collaborators, Professor William King and Dr. Huan Hu, Professor Brendan Harley and Dr. Sunny Choi, Professor Srikanth Singamaneni and Dr. Limei Tian (in Washington University in St. Louis). I could hardly accomplish my research work without their fully support and great help.

I would like to acknowledge my group members in Nano Sensors Group. Especially, I would like to thank Dr. Meng Lu, Weili Chen, Kenny Long, Hojeong Yu, Meng Zhang, Jui-Nung Liu, Yafang Tan, Tiantian Tang, Chenqi Zhu, and Gloria See for

their suggestions and willingness to endure my questions as well as sharing the lab facilities.

I owe a debt of gratitude to the staff at the Micro and Nanotechnology Laboratory. Gratitude for financial support is due to the National Science Foundation (NSF) and the Center for Innovative Instrumentation Technology (CiiT) at University of Illinois at Urbana-Champaign (UIUC).

And special thanks to my parents and my sister for their belief and endless encouragement during the whole study. Last and most importantly, I would like to thank my husband for his full support and love, and for making possible the completion of my research and dissertation.

TABLE OF CONTENTS

LIST OF ABBREVIATIONS

1D	one-dimensional
2D	two-dimensional
3D	three-dimensional
AFM	atomic force microscopy
AlGaAs	aluminium gallium arsenide
ASC	adipose stem cell
AuNP	gold nanoparticle
AuNR	gold nanorod
CCA	connected components analysis
CCD	charge-coupled device
CTAB	cetyltrimethylammonium bromide
Cy-5	cyanine-5
DI	deionized water
DMEM	Dulbecco's modified eagle medium
DNA	deoxyribonucleic acid
DUV	deep ultraviolet
ECM	extracellular matrix
EDC	1-ethyl-3-(3-dimethylaminopropyl) carbodiimide
EGF	epidermal growth factor
ELISA	enzyme-linked immunosorbent assay
FA	focal adhesion

FAK	focal adhesion kinase
FDTD	finite-difference time-domain
FGF	fibroblast growth factor
FWHM	full width at half maximum
GaAs	gallium arsenide
HAuCl4	chloroauric acid
HEPES	4-(2-hydroxyethyl)-1-piperazineethanesulfonic acid
IgG	Immunoglobulin G
IPA	isopropyl alcohol
kDa	kilodalton
LED	light-emitting diode
LF	label free
LSM	level-set method
LSPR	localized surface plasmon resonance
MARK	mitogen-activated protein kinases
mHAT	mouse hepatocyte-like (cell)
MMSE	minimum mean-square error
mRNA	messenger ribonucleic acid
N2	nitrogen
NA	numerical aperture
NF-κB	nuclear factor kappa-light-chain-enhancer of activated B cells
NHS	N-hydroxy succinimide
NP	nanoparticle

OD	optical density
PBS	phosphate buffered saline
PC	photonic crystal
PCEF	photonic crystal enhanced fluorescence
PCEM	photonic crystal enhanced microscopy
PDMS	polydimethylsiloxane
PET	poly (ethylene terephthalate)
PIV	peak intensity value
PML	perfectly matched layer
PS	polystyrene
PWV	peak wavelength value
Q	quality factor
RCWA	rigorous coupled-wave analysis
RI	refractive index
RIU	refractive index unit
RLE	run-length encode
RNA	ribonucleic acid
RPMI	Roswell Park Memorial Institute (cell media)
SA	streptavidin
SEM	scanning electron microscope
SH-PEG-COOH	heterobifunctional polyethylene glycol
Si3N4	silicon nitride
SiO2	silicon dioxide

SPR	surface plasmon resonance
SPRi	surface plasmon resonance imaging
Src	proto-oncogene tyrosine-protein kinase sarcoma
tDPN	thermal Dip-Pen Nanolithography
TE	transverse electric
TEM	transmission electron microscopy
TiO2	titanium dioxide
TIRF	total internal reflection fluorescence
TM	transverse magnetic
TNF-α	tumor necrosis factor α
UV	ultraviolet
UVCP	ultraviolet cured polymer

CHAPTER 1

INTRODUCTION TO LABEL-FREE IMAGING AND PHOTONIC CRYSTAL BIOIMAGING

In this chapter, we present the motivation for this work. The need for accurate imaging tool stems from live cell imaging and biomarker detection problems. Both these aspects, when addressed using currently existing methods, suffer from limitation hindering their practical use. The goal of this work is to propose and validate a simple yet versatile imaging modality able to overcome these limitations. We first describe the motivation in the context of live cell imaging as well as biomarker detection. Then, we review existing imaging methods, focusing on label-free approaches. Finally, we provide an outline of the work presented here.

1.1 Motivation

1.1.1 Live Cell Imaging

Live cells are integrated not only structurally, but also functionally with their surrounding extracellular matrices (ECMs) in highly organized processes, which may be dynamically involved with thousands of proteins [1-4]. The complex interaction between cell and the ECM molecules is essential to regulate and mediate various cellular procedures, including cell adhesion, cell migration, and stem cell differentiation, etc. For instance, integrin [2], a type of transmembrane receptor, can cluster in some specific cell-ECM adhesion sites (so called focal adhesions) to provide a dynamic link between the intracellular and extracellular environments. Reorganization of the intracellular

cytoskeletal and ECM proteins enables signals (e.g. biomechanical, biochemical) to be propagated across the cellular membrane [5-12]. In this section, we review the cell-matrix interactions involved in the formation of cell adhesion, migration, and stem cell differentiation to potential future therapeutic approaches.

Cell adhesion has been a popular research topic in the past several decades, mainly focusing on the binding of a cell to a substrate/surface, such as an extracellular matrix (ECM) or another cell [13-15]. It is critical for a live cell to utilize the cellular adhesion for maintaining its multicellular structure and function. Even though cell adhesion is a dynamic structure, it can withstand and exert forces on the ECM during a certain life time. A molecular complex at the cell focal adhesion (FA) site can gather over hundreds of different types of adhesion molecules, such as Src, FAK, talin, etc[16-18]. The cell adhesions connect cell cytoskeleton to ECM molecules through transmembrane proteins and may stimulate downstream signal transductions. Therefore, cell adhesions are one kind of mechanosensitive elements, which convert mechanical stimuli into biochemical responses by sensing and responding to environmental parameters (such as matrix components or rigidity). Due to the complexity of the cell adhesion process, the underlying mechanisms of cell–ECM or cell-cell adhesions remain unclear.

Cell migration generally refers to the surface/substrate attached cells movement to a different location with crawling or blebbing motility [19-22]. The speed of cell migration is relatively slow, normally around a few um/minutes for cultured ordinary cells. Cell migration is a coordinated process of cellular membrane protrusions that regulated by the turnover of disassembly and reassembly of cell focal adhesion and the

dynamics formation of actin filaments in the migration frontier [20, 23]. The traction forces are generated during this complex process by the activity of motor proteins (such as myosin) for cells to seize on the ECM molecules and move the whole cell body [24]. External stimuli from the surrounding environment can influence cell migration via intracellular biochemical signals transduced into the cytoskeleton network through the interactions of transmembrane proteins with ECM molecules [25]. During migration, the morphological features of moving cells can vary significantly[26]. For example at one extreme, round and highly protrusive or blebbing cells (such as lymphocytes and cancer cells in some environments) can migrate with high speed using weak adhesions [27, 28]. On the other hand, highly spread cells (such as fibroblasts and endothelial cells) have many large and strong adhesions and migrate relatively slowly, while their migration is often referred to as being mesenchymal [29]. In reality, both the external factors, such as substrate compliance or dimensionality, and intrinsic factors, such as the contractility of the cells, can alter the migration modes. Therefore, understanding the mechanism of cell migration and the influencing factors is essential to the development strategies of many novel therapeutic methods, and may impact tissue repair, stem cell therapeutics, cancer metastasis preventing, as well as drug development, just to name a few.

Stem cells have the ability to generate mature cells with a type of specific tissue through differentiation and also have the ability to perpetuate themselves through self renewal [30-35]. Stem cell differentiation is a critical process for development of multicellular organism and can occur during embryonic development, wound healing, or cancer development, etc. Cellular differentiation is a transition from one pattern of gene expression switching to another one and thus is regulated by the gene regulatory network.

A cascade of signaling events, often initiated from the extracellular environment and propagated through the transmembrane molecules and cytoskeletons, can influence the cell differentiation fate [36-39]. Once the signal reduction triggers the cellular differentiation, a series of dramatic changes in the cell will occur, such as gene expression, morphology, metabolic activity, etc. However, the cellular differentiation and the regulation signal network are complex processes highly evolving through with changes in the environment and are still largely unknown. Therefore, understanding the cellular differentiation process as well as the regulation factors holds great promise for the future of regenerative and translational medicines.

1.1.2 Cancer Biomarker Detection

Each year, more than ten million people are diagnosed with cancer globally [40]. Although there has been significant progress in understanding and treatment of cancer over the past decades, cancer still causes more than five million deaths (more than 10% of all human deaths) every year and thus remains one of the highest death-rate diseases. One reason causing the high death-rate of cancer is late diagnosis, since cancer grows uncontrollably from the inner part of the organs and cannot be efficiently recognized by the human body immune system. In an advanced cancer development stage, cancer cells often invade surrounding tissues and can also metastasize from the primary site to other parts of the body.

Every cell type, including cancer cell, has a unique molecular signature (referred to as biomarkers) [40-44]. Through secretion, cancer cells may release many DNA, RNA, proteins, lipids, or other macromolecules into the extra-cellular fluid in the human body.

Some of these released products, often in very low concentrations, can end up in the bloodstream circulation and hence serve as potential serum biomarkers. The cancer biomarkers contain useful information on most of the physiological process in cancer cells, cancer tissue microenvironment and cancer cell-host interaction, and the level and activities of cancer biomarkers in blood circulation are identifiable with different features at different development stages. Therefore, cancer biomarker can be an important biological indicator of cancer status and progression for the physiological processes of the cancer cell or tissue (such as disease-related biomarkers), or pharmacological responses to a clinic therapeutic intervention (such as drug-related biomarkers).

Despite growing research and fruitful achievements in cancer therapy, nearly half of people who had received treatment for invasive cancer died from cancer or the treatment each year. It is well known that the chance of being cured of cancer increases with earlier cancer detection and treatment. Nowadays, however, only a few cancer biomarkers are available to evaluate and stage cancer in routine clinical practice, although there are many notable accomplishments in the research field of cancer biomarker detection [45-48]. One major factor preventing routine clinical evaluation is the difficulty to detect cancer biomarkers due to their low concentration in the blood stream and their high variability across individuals. Consequently, it causes low sensitivity as well as low prognostic and predictive value in biomarkers detection methods [49]. Thus, there is a great need to develop high sensitivity and inexpensive method to detect the circulating cancer biomarkers.

1.2 Label-free Imaging

The imaging contrast of a live cell without labeling under a conventional bright-field microscope is infinitesimal since the effective refractive index of a normal live cell is about 1.35~1.37, while that of water (as background) is 1.33 in the wavelength range of visible light. Therefore, labels employing dyes or fluorescence have been used to enhance visualization of detecting the presence of a particular biomolecule or cell to which the biomarkers are conjugated. These labeling methods for detecting biomolecules or cells are powerful and are supported by standardized infrastructure across industries. In addition, dielectric-based devices have also been used in an attempt to improve the detection sensitivity. For instance, total internal reflection fluorescence (TIRF) is a well-established technology in which light is coupled into a waveguide and thus fluorophores can be excited within the evanescent field on the device surface [50-52]. The incident light can be incoupled with a grating or a prism and then propagated along the waveguide through total internal reflection, where the biological sample placed on the top side of the waveguide functions as the cladding. TIRF-based microscopy can selectively visualize the cell-matrix interface with high axial resolution since it only excites the fluorophores within the evanescent field on the device surface, and thus diminishes the background fluorescence which would otherwise scatter and absorb signal from other components in the cellular media. Therefore, the signal-to-noise ratio of the TIRF microscopy can be significantly improved with inherent spatial discrimination.

In spite of its widespread use, labeled detection has several inherent drawbacks caused by the natural properties and physical linking of the label itself. For example,

labels can possibly block the binding sites of the probe or target proteins, modify analyte conformation, and induce steric hindrance in molecular detections. Labels can also be toxic in live cell imaging and intrinsically alter cell behaviors, functionalities or signal pathways. Moreover, fluorescent tags are subject to quenching and can be photobleached very quickly, which may cause difficulty to provide long-term kinetic information. In addition, finding and producing an appropriate label which can function stably and uniformly across a biosystem can be costly and tremendously time consuming [53]. Therefore, although it is challenging, eliminating the label from the detection assays while still maintaining the high sensing sensitivity is the ultimate vision in the research field of bioimaging and detection, since it will provide noninvasive probing, improve the detection accuracy, limit conformation modifications and provide long-term kinetic information.

1.2.1 Label-free Biosensor

Label-free biosensors are an emerging class of biosensing and detection methods [54]. Namely, the molecules of interest in label-free detection are not labeled or altered and thus can be detected in their natural forms. Label-free detection can quantitatively reveal the binding affinity, specificity, and long-term kinetics of the biological elements. Label-free detection can be implemented in schemes that utilize a transducer to probe some properties of the interested analyte, such as electronic charge which can be determined by field-effect transistor-based or electrochemical sensors, mass which can be measured by piezoelectric or surface acoustic wave devices, or dielectric permittivity which can be sensed by evanescent optical fields [55, 56].

Label-free optical biosensors are especially attractive since the biochemical interactions can be interrogated from afar (as long as within the detection zone) without any direct physical connection to the optical sensor itself, which provides flexibility for sensor formats and enables the use of large sensor arrays [57-59]. Fundamentally, the sensitivity of a label-free optical biosensor is determined by the strength of the light-matter interaction atop of the sensor surface. Generally, electromagnetic evanescent fields are generated on the top of label-free optical biosensors and form the active detection zone. They can be utilized to examine the interaction of the light with the absorbed biomolecules. A change of the dielectric permittivity caused by the biological elements within the detection zone, e.g. surface attachment of proteins or cells, will lead to a corresponding variation in the resonance wavelength or intensity of the reflected or transmitted light. The exponential decay of the evanescent fields results to a penetration depth of around 200 nanometers in the active detection zone atop of the optical sensor surface. The resulting scheme of near-surface detection is indeed ideal for monitoring the interactions of biological elements at the transducer surface, including nucleic acids, proteins, cell-ECM, while minimizing the bulk solution interferences. Besides, the optical transducer has no inherent selectivity, while the sensing selectivity is provided by the surface chemistry or capture biomolecules immobilized atop the sensor surface. This supplies a broad application range for label-free optical sensor which can be used for most of the biomolecules or live cells.

1.2.2 Surface Plasmon Resonance Biosensor

Among many other optical sensing modalities, including resonant mirrors and ellipsometry, surface plasmon resonance (SPR) is the most popular and widely studied label-free optical sensing technique [60-63], which was first demonstrated for biosensing by Liedberg et al. in 1983 [64]. The surface plasmons, which are resonant oscillations of the free electrons at the interface between dielectric and metal materials (e.g. gold), can be excited when polarized incident light is diffracted at the angle of total reflection. The total reflection angle relies on the refractive index of the surrounding media within the decay length of that electromagnetic evanescent wave. When the wave vector of the incident light matches that of the surface plasmon, the energy extraction appears as a depression in the reflected spectrum at a given wavelength and incident angle. Therefore, the target analyte can be sensed in real time by interacting with the incident light, modifying the dielectric permittivity and correspondingly the excitation conditions of the surface plasmon atop of the metallic layer. SPR is a very powerful tool though it also has limitations, such as the cost of the system and its complexity (due to the need for precision optical and alignment components). Besides, SPR-based biosensing and bioimaging methods may suffer from the broad spectral width due to the intrinsic property of the metal plasmon resonance which leads to low spectral resolutions in biosensing. Moreover, the large lateral propagation of surface plasmons (e.g. generally on the order of 100 μm) may restrict the spatial resolution of the SPR-based imaging.

1.2.3 Photonic Crystal Biosensor

A novel photonic crystal optical biosensor has recently been demonstrated for label-free detection of biochemical interactions [65-72]. Photonic crystal is a periodic

multi-layer dielectric structure with optical properties that vary with sub-wavelength periodicity in one, two, or three dimensions. Photonic crystal biosensor demonstrates a narrow-band reflection with nearly100% reflection efficiency at the resonance wavelength. It also exhibits a strong optical confinement of incident light into an infinitesimal volume and thus enables the detection in nanometer scales.

Photonic crystal biosensor has been utilized to detect surface attached biological analyte and exhibited a high detection sensitivity for mass density and a large dynamic range [73]. In addition, photonic crystal sensor has also been employed to detect gas, temperature, pressure, stress and humidity, to name a few. Materials commonly utilized for photonic crystal fabrication are heteropitaxial layers (e.g. AlGaAs/GaAs), III-nitride compound layers or dielectric layers (e.g. Si3N4, TiO2, SiO2). Recently, organic compounds and polymers (e.g. UV curable polymers) have attracted much attention due to the simple and low cost fabrication processes and capability for mass-scale production. Moreover, photonic crystal biosensors can be incorporated into standard microplates (e.g. 96-well microplate) for compatibility with existing fluid handling systems as well as high throughput, multiplexing detection system. In summary, photonic crystal biosensor has demonstrated great promise as the next generation biosensing technique.

1.3 Research Outline

The ultimate goal of this research is to develop and utilize photonic crystal enhanced microscopy system for biosensing and bioimaging, including detection of live cell, nanoparticle and protein-protein interaction. Chapter 2 describes the fundamental physics and design of the photonic crystal biosensor followed with a computer-based

modeling, as well as characterization of the biosensor. The working principle of the photonic crystal enhanced microscopy system for bioimaging is also introduced in this chapter. Label-free imaging for live cell with photonic crystal enhanced microscopy, including cell adhesion, cell migration, and stem cell differentiation, is addressed in Chapter 3. This chapter also describes the imaging analysis software which was developed to study the spatiotemporal dynamics of cell boundary evolution during migration. Chapter 4 explores the label-free detection for nanoparticles with photonic crystal enhanced microscopy. This work is extended in Chapter 5 and a novel detection method utilizing the nanoparticles as tags to probe the protein-protein interactions is introduced in this chapter. Finally, Chapter 6 summarizes the thesis and provides the future outlook for this research.

CHAPTER 2

PHOTONIC CRYSTAL ENHANCED MICROSCOPY

This chapter describes the photonic crystal imaging used in this work. As mentioned previously, photonic crystal has advantages when compared to existing label-free methods, specifically higher spectral resolution and potentially higher spatial resolution (because of the lesser amount of lateral propagation). This makes photonic crystal imaging a promising candidate to achieve our goals in imaging of both live cells and protein-protein binding. This chapter first briefly introduces the historical background for photonic crystal microscopy. Then, we describe the optics theory necessary to understand the biosensor. Further, we present the basics of photonic crystal biosensor, including the periodic subwavelength grating structure, its effect on guided-mode wave propagation, as well as the photonic crystal biosensor modeling. Finally, the actual design and fabrication of the biosensor and the development of photonic crystal based imaging system are discussed.

2.1 Introduction

Anomalies in periodically modulated nanostructures, initially discovered by Wood in 1902 [74] as an anomalous interaction of light with dielectric gratings structures, have attracted much attention in the last several decades. The structures of resonant anomalies in waveguide gratings had later been demonstrated with a subwavelength modulation in refractive index along one dimension [75, 76]. This nanostructure can function as optical filters producing complete exchange of energy

between bi-directional propagating diffracted waves with arbitrarily low line widths and smooth line shapes [77]. This guided-mode resonance is a result of possible guided modes propagating with a periodic modulation, which allows phase-matching of externally incident radiation into modes that can be re-radiated into free space. Lately, guided-mode resonances have also been shown in 2D photonic crystal (PC) slabs [78-80] and crossed gratings [81, 82].

Photonic Crystal (PC) biosensors have recently been demonstrated as a highly versatile technology for a variety of label-free assays including high-throughput screening of small molecule–protein interactions, characterization of protein–protein interactions, and measurement of cell attachment modulation by drugs [53, 65-71]. A PC biosensor is a sub-wavelength grating structure consisting of a periodic arrangement of a low refractive index material coated with a high reflective index layer. By measuring the resonant peak wavelength value (PWV) on a pixel-by-pixel basis over a PC surface, an image of cell or protein attachment density may be recorded. PWV images of the PC may be gathered by illuminating the structure with collimated white light through the transparent substrate, while the front surface of the PC is immersed in aqueous media. The advantages of PC-based surfaces for cell or protein attachment imaging are compelling. As a label-free technology, cell or protein attachment to a PC sensor is measured without the use of dyes or stains, so a population of cells or proteins can be measured repeatedly without disrupting their culture environment. The detected output signal is highly quantitative, providing measurements that are repeatable between sensors, instruments, and laboratories without photobleaching.

PC biosensors can be fabricated from inexpensive materials and require only low intensity illumination from beneath the sensor, and there is no need for electrical or physical contact between the sensor and the detection system. Besides, the PC biosensors can be utilized in a reflection mode, so the illumination light does not pass through the cell body, the cell media, or the liquid–air meniscus of a microplate well. Therefore, it efficiently avoids the scatter problem which could happen in transmission mode. Furthermore, the PC biosensor strictly limits lateral propagation of resonantly coupled light, enabling imaging-based detection with resolution sufficient for measuring subtle variations in cell adhesion strength within a single cell, without needing to pre-tune the sensor to a particular resonant coupling condition, as in Surface Plasmon Resonance imaging (SPRi). In summary, PC biosensor imaging provides information that is fundamentally different than that provided by conventional optical microscope, as the sensor responds to local variation in cell or protein attachment strength to the transducer surface. The sensor can be prepared with a variety of surface functionalizations (such as matrix coatings, antibodies, and peptides) and thus can be used as a tool for measuring how cell or protein attachment to surfaces is modulated by drugs, growth factors, or other environmental factors.

This chapter describes the theoretical background and the development of the photonic crystal biosensor used in this work. As discussed earlier, existing biosensors aiming at imaging nano-structures as well as live cells face limitations hindering their practical use. Label-based such as fluorescence imaging is degraded by the photobleaching effect and limits the length of imaging sessions (which prevents the study of medium-to-large time scale mechanism. Methods based on optics can address these

issues, but are also limited by imaging contrast and sensitivity. In order to circumvent the limitations of existing biosensors, our lab previously developed a Photonic Crystal Enhanced Microscopy (PCEM) [66, 83] which is used as a foundation for this work.

2.2 Photonic Crystal Biosensor

2.2.1 Physics of Photonic Crystal Biosensor

A photonic crystal biosensor, as shown in Figure 2.1, has a grating structure in a sub-wavelength range of the illumination light. The sensor consists of a periodic grating of a low refractive index material coated with a high refractive index layer, while the grating and the high index guidance layer are the key components. The grating enables phase matching of external radiation to the modes supported by the photonic crystal, and symmetrically gives rise to the leaky nature of these modes by enabling re-radiation of the confined light. When the PC is illuminated with a broadband light source at normal incident angle, high order diffraction modes couple light into and out of the high refractive index layer, destructively interfering with the zeroth-order transmitted light. For off-normal incident light, a single order couples to a single leaky mode. This phenomenon can be observed in far field as a significant dip in transmission or a peak in reflection for illumination wavelengths and angles that satisfy the resonance condition:

$$\frac{2\pi}{\lambda}\sin(\theta) \pm m\frac{2\pi}{\Lambda} = \beta, \tag{1-1}$$

where λ and θ represents the wavelength and illumination angle of the incident light, respectively; m denotes the diffraction order of the modes; Λ describes the period of the grating structure; and β is the real part of the propagation constant of the guided

mode. Phase matching by the periodic structure to the reflected and transmitted zeroth orders enables extraction of energy from the leaky waves. At a particular resonant wavelength and incident angle, complete interference occurs (no light is transmitted) and it yields a sharp resonant reflection peak with nearly 100% reflection efficiency.

The spectral location of peak reflection, named resonant wavelength, can be modulated by the addition of biomaterial upon the PC surface within the range of the strongly confined electric field (evanescent field). Hence, bulk refractive index variation of the medium atop the sensor surface will result in a shift of the resonance wavelength to a higher wavelength, as will any thickness or density changes of a surface-bound biomolecular layer. Thus, photonic crystal biosensor enables quantitative measurement of molecular adsorption or conformation change in the evanescent field at the sensor interface by converting the nanoscale changes into a readily detectable optical signal.

The electromagnetic standing wave that is generated at the PC surface during resonant light coupling inhibits lateral propagation, thus enabling neighboring regions on the PC surface to display a distinct resonant wavelength that is determined only by the density of biomaterial attached at that precise location. By measuring the resonant peak wavelength value (PWV) on a pixel-by-pixel basis over a PC surface, an image of biomaterial (such as cell or protein) attachment can be acquired. PWV images of the PC can be acquired by illuminating the structure with low intensity collimated broadband light (through the transparent substrate), while the front surface of the PC biosensor can be immersed in aqueous media.

2.2.2 Photonic Crystal Biosensor Modeling

To predict the local reflectance spectrum and to visualize the distribution of

electromagnetic fields on PC surface, we applied the Lumerical Finite Difference Time Domain (FDTD) [84] computer simulations of the PC structure (Figure 2.2). Two periods of the device are simulated, with periodic boundary conditions applied to the perpendicular to the grating structures. Using the physical dimensions of the fabricated device to specify the modeled structure, FDTD predicts a resonant reflection wavelength of $\lambda = 620$ nm and a reflection efficiency I = 96%. This result can guide the design of the PC and gives an estimate of the expected contrast that can be observed in the conditions of the simulation.

2.2.3 Photonic Crystal Biosensor Fabrication

The PC sensors used in this study can be fabricated using a low-cost nanoreplica molding approach (Figure 2.3) that has been described previously. Briefly, a silicon wafer molding template with a negative volume image of the desired PC grating structure (period = 400 nm, depth = 120 nm) was fabricated using deep-UV lithography and reactive ion etching. Liquid UV-curable epoxy was pressed between a glass cover slip (0.17 mm thick) and the silicon wafer, and was subsequently cured to a solid using a high intensity UV lamp. The hardened epoxy preferentially adhered to the glass substrate and was peeled away from the silicon wafer, leaving a replica of the silicon mold. A thin TiO2 layer (t ~ 60 nm) was deposited via reactive RF sputtering (PVD 75, Kurt Lesker) providing the high-refractive index coating. Figure 2.4 presents a scanning electron micrograph of the replica-molded sensor after dielectric coating that shows excellent uniformity across the PC surface. The grating height is ~60 nm and the roughness on PC surface is 4.3 nm ± 1.0 nm (top) and 6.6 nm ± 1.4 nm (gap between the teeth) for an area of 100 nm × 100 nm, as measured by atomic force microscope (AFM). The PC is

designed to resonantly reflect a wavelength of $\lambda \sim 620$ nm, when covered by aqueous media.

2.2.4 Photonic Crystal Characterization

The ability of the PCEM to measure peak shifts of the resonance wavelength in the bulk refractive index of the cell media was performed to calibrate for cell attachment demonstrations. The PC surface was exposed to deionized (DI) water (n = 1.333) and subsequently exposed to isopropyl alcohol (IPA) (n = 1.377). The individual pixel atop PC surface in a PWV image demonstrates high reflection efficiency and narrow resonant reflection bandwidth, and the PWV shift yielded a bulk refractive index sensitivity of $\Delta l/\Delta n$ = 102 nm/RIU (refractive index unit). With the PC surface exposed to cell media (Ham's F12 media, Invitrogen) in a PDMS well attached on the PC under mammalian cell culture condition (T = 37 ºC and 5% CO2), a series of PWV images were acquired over a 12 hour period to demonstrate PWV stability. The average PWV shifted about 0.12 nm over 12 hours, and the standard deviation of PWV within an image (512×512 pixels) of a PC was 0.09 nm.

2.3 Principle of Photonic Crystal Enhanced Microscopy (PCEM)

A schematic diagram and a photo of the PCEM instrument are shown in Figure 2.6 and 2.7, respectively. The system is built upon the body of a standard inverted microscope (Carl Zeiss Axio Observer Z1). In addition to ordinary bright field imaging, a second illumination path is provided from a fiber-coupled broadband light-emitting diode (LED) (Thorlabs M617F1, 600 < I < 650 nm). The fiber output is collimated and filtered by a polarizing beamsplitter cube to illuminate the PC with light that is polarized with its electric field vector oriented perpendicular to the grating lines. The polarized beam is

focused by a cylindrical lens (f = 200 mm) to form a linear beam at the back focal plane of the objective lens (10× or 40×, Zeiss). After passing through the objective lens, the orientation of the line-shaped beam is rotated to illuminate the PC from below at normal incidence. The reflected light is projected, via a side port of the inverted microscope and a zoom lens (1.6×), onto a narrow slit aperture at the input of an imaging spectrometer. The width of the adjustable slit was set to 30 nm for the work reported here. Using this method, reflected light is collected from a linear region of the PC surface, where the width of the imaged line, 1.2 μm, is determined by the width of the entrance slit of the imaging spectrometer and the magnification power of the objective lens. The system incorporates a grating-based spectrometer (Acton Research) with a 512×512 pixel CCD camera (Photometrics Cascade 512). The line of reflected light, containing the resonant biosensor signal, is diffracted by the grating within the spectrometer (300 lines/mm) to produce a spatially resolved spectrum for each point along the line. Therefore, each pixel across the line is converted to a resonant reflection spectrum (Figure 2.8 (a)), containing a narrow bandwidth ($\Delta\lambda \sim 4$ nm) reflectance peak from the PC.

The PWV of each peak is determined by fitting the spectrum to a second order polynomial function, and then mathematically determining the maximum wavelength of the function. By fitting all 512 spectra, in a process that takes 20 ms, a line comprised of 512 pixels is generated that represents one line of a PWV image of the PC surface (Figure 2.8(b)). With a 10× objective lens and an effective magnification of 26×, each pixel in the line represents a ~0.6 μm width on the PC surface and 512 such pixels cover a total width of ~300 μm (x dimension). To generate a two-dimensional PWV image of the PC surface, a motorized stage (Applied Scientific Instruments, MS2000) translates the sensor

along the axis perpendicular to the imaged line (y dimension) in increments of 0.6 μm/step. Using this technique, a series of lines are assembled into an image (Figure 2.8 (c)) at a rate of 0.1 sec/line and the same area on the PC surface can be scanned repeatedly. Each image is comprised of 512 by n pixels, where n can be selected during each scan session, and each pixel represents a $0.6 \times 0.6\ \mu m^2$ region of the PC surface. A biosensor experiment involves measuring shifts in PWV and/or shifts in the resonant Peak Intensity Value (PIV).

2.4 PCEM System Optimization

The system developed reported in [66, 83] has been improved as part of this work in order to adapt to the new type of applications. We list here some of these improvements and how they pertain to specific imaging tasks.

2.4.1 Fast Acquisition Software

In order to allow for dynamic acquisition of live cells, the imaging software had to be accelerated. The existing system was limited to acquiring a single frame per minute, which limits the ability to image live cells with sufficient frequency to observe displacement and attachment (these phenomena are best observed with a time period on the order of seconds between frames). A few additions to the existing software were included to the existing code in order to reduce acquisition time:

1) The data format on disk was changed from text to binary. With pixel values on the order of 10^5 (5 digits), using a binary format reduces the size of the output files written to disk (by a factor 2 to 3) thus accelerating file writes and does not require extra conversions (although this effect is minimal).

2) Typical scans using the existing software were performing image acquisition (using the line scan approach described earlier), then waiting for the current frame to be written to disk before continuing with the scan. The write time can be overlapped with acquisition of the next frame by using a double buffered system. As described on Figure 2.9, the system starts with both buffers empty and requests a buffer whenever a frame is to be acquired. As soon as a line scan is terminated, a trigger is sent to a writer thread responsible for generating the output file. In the mean time, if the second buffer has been written to disk, it can be used to acquire the next frame instantaneously.

3) Finally, the software has been augmented to allow for imaging of multiple regions of interest within the field of view. Instead of performing a large scan of the whole field of view (512^3 samples), acquisition time can be reduced by scanning a few subregions with less samples.

2.4.2 Combining Bright-field Imaging

In order to visualize simultaneously PC spectra images and bright-field images, the imaging acquisition software was augmented to control a separate bright-field camera. Illumination for this bright-field camera originates from a different light path, which is also controlled by the imaging acquisition software. PC spectra scans and bright-field scans are interleaved for each frame. The bright-field imaging can be useful for confirmation of the cell existence, position or morphology change.

The bright-field image is taken by a separate camera in an independent output light-path, tuning by a rotation wheel with mirrors rotating between the label-free

imaging light-path and bright-field light-path. The bright-field imaging can be useful for confirming the cell status during dynamic detection of live cell imaging. The bright-field acquisition was absent from the original software and thus had to be implemented and integrated into the acquisition software (in C # language). The acquisition sequence is setup as follows: first a label-free image is acquired using a line scan (with the imaging stage moved line by line); then the imaging stage moves back to the center of the field of view; the reflector is closed to block the strong light from LED; the rotation wheel is tuned to the bright-field imaging light-path; finally the bright-field imaging camera takes a bright-field image. To prepare for the next acquisition, the rotation wheel is turned back to the label-free light-path. The series of label-free images and bright-field images can be taken sequentially.

2.5 Figures

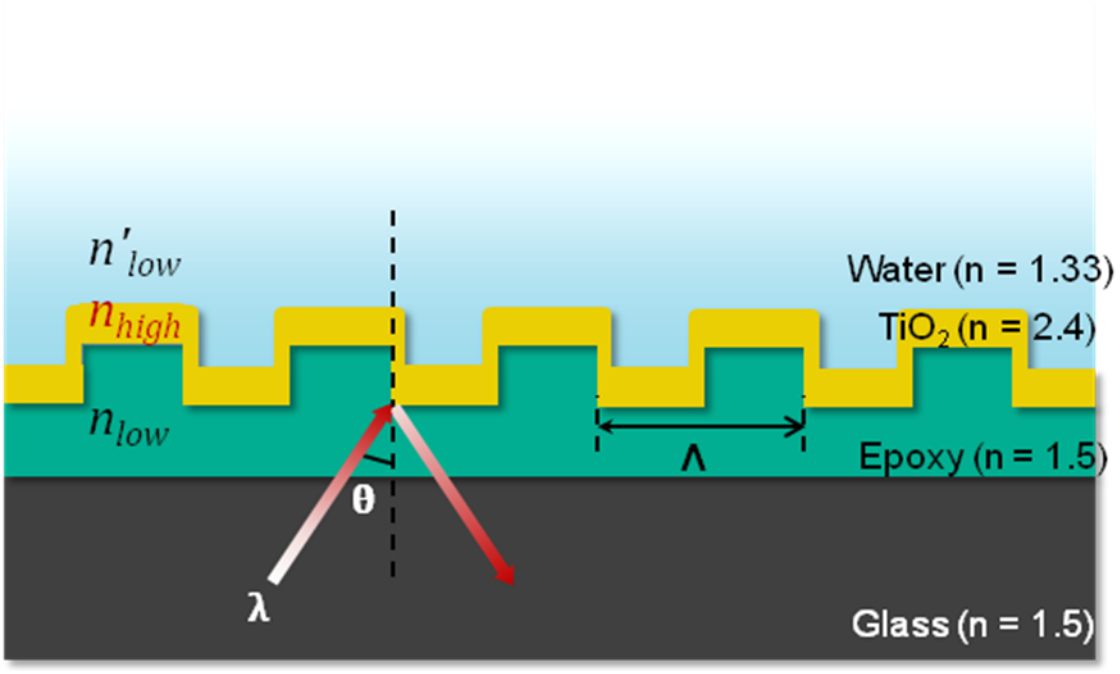

Figure 2.1 Schematic Diagram of Photonic Crystal Biosensor.

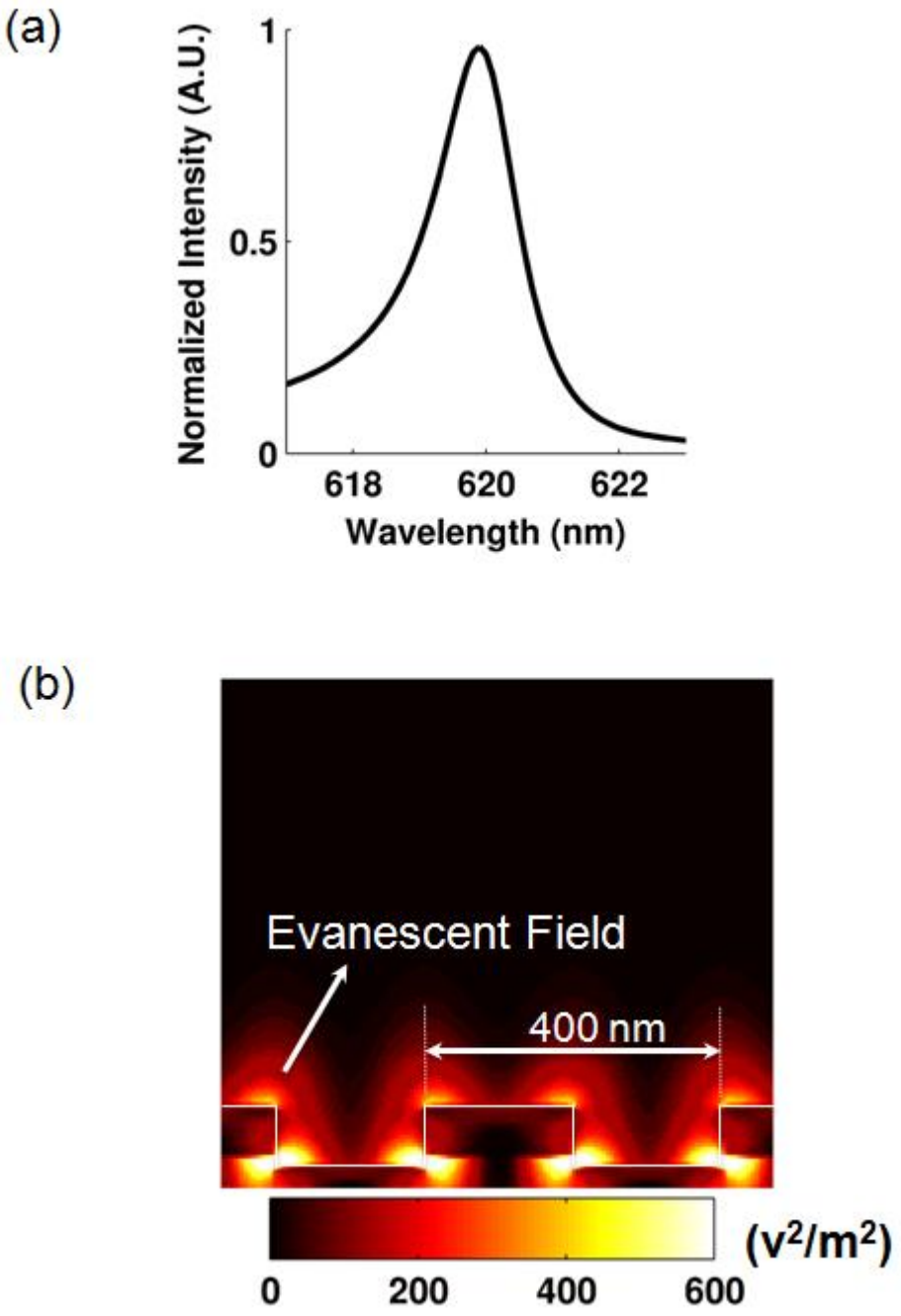

Figure 2.2 Computer simulations with FDTD of (a) reflection and (b) near field electric-magnetic distributions of photonic crystal surface.

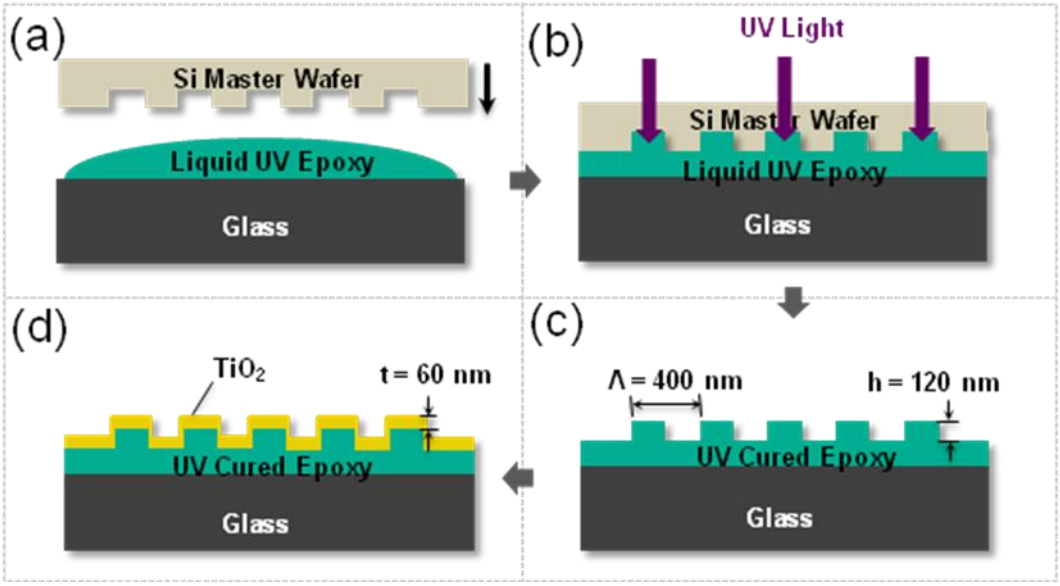

Figure 2.3 PC Biosensor Fabrication Process. (a) The process begins with depositing a thin layer of liquid UV epoxy polymer between a Si wafer template and a glass substrate. (b) The epoxy is converted to a solid with UV light exposure. (c) The template is peeled away and the grating pattern is transferred to the glass. (d) A thin layer of sputter-deposited TiO2 film is applied over the grating structure. (e) Scanning electron micrograph of the PC surface. Inset: Zoomed in tiled SEM image. (f) Photo of a PC fabricated on a glass cover slip.

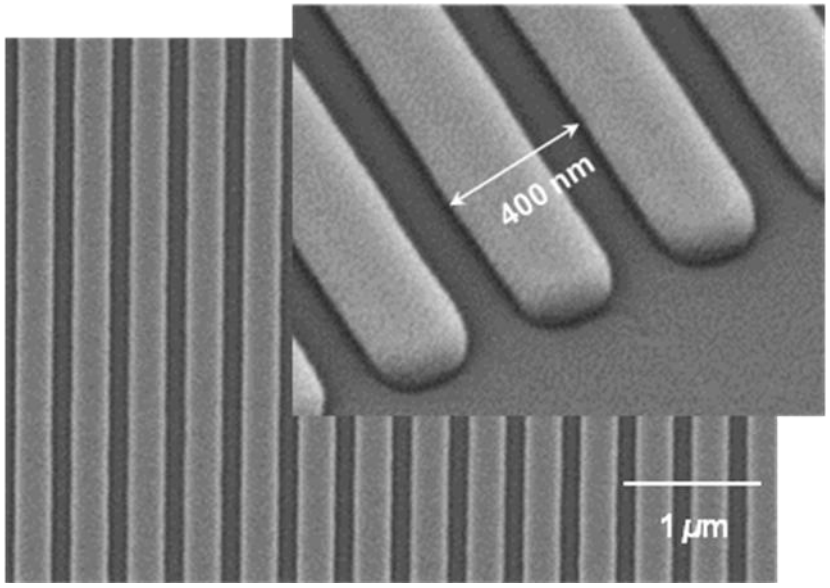

Figure 2.4 Scanning electron micrograph of the PC surface. Inset: Zoomed in tiled SEM image.

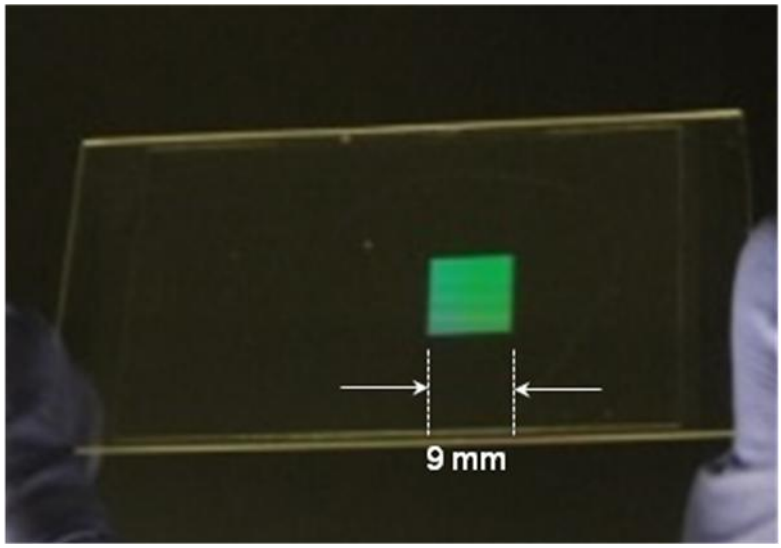

Figure 2.5 Photo of a photonic crystal biosensor fabricated on a glass cover slip.

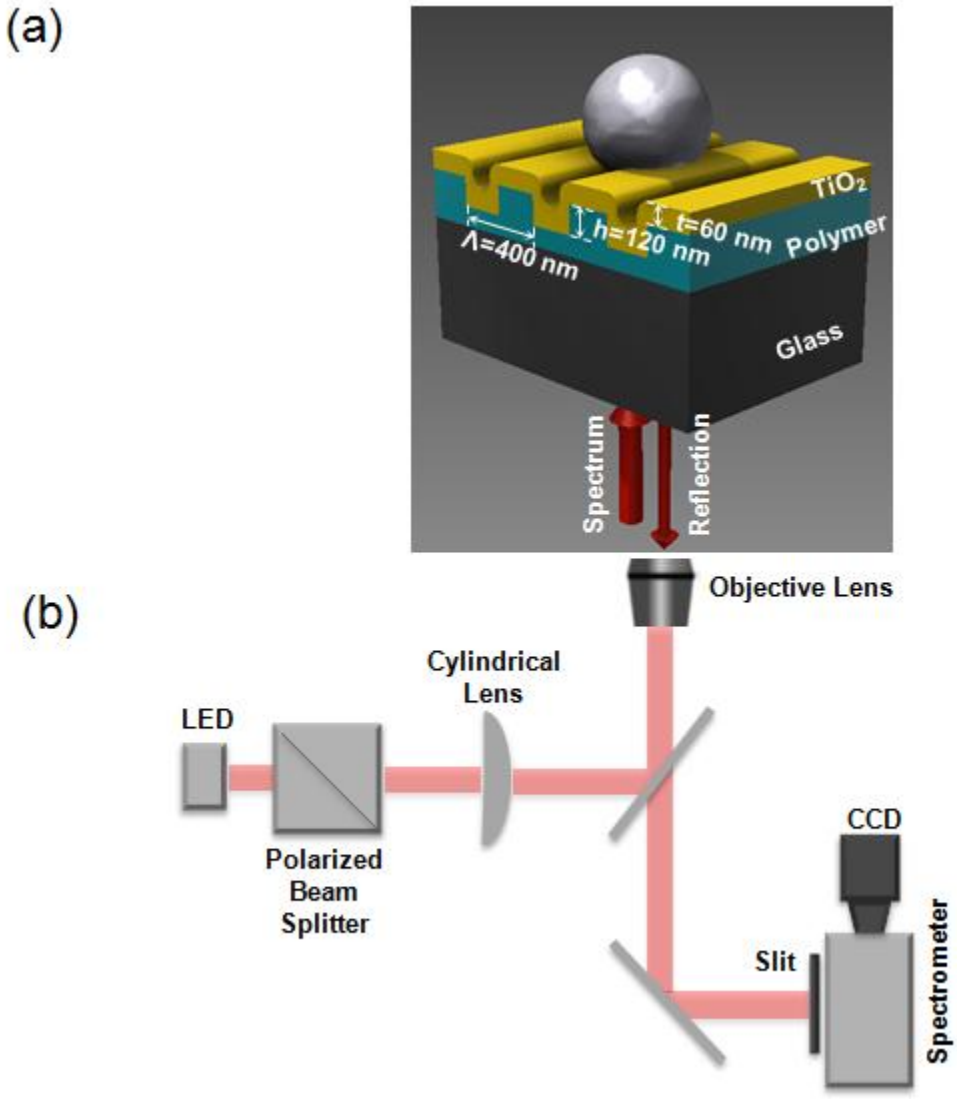

Figure 2.6 Instrument schematic of the photonic crystal enhanced microscopy (PCEM).

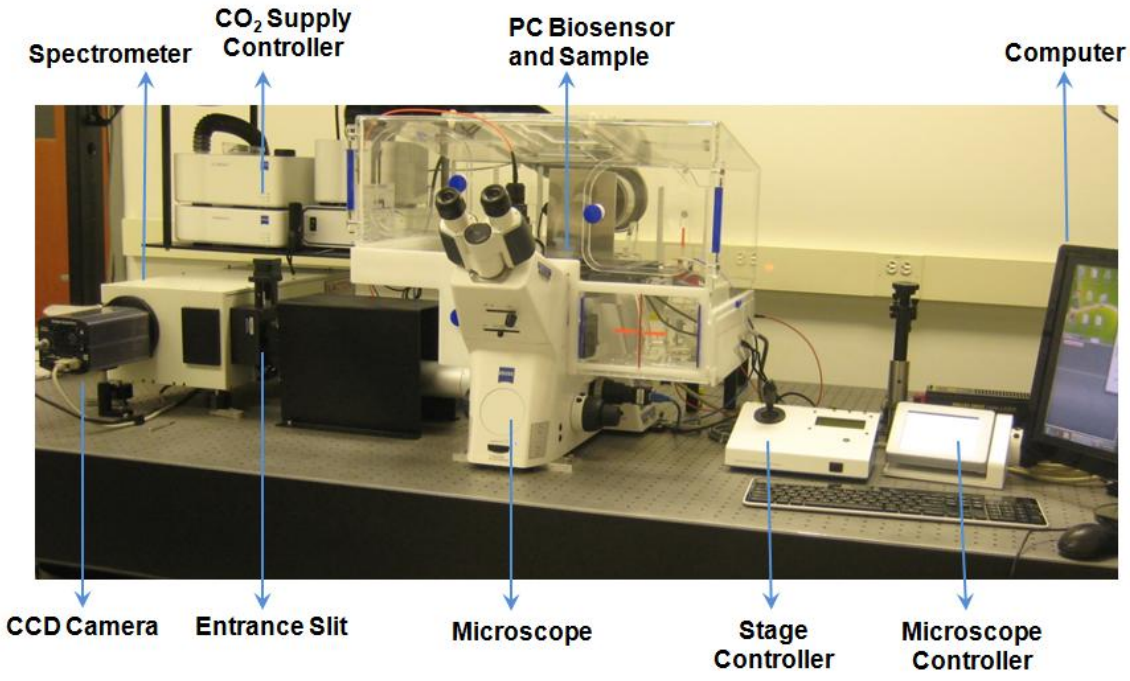

Figure 2.7 A lab photo of the photonic crystal enhanced microscopy (PCEM).

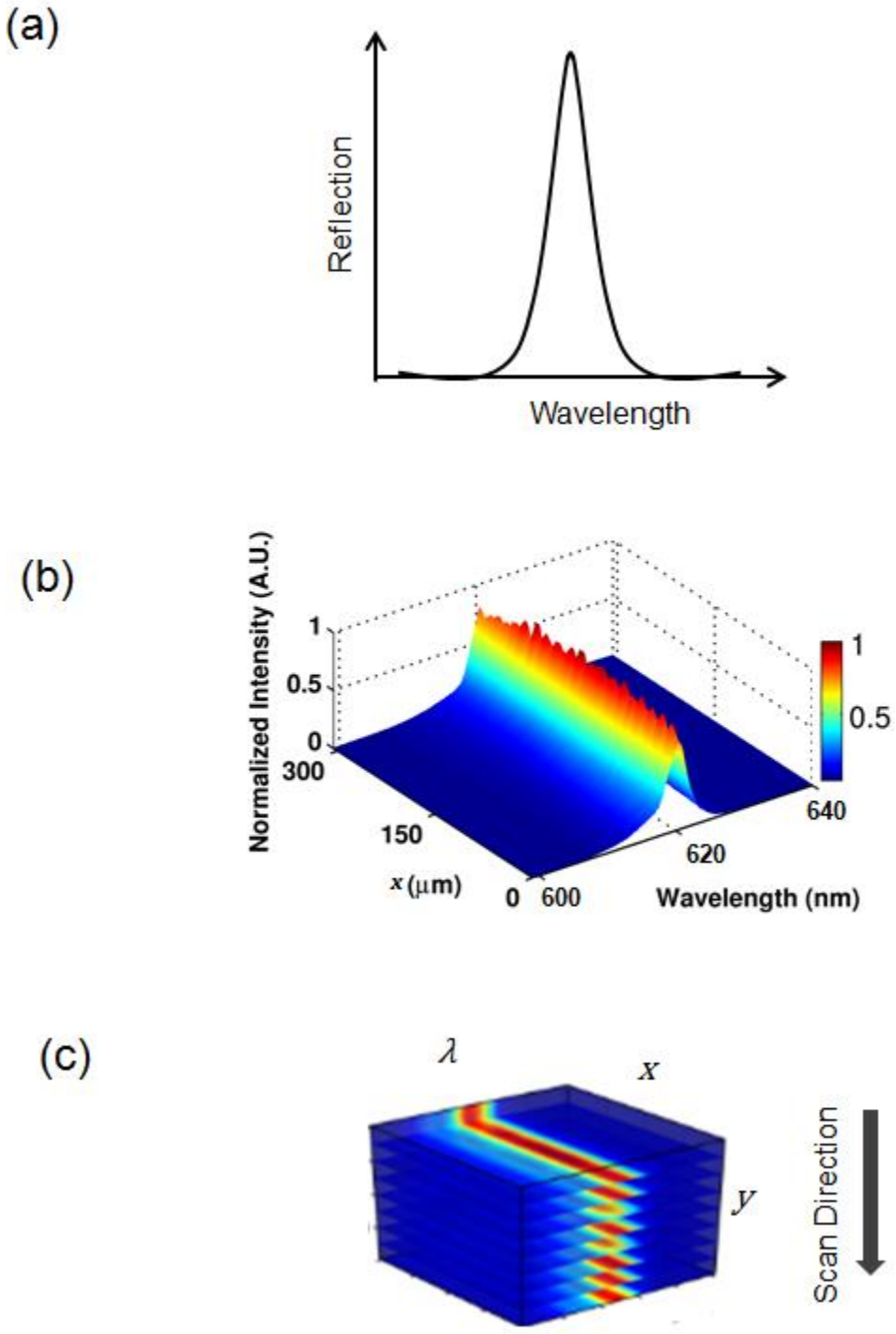

Figure 2.8 PCEM Data Acquisition. (a) Example spectrum at resonance wavelength. (b) Normalized spectrum image (surface plot). (c) PCEM system acquired 3D spectrum data.

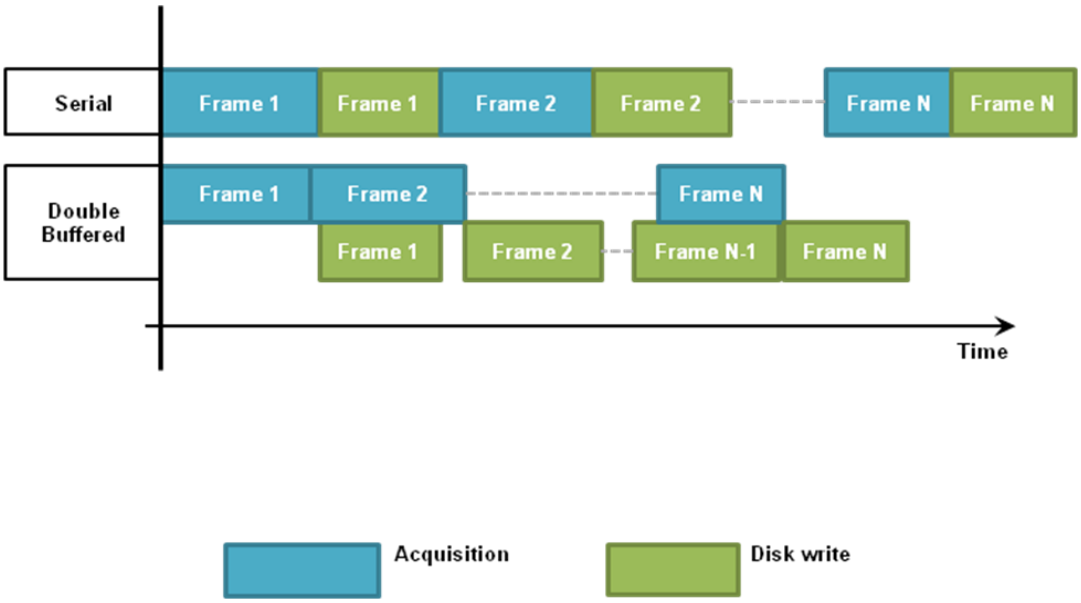

Figure 2.9 Double Buffered Imaging Acquisition for Fast Scan in Photonic Crystal Enhanced Microscopy System.

CHAPTER 3

LABEL-FREE IMAGING FOR LIVE CELL USING PCEM

3.1 Background and Motivation

The extracellular matrix (ECM) is composed of molecules secreted by cells which can provide structural and functional support to the cells imbedded in this environment. The interactions between cells and their ECMs are critical for the mediation and regulation of many cellular activities, such as adhesion, proliferation, communication, differentiation, etc [1, 2]. Conventional methods for measuring and characterizing these interactions generally require labeling cells with stain or fluorescence dyes/proteins. The labeling methods, however, may be cytotoxic to the cells, vary the conformation of the target proteins in cells, or suffer from the fluorescence photobleaching effect. Therefore, it may complicate the study of cell behavior and function [85, 86].

Label-free microscopy imaging approaches have been developed to address the above challenges and can be used to investigate the cellular-ECM interactions [87-89]. Typically, a biosensor transducer surface (such as thin metal or photonic crystal layer) is utilized in label-free microscopy technologies to generate an electromagnetic signal, including electrical and optical signal. This signal can possibly be modified by the intrinsic physical properties (such as dielectric permittivity) of the biological material on the top of the transducer surface. The selectivity of the label-free biosensor is generally broad owing to the fact that it is determined by the surface chemistry rather than the sensor itself. Surface Plasmon Resonance imaging (SPRi) [90] is one of the popular

label-free methods that can measure cell attachment. The principle of SPRi, which utilizes electromagnetic surface waves propagating (parallel to the dielectric/metal surface) on a thin planar metal film (such as gold), is to detect the permittivity change by the surface reflected light with a certain angle under specific resonance conditions. However, SPRi maybe in practice for live cell imaging. For example, the lateral propagation distance of SPRi is typically more than several tens of microns, which may have a degrading influence on the spatial resolution [91]. Both incidence and reflection light paths pass through the cell body which may cause scattering in the reflected light and also lead to complicated data interpretation [92, 93].

In this work, we demonstrate the dynamic label-free imaging using photonic crystal enhanced microscopy (PCEM) to measure the live cell surface attachment profile during adhesion, migration and differentiation. As mentioned earlier, this imaging system incorporates the photonic crystal (PC) biosensor with an ordinary microscope system and a spectrometer to generate the reflection spectrum of the PC, while the output spectrograph is collected with a CCD camera. The PCEM system utilizes the evanescent field atop of the PC as the sensing zone (with a penetration depth of ~200 nm), and can quantitatively measure the dynamic cellular material change and cell–ECM interactions (within the sensing zone). It can also be applied with substrates functionalized with different types or concentrations of ECM molecules, and thus can be broadly used in many extracellular conditions. Furthermore, the PCEM is integrated with an incubator which maintains the normal cell culture condition. Besides, as a label-free imaging system, the PCEM does not suffer from the limitations of fluorescence photobleaching,

and therefore enables long-term monitoring of cell attachment over substantial time scales (such as hours, or up to days).

3.2 Material and Methods

3.2.1 Cell culture

1) 32D Cell

A myeloblast-like cell line (32D stem cell), which is an interleuin-3 (IL-3) dependent murine myeloid progenitor cell line, was purchased from ATCC. Stable cultures of the 32D cell were maintained in RPMI 1640 medium with 2 mM L-glutamine adjusted to contain 1.5 g/L sodium bicarbonate, 4.5 g/L glucose, 10 mM HEPES, and 1.0 mM sodium pyruvate supplemented with 10% heat-inactivated fetal bovine serum and 10% mouse WEHI-conditioned medium. The differentiation of 32D cell into neutrophilic granulocytes is by removal of IL-3 and injection of granulocyte-colony stimulating factor (G-CSF) to the 32D growth medium.

2) ASC cell

Porcine adipose Stem Cells, a type of mesenchymal stem cells (MSC), were obtained from Matt Wheeler's group in Animal Science. Stable cultures of ASC cells maintained in low glucose DMEM supplemented with 10% FBS. For osteogenic induction, they were cultured in low glucose DMEM supplemented with 10% FBS, 0.1 μM dexamethasone, 10 mM beta-glycerophosphate, and 50 μM ascorbic acid.

3) mHAT cell

Murine dental stem cells (mHAT) were attained from the Harada Lab. Stable cultures of the wild type HAT cell were maintained in Dulbecco's Modified Eagle Medium supplemented with B-27 serum free supplement (Invitrogen), 20 ng/ ml bFGF and 20 ng/ ml EGF (Peprotech).

3.2.2 Stem cell differentiation

Induce the ASC cells with ASC osteogenic induction medium and use ASC growth medium to culture uninduced PASC cells as a negative control. Incubate PASC cell for 21 days and gently change the medium every third day without disturbing the cell monolayer.

3.2.3 Photonic Crystal Biosensor Surface Preparation

PCs were sonicated for one minute in acetone, followed by cleaning with IPA and water. After thorough drying with N_2, devices were oxygen-plasma treated for 1 minute to facilitate attachment of a liquid containment gasket. A polydimethylsiloxane (PDMS) gasket with an internal area of 1×1 mm^2 was prepared with a thickness of 10 mm. After application of the gasket well, the PC surface was hydrated with phosphate buffered saline (PBS), and a layer of fibronectin was adsorbed to promote cellular attachment. The sensor was inserted into a custom holder attached to the motorized stage of the microscope, followed by PWV image scanning.

3.2.4 Customized Stage Holder with Chamber

A customized holder with chamber on the scanning stage of the microscope is built to fix the PC biosensor on the stage. The holder can avoid the random movement of

the PC biosensor on the stage, which may caused by pipetting liquid from or to the basket around the PC device and thus influence the relative imaging position. The PC device can be screwed onto the custom holder and then the holder can be further fixed to the scanning stage together with the PC. To be utilized in the dynamic live cell imaging, a customized chamber is built to cover the holder and can be connected with the CO_2 mixer to provide 5% CO_2 air with humidity to maintain certain pH value of the cell medium, which is necessary to the long term live cell survival.

3.2.5 Development of Traction Software for Cell Boundary Evolution

Cell movement is hardly avoidable during live cell imaging and thus there is a need to measure and characterize cell displacement/behavior dynamically. To this end, numerical methods to detect and track cells are necessary along with tools performing quantitative analysis. Automated and high throughput computational imaging analysis methods are essential for accurately analyzing the spatiotemporal cell membrane dynamics. Semi-automated contour-based analysis methods have been used to measure protrusion activity of the cell. Recently, more sophisticated algorithms have been developed to track the protrusive movement of the cells during adhesion or random migration. The level-set-based approach has been applied to reconstruct the continuous motion of cell membrane from video images [94, 95]. However, this approach is computationally demanding and it is also challenging for the whole-cell tracking with general cell shapes.

In this work, we generalized this level-set-based method to whole-cell tracking, as well as balanced the tracking accuracy and computational cost. As such, our imaging

analysis tool can be utilized to detect and track whole-cell membrane movement for an extended period of time with reasonable computational cost. The dynamic mass redistribution can thereafter be quantified and correlated with the membrane protrusions. The overall flow chart of the software program is shown in Figure 3.1, which includes cell boundary detection, boundary evolution, time course quantification and cross-correlation analysis.

To detect the cell edge, the k-means clustering method was used to differentiate the different intensity layers of the PWV image. It is relatively robust to imaging noise and uneven background. For cell boundary evolution, we adapted the level set method (LSM) as described in [94, 95]. The level set method is an approach for tracking the evolution of complex boundaries, which is briefly described here.

The following equation defines the location of cell boundary at a certain time:

$$\Gamma(t) = \left\{(x, y) \middle| \varphi(x, y, t) = 0\right\}, \tag{3-1}$$

where $\Gamma(t)$ represents the cell boundary at time t; the point (x, y) is located at the cell boundary; $\varphi(x,y,t)$ is the level set function and it represents the signed distance from location (x,y) to the boundary $\Gamma(t)$ at time t. Equation (3-1) illustrates that the cell boundary $\Gamma(t)$ can be estimated at the zero level of the level set function $\varphi(x,y,t)$ at any time t. To simplify calculation, we assume that the cell boundary moves toward its normal direction, and the cell boundary evolution thus can be described as a Hamilton-Jacobi equation:

$$\frac{\partial \varphi(x, y, t)}{\partial t} = V\left(\varphi(x, y, t), t\right)\left|\nabla \varphi(x, y, t)\right|, \tag{3-2}$$

where $V(\varphi(x,y,t),t)$ is the speed function of level set function $\varphi(x,y,t)$ at time t; ∇ represents the gradient operator; and $|\bullet|$ denotes the Euclidean norm. Equation (2) depicts that the cell boundary $\Gamma(T)$ can be propagated to its consecutive frame boundary $\Gamma(T+1)$ using LSM through estimating the intermediate boundaries.

In general, it is a challenge to accurately align the corresponding boundary points between two time frames, assuming normal propagation. This problem of misalignment is especially severe at the sharp corners of the boundary with large curvatures at the front or rear parts of cell. One possible solution is to decrease the step length of the level set method during boundary evolution. However, this will result in a significant increase in computation time.

To balance the computational accuracy and calculation time, we use a reasonable small step length in the level set method to estimate enough intermediate boundaries between each pair of time frames. Then we apply a spline fit method to map all the intermediate boundaries to spline boundaries parameters by a 1D coordinate. Using this approach, the problem of aligning the boundary between successive frames is reduced to aligning 1D spline coordinates. During the boundary alignment and propagation, several types of boundary misalignment with geometric conflictions are checked and corrected, as shown in Figures 3.2.

To map the mass redistribution and boundary protrusion along the cell edge, the sampling window on the PWV image is selected to be about 0.6 μm in depth and 1.25 μm in width along the cell edge. To build the sampling band (which is average intensity and velocity in region located near the edge of the cell at certain depth with a certain

width), we use a distance map (an image which intensity is the Euclidean distance to the cell boundary) to acquire a constant band with 0.6 μm in depth toward the cell center along cell boundary. The windows are then used as masks for sampling PWV shift and boundary displacement at a given time and location. The sampling procedure in temporal dimension is done as follows: (1) For the PWV shift, the sampling window is used to mask the PWV shift image and calculate the average PWV shift value inside the sampling window; (2) The cell boundary displacement is also calculated by averaging the displacement vectors of boundary points at the corners of the windows. Therefore, both the PWV shift (along the cell boundary) and boundary velocity are sampled into a two dimensional map. Then the spatiotemporal relationship between mass redistribution and cell morphological behavior along the boundary can be studied based on the two dimensional map.

To investigate the spatial-temporal relationship between PWV shift and cell boundary evolution at migration initiation, the cross-correlation (CC) along the temporal and spatial dimensions are calculated between PWV and cell boundary translocation, respectively. The temporal cross-correlation is defined by the following equation:

$$\rho(S, B, \tau) = \frac{Cov(S, B, \tau)}{\sigma_S \sigma_B}, \tag{3-3}$$

where S and B represent the time courses of PWV shift and cell boundary translocation, respectively; τ denotes the temporal difference between two time courses S(t) and B(t); $Cov(\ )$ is the covariance of two time courses between PWV shift and cell boundary

evolution; σ_S and σ_B represent the corresponding standard deviations of the centered time courses. And *Cov*( ), σ_S and σ_B are defined as in the following equations:

$$\begin{aligned} &Cov(S,B,\tau) = E[(S(t)-\mu_S)(B(t-\tau)-\mu_B)], \\ &\sigma_S = \max_{\text{all sampling windows}} \sqrt{Var(S(t)-\mu_S)}, \\ &\sigma_B = \max_{\text{all sampling windows}} \sqrt{Var(B(t)-\mu_B)}, \end{aligned} \tag{3-4}$$

where *E*[ ] represents the expectation value of a random variable; *Var*( ) is the variance; μ_S and μ_B denote the means of the time courses of PWV shift and cell boundary translocation, respectively. Equation (3-3)-(3-4) reflect that the temporal difference τ between two time courses can be described as peak value of the coefficients calculated by the normalized cross-correlation. The global normalization with maximum correlation among all sampling window was used to modify the Pearson's cross-correlation, to highlight the subcellular regions with significant change in mass redistribution or more cell protrusion. The spatial cross-correlation functions are calculated in a similar fashion to evaluate the spatial shift between the line scans of mass redistribution and cell protrusion along the whole time course of imaging.

3.3 Results and Discussion

3.3.1 Detection of Live Cell Attachment

We demonstrated the detection of single stem cell attachment using PCEM imaging system. Murine dental stem cells (mHAT) were cultured and allowed to attach to a PC surface prepared with fibronectin over a period of two hours. From the series of peak wavelength value (PWV) images (Figure 3.3(a)) gathered at 10 minute intervals,

initial attachment times can be identified within the 10 minute period of image acquisition. Cells are observed attaching to the pretreated PC surface, with initial attachment characterized by small, round areas of PWV shift, consistent with spherical cells exiting suspension. As time progresses, average cell diameter increases, and membrane boundaries become more irregular as cellular processes begin to extend from cell bodies. Many cells maintain highest shifts at their periphery, which is consistent with the high concentration of cytoskeleton protein necessary for boundary maintenance and lamellar extension. Random locomotion is observable, which reveals that cellular detachment results in a full recovery of initial PWV values when a cell moves to a new location. As cells attach and spread, positive PWV shifts are observed due to an increase in the concentration of cellular material within the evanescent field region of the PC.

Representative spectra are shown from inside, boundary and outside of the attached stem cell (Figure 3.3(b)), demonstrating a definitive whole-spectrum shift of the characteristic resonant peak. For instance, the spectra of three specific locations are plotted in Figure 3.3(b) as black, red and green curves, which are corresponding to the three small circles in Figure 3.3(a) at 30 and 50 minutes (black circle –cell center; red circle–near cell edge and shifted from outside of the cell boundary to inside of the cell boundary as cell spreading; green circle–outside of the cell boundary). At 30 minutes, the spectra peak of the location (red curve) is similar to that of the background pixel (green curve). As the cell attaching and spreading, the cell boundary crosses the location at red circle, thus the peak of the red curve shifted to be similar with the spectra at cell center (black curve). This clearly indicates that the PCEM system can detect cell attachment dynamically through peak resonance shift values.

One interesting phenomenon, as shown in Figure 3.3(a), the PWV images indicate that the cell falls on the surface and start to attach after a while. This earlier attaching time varies for individual cells and it could be ranged from 10 minutes up to 50 minutes. This detection ability at earlier attachment is unique in PCEM for live cell imaging. And it can't be easily detectable in conventional bright-field (or fluorescence) imaging modalities, as demonstrated without any obvious changes at the bright-field images (yellow arrows in Figure 3.3(a) at 20 minutes). During this earlier attaching time, it is possible that the cell is probing the surrounding environment, such as pulling or pushing the extracellular matrix (ECM) fibers absorbed to the substrate surface for testing the material stiffness, surface structure and roughness, as well as selecting the binding sites. It is likely that the mass redistribution of the cell body will also start from this earlier attaching time, including the transmembrane receptors (e.g. intergrin) relocation to the focal adhesion sites at the bottom of the cells. Therefore, PCEM imaging system can successfully detect this mass redistribution procedure at the live cell earlier attachment.

We next performed the PCEM imaging of live cell attachment for different cells to demonstrate the identification of the imaging system. Three different stem cells (32D, ASC, mHAT) were tested with the PCEM imaging. 32D cells are interleukin-3 (IL-3) dependent murine myeloid progenitor cells that are widely used as an in vitro model of hematopoiesis [96, 97]. Adipose-derived stem cells (ASC) [98, 99] and dental pulp epithelial stem cells (mHAT) [100, 101] are both mesenchymal cells commonly used in bone tissue engineering and regenerative medicine. Both PWV images and bright-field images are obtained and the statistical results are analyzed based on five cells in each type of stem cells. As shown in Figure 3.4, the three different stem cells demonstrate

distinct features in the PWV images, such as aspect ratios, areas, perimeters, lengths and widths, etc. For example, the aspect ratio of the attached cell body for ASC is significant higher than the other two types of stem cells (mHAT and 32D cells). While the attached cell areas and perimeters of 32D cell are significant smaller than ASC and mHAT cells. One can utilize these attachment information obtained from the PWV images to identity and classify different stem cells.

Furthermore, dynamic attachment features can be extracted from the dynamic acquisitions using PCEM imaging system. As shown in Figure 3.5, sequences of video frames for PWV and bright-field images are analyzed for mHAT cells attachment and the dynamic changes during attaching procedures are obtained, such as attaching areas, perimeters, aspect ratios, centroid locations, mean PWV intensities, etc. For instance, the timing and gradient of the cell areas spreading and perimeters growing during attachment are significantly different among the three different stem cells. As shown in the Figure 3.6, the dynamic analysis of PCEM imaging results demonstrate that the 32D cell can fully attach within 10~20 minutes, while the ASC and mHAT cell will spend more than 40 minutes to be able to fully attach on the substrate surface. This phenomenon can be possibly explained by the highly dynamic mobility capability of the 32D cell, as it can be differentiated to white blood cells and share some of the mobility features with the white blood cells.

3.3.2 Dynamic Detection of Single Cell Migration

Cell migration plays essential roles in maintenance and development of multi-cellular organisms, including embryogenesis, tissue regeneration, wound healing, and

cancer metastasis. For example, endothelial cells are programmed to migrate toward the site of nascent blood vessels during tissue regeneration and angiogenesis which supply nutrients for the maintenance and growth of surrounding tissues. During wound healing procedure, stem cells migrate toward the wound place and differentiate into specific cell types. Therefore, understanding the underlying mechanisms regulating cell migration has important implications in regenerative medicine and stem cell therapeutics.

The PCEM imaging system can dynamically detect cell migration. As shown in Figure 3.3(a), a sequence of PWV images represents the migration of mHAT cells in random directions after attached to the substrate surface. The intensity change of the PWV images indicates the mass redistribution of the cell body during migration procedure. To investigate the spatiotemporal partition of mass redistribution at the cell boundary of the migrating cells, photonic crystal biosensor-based live cell imaging and image analysis methods are integrated to visualize and quantitatively analyze the cell migration. The image analysis method, as described in methods section, is developed to automatically analyze the dynamic movement of the boundary evolution during cell migration.

The temporal cell boundary traction results from a single migrating mHAT cell are shown in Figure 3.7 and the color (from blue to red) represents the cell boundary evolution time (from 0 to 220 minutes). The resulting temporal-spatial boundary evolution map is shown in Figure 3.8, while the x-axis indicates the temporal sample points along boundary evolution time (in units of minutes) and y-axis indicates the spatial sample points along the normalized cell boundary length (in absence of units). The color

change of the evolution map indicates the cell boundary evolution cumulative distance (in unit of um) at each temporal-spatial sample point, while blue represents short migration distance and red represents long migration distance. From the boundary evolution map, we can see that the mHAT cell is mainly attaching and spreading during first ~50 minutes, so the boundary movement distance is relatively short (lower than 5 um) as the blue color indicating in the evolution map. Then, the mHAT cell starts to migrate towards "East" direction after ~70 minutes, so the boundary movement distance starts to directionally increase and reaches the longest migration distance (around 14 um) after 120 minutes. Two representative cross-section curves along temporal direction are shown in Figure 3.9, while the blue curve represents the point A and red curve represent point B at the cell boundary in Figure 3.7. The two curve starts with similar migration distance for the first 50 minutes during attachment, then the red curve raises much higher (around three times higher) and reaches a plateau value (around 14 um) after 120 minutes. As we can see from Figure 3.7, point A corresponds to the protrusion part of leading frontier in the cell body during migration and it can be explained well that the leading frontier has the longest migration distance. Our future work is to uncover the underlying mass redistribution mechanism during cell migration using the PCEM imaging system combined with the automatic analysis software.

3.3.3 Detection of Stem Cell Differentiation

Stem cell can differentiate into special types of cells and maintains the normal multi-cellular organism development, such as in tissue repair or embryonic development. Due to modified gene expression, many characters of a stem cell body can have

significant changes during differentiation, including shape, size, metabolic activity and responsiveness to certain environment signals, etc. Different types of stem cells can have very distinct features among those physical changes during differentiation. By detecting those physical changes, one can distinguish whether the stem cell is differentiated or characterize the differentiation stage.

We performed the adipose stem cell (ASC) osteogenic-differentiation assay on photonic crystal biosensor surface and measured the peak resonance wavelength change using PCEM imaging system. The ASCs were treated with the osteogenic induction medium for entire differentiation time. Every other day, the treated ASCs were collected and then seeded on the photonic crystal biosensor surface upon imaging time to measure their attachment performances. The resulting sequence of detected differentiation images are shown in Figure 3.10. From both the bright-field and PWV images, we can clearly see that the ASC is more elongated with a thin spindle shape at day 0 of differentiation procedure. As the differentiation carrying on (e.g. day 4), the shape of the ASC gradually becomes to be more rectangular, which is progressive to the morphology of osteoblasts. At day 10, the induced osteoblasts demonstrate a rectangular morphology, which is similar to an adult osteoblast's morphology. These imaging results illustrate that the PCEM imaging system can successfully detect the attachment performance change during stem cell differentiation procedure. The future work includes applying this PCEM detection assay to different types of stem cell differentiation, such as 32D stem cell differentiation.

3.4 Figures

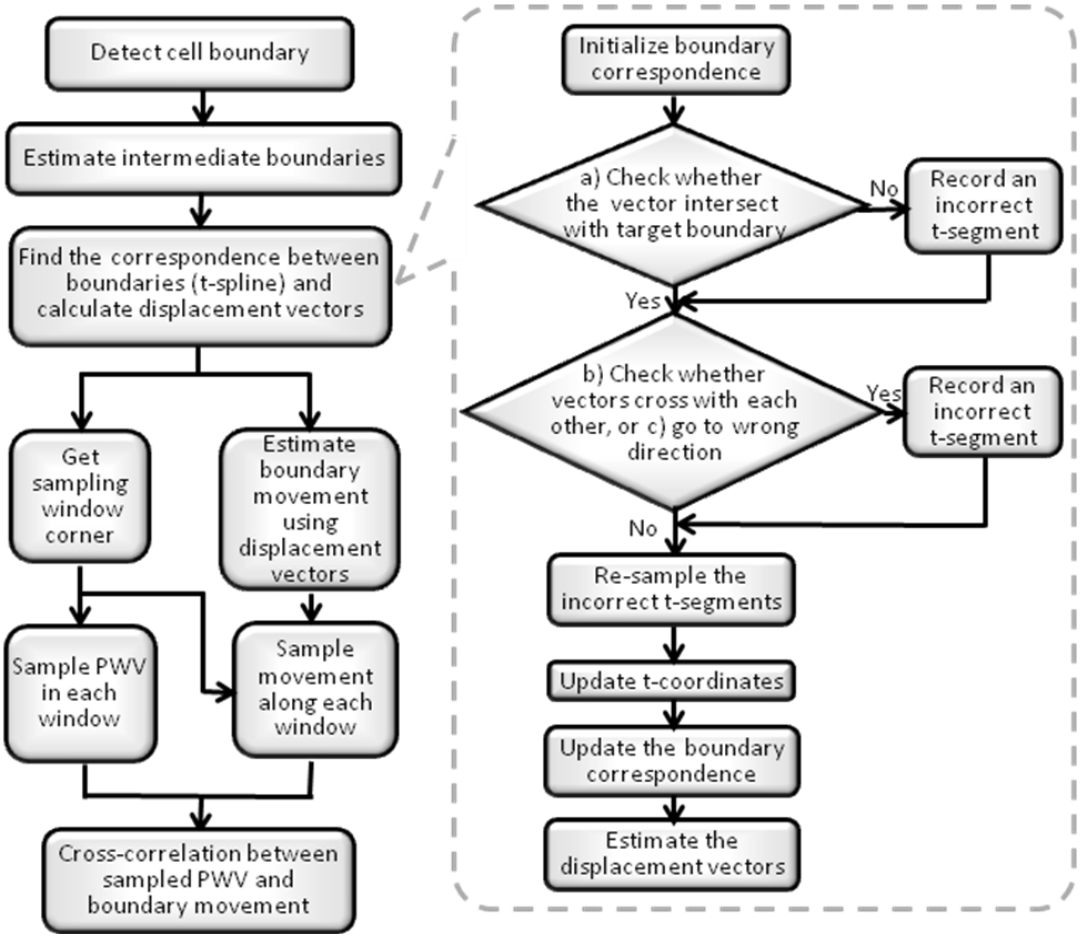

Figure 3.1 The flow chart of the software program includes cell boundary detection, boundary evolution, time course quantification and cross-correlation analysis.

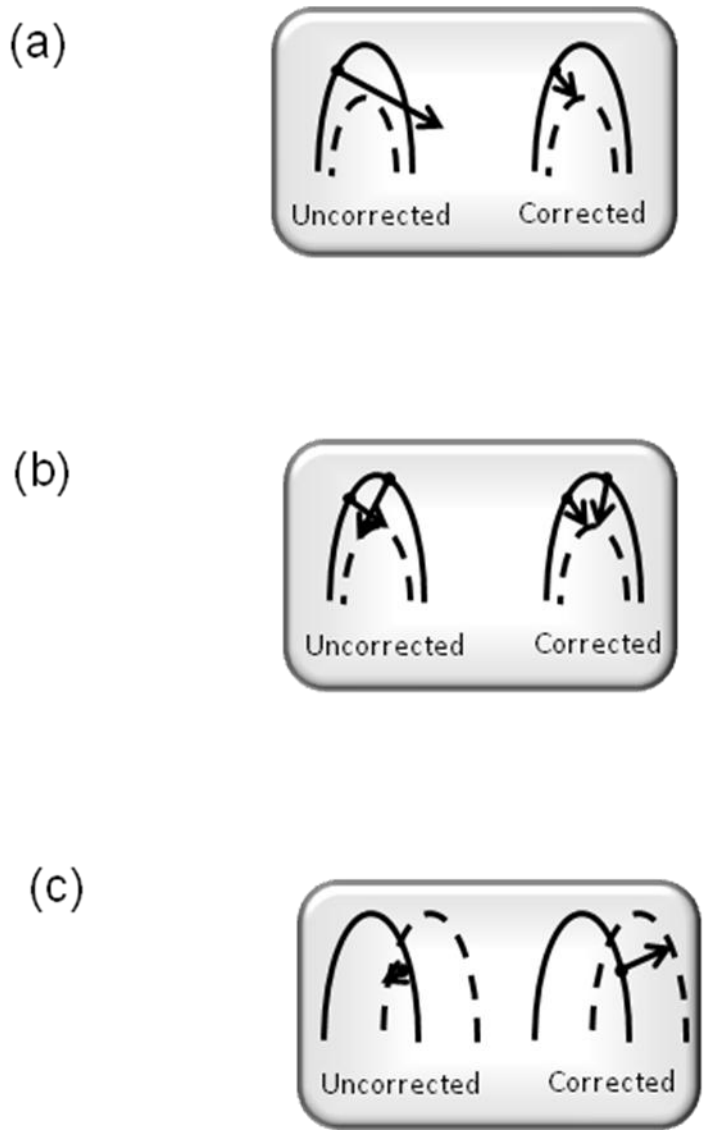

Figure 3.2 Special cases of boundary misalignment with geometric conflictions

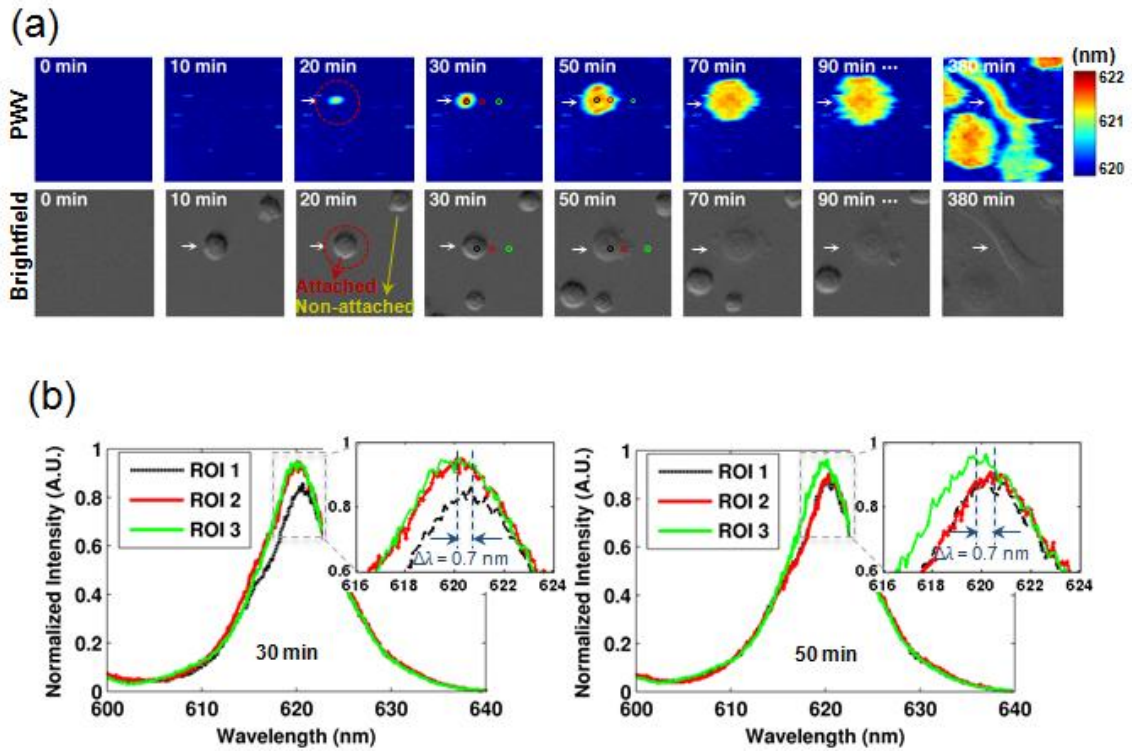

Figure 3.3 Label-free, Dynamic Detection of Stem Cells Attachment using PCEM. (a) Stem Cells (mHAT) were seeded on a fibronectin-coated PC sensor surface and start to attach after 10 minutes (Top row: PWV images, bottom row: bright-field images), indicating a higher localization of cellular material at the sensor surface which can be expected during cell spreading. (b) Spectra are shown from inside, boundary and outside of the attached cell at 30 and 50 mins (3 regions are marked with black, red and green circles).

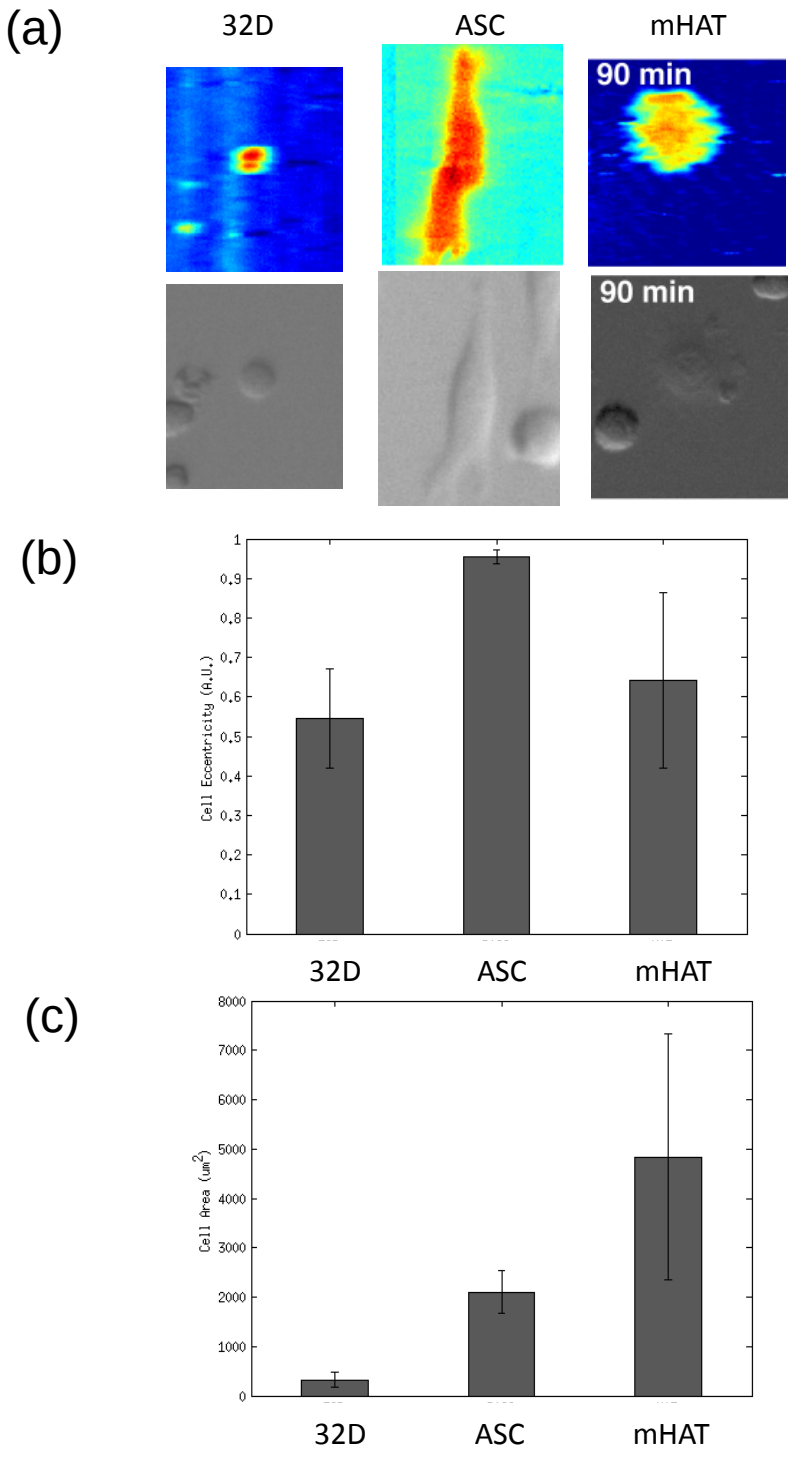

Figure 3.4 Label-free Detection of Stem Cells Attachment using PCEM. (a) The three different stem cells (32D, ASC, and mHAT) demonstrate distinct features in the PWV images, such as (b) aspect ratios or (c) attached areas of the cell bodies.

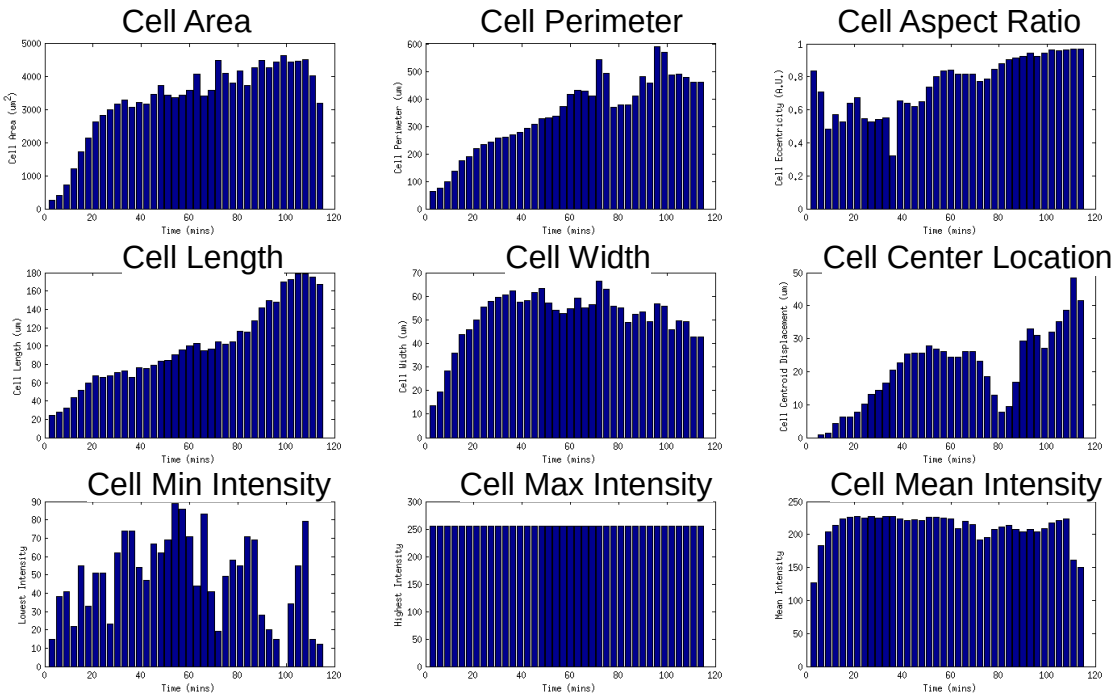

Figure 3.5 Dynamic changes during mHAT cells attaching procedures are obtained with PCEM and analyzed with the boundary evolution software. Cell information, including (a) attaching areas, (b) perimeters, (c) aspect ratios, (d) length, (e) width, (f) centroid locations,(g)min image intensities, (h) max image intensities, (i) mean image intensities, are plotted in temporal dimension.

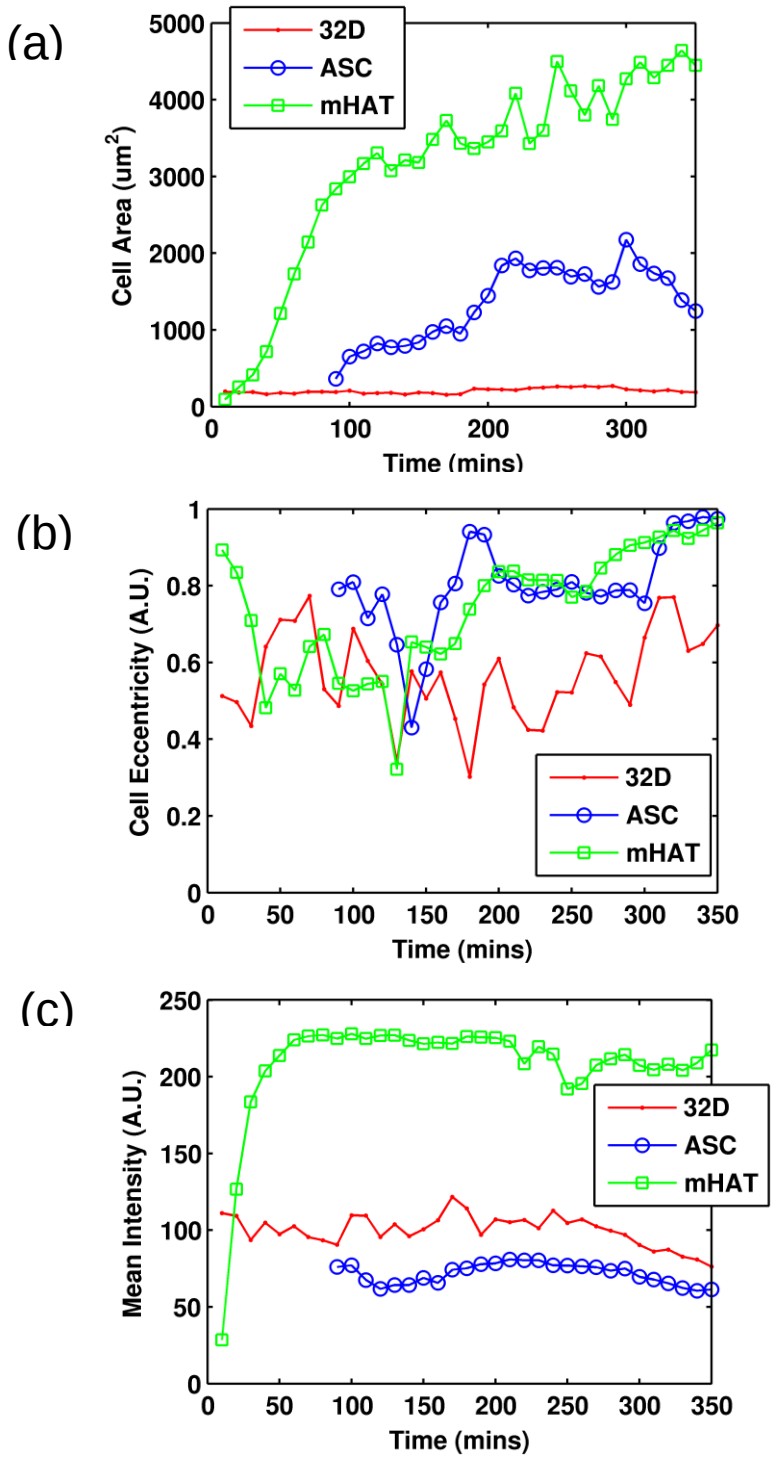

Figure 3.6 Comparison of dynamic of PCEM imaging results analysis (including temporal changes of cell area, aspect ratio and mean intensity) for three different stem cells (32D, ASC, and mHAT).

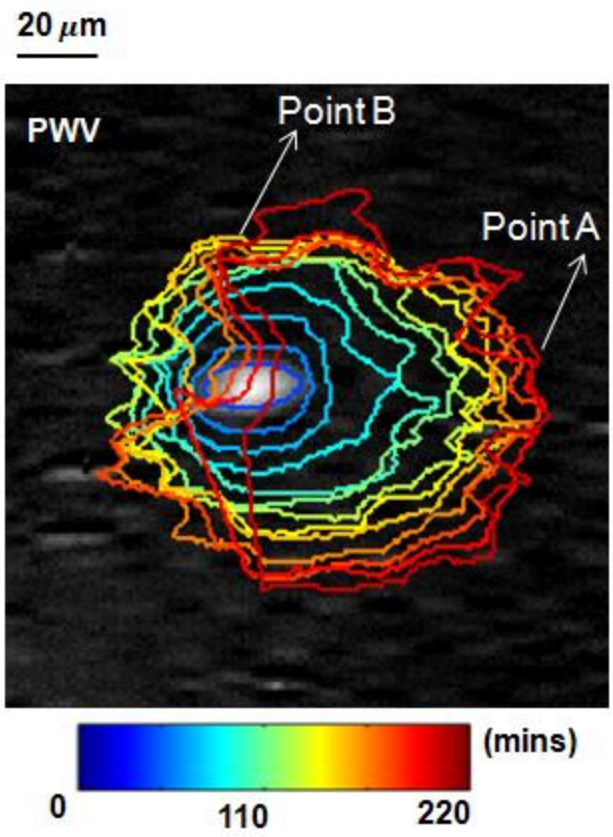

Figure 3.7 Stem cell boundary evolution extracted from PWV images along temporal dimension (color bar demonstrates the time for cell attaching and spreading).

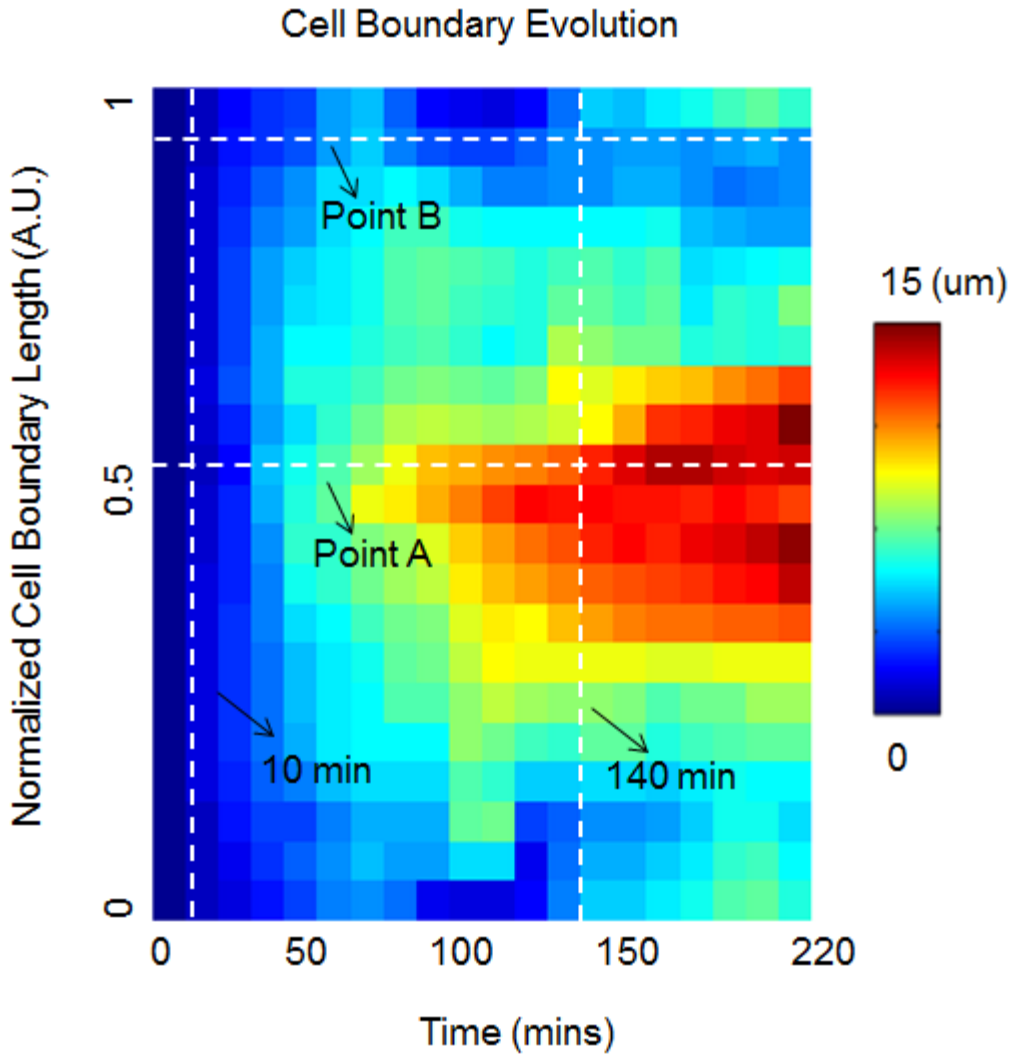

Figure 3.8 Two-dimensional map represents the spatiotemporal relationship between mass redistribution and cell morphological behavior along the boundary.

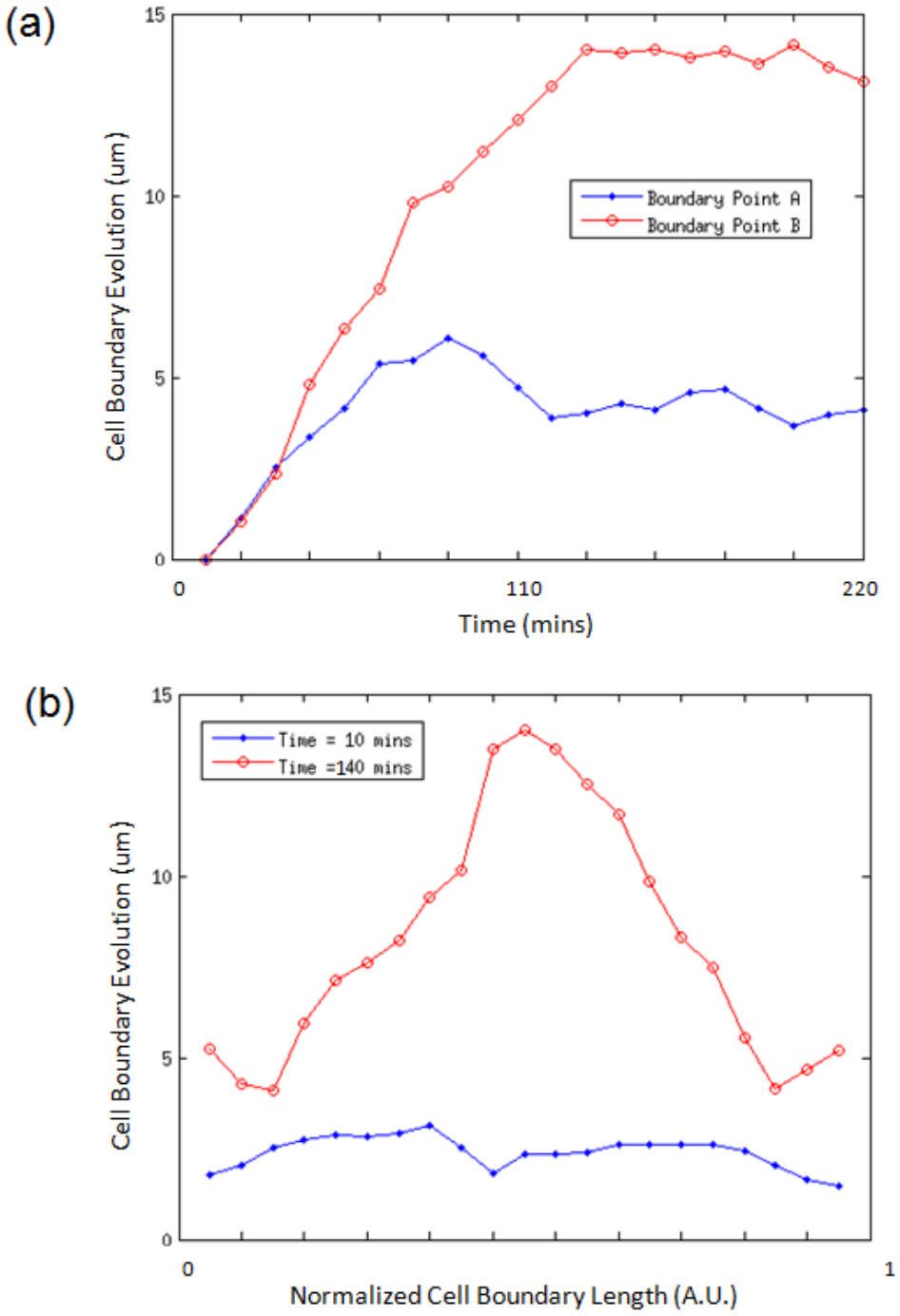

Figure 3.9 Representative cross-section curve for cell boundary evolution along (a) temporal dimension and (b) spatial dimension.

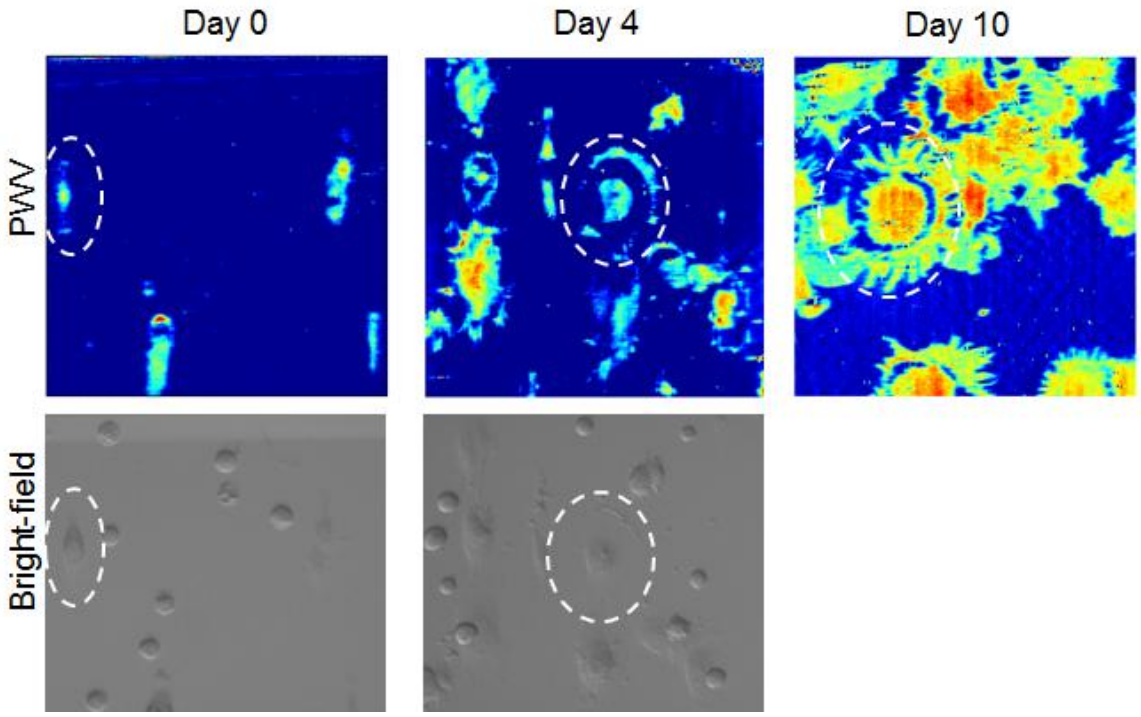

Figure 3.10 The PCEM detected PWV and bright-field images for ASC Osteogenesis differentiation at different stages (day 0, day 4 and day 10).

CHAPTER 4

LABEL-FREE IMAGING OF NANOPARTICLE ATTACHMENT ON PHOTONIC CRYSTAL BIOSENSOR

4.1 Background and Motivation

Nanoparticles (NP) prepared from dielectric [102], semiconductor [103], metal [104], and magnetic [105] materials have recently become important elements of biosensor technology due to the ability to prepare their surfaces with ligands that enable them to recognize specific target molecules, and their ability to interact with electromagnetic fields in useful ways [106-116]. For example, nanoparticles with dielectric permittivity greater than that of water may be used as secondary tags for enhancing the signals from resonant optical biosensors [117], while magnetic nanoparticles are used to facilitate particle manipulation while at the same time providing a mass amplification tag for acoustic biosensors [118]. Likewise, metallic nanoparticles, comprised of silver or gold, couple with external illumination sources to generate surface plasmons, which are used to enhance local electric fields on the nanoparticle surface [119, 120].

While many biosensing approaches are capable of sensing the adsorption of large numbers of nanoparticles [121], several approaches are capable of detecting the presence of a single nanoparticle, if the particle is adsorbed to a specific active location [122-126]. Due to the difficulty of directing analytes to precise locations on a substrate surface

where a biosensor has sensitivity, one approach to overcoming this limitation is to utilize a biosensor surface in which the entire surface area is active as a sensor. Through the use of an imaging detection approach, the adsorption of analyte upon any region within the field of view may be measured. Imaging-based biodetection utilizing optical sensors has been demonstrated using surface plasmon resonance [127-129], photonic crystal biosensors [67-70, 130], and dielectric thin film interference sensors [131-134]. Such approaches are advantageous because analytes that produce highly localized changes in dielectric permittivity, such as cells, virus particles, or nanoparticles, may be detected, with the potential to observe the attachment of individual targets.

In this work, we apply the photonic crystal enhanced microscopy (PCEM) to detect the attachment of dielectric and metallic nanoparticles upon a photonic crystal (PC) surface. While our initial demonstration of PCEM described imaging the spatial distribution and time evolution of live cell attachment strength to a functionalized PC surface with 0.6 μm pixel resolution [66], here we report the detection of nanoparticles that are smaller than the pixel size. We demonstrate that metallic (gold) nanoparticles or nanorods produce highly localized effects upon the photonic crystal (PC) resonant reflection spectrum that enable individually attached particles (as small as ~65 nm×30 nm) to be easily observed by two distinct mechanisms. Furthermore, we observe that the dielectric permittivity of particles results in a local shift in the resonant wavelength of the PC, while the optical absorption of nanoparticles results in a localized reduction in the resonant reflectivity magnitude. We anticipate the use of dielectric or metallic nanoparticles as functionalized tags in "sandwich" style assays that can be used to visualize the presence of individual captured analyte biomolecules upon a PC surface.

4.2 Material and Methods

4.2.1 FDTD Simulation

Simulation of the reflection spectrum and the electric-field distributions with FDTD is performed to predict the peak resonance wavelength and intensity shift caused by the nanoparticle attachment. Two periods of the PC are simulated with the periodic boundary conditions applied to perpendicular to the grating structures. The incident light is set to be p-polarized (TM mode) from normal direction beneath the PC device. The nanoparticle is placed in several different positions on the PC surface, including on the top of the grating structures and between the gap of the grating structures.

4.2.2 Photonic Crystal Biosensor Surface Preparation

PC surface were prepared similar to the previous chapter, except no need for coating an extracellular matrix molecules. Briefly, PCs were cleaned with isopropyl alcohol (IPA) and MilliQ water, respectively. After thorough drying with Nitrogen air (N_2), the PC biosensors were treated with oxygen-plasma and attached with a PDMS gasket. Then the sensor was inserted into a custom holder attached to the motorized stage of the microscope, followed by PWV image scanning.

4.2.3 Deposit Patterns of Polymer Spots Using tDPN

An array of nano-patterns is deposit on the photonic crystal surface with a newly developed technique - thermal Dip-Pen Nanolithography (tDPN) [135-138]. A heated AFM tip deposited polystyrene nanopatterns on the photonic crystal surface. This process consists of two major steps. The first step is to ink the AFM tip. A custom-built AFM tip

made of doped silicon was heated up to 260ºC by applying electric currents through the AFM tip. As the AFM tip was heated, we brought the AFM tip into contact with a polystyrene (PS) fiber using a micromanipulator under a microscope. Once the tip contacted the PS fiber, the PS melted and inked the heated AFM tip. The second step is to deposit PS onto the photonic crystal surface. The inked heated AFM tip was mounted on an AFM (Model MFP-3D, Asylum Inc.) and scanned across the photonic crystal surface. When the AFM tip was heated up and reached a temperature of 260ºC, the molten PS migrated from the heated AFM tip to the photonic crystal surface, formed solid PS nanopatterns upon cooling by the photonic crystal surface. For fabricating nanolines of PS, the AFM tip scanned the PC sample at a velocity of 150 nm/s. For fabricating nanodots of PS, the AFM tip dwelled on the PC sample for several seconds while heating, then heat was turned off, finally the AFM tip withdrew from the PC sample.

4.2.4 Nanoparticle Automatic Counting

After acquiring the PIV images from the PCEM imaging system, accurately counting the number of nanoparticles in each microspot is essential to the final detection results, but also can also be a tedious procedure due to the large number of nanoparticles in each field of view (it typically reaches several hundreds, even up to thousands). In this study, we developed a software to analyze the PIV images and automatically count the nanoparticles. The imaging analysis procedure is shown in a flow chart in Figure 4.1 and can be summarized as follows: (1) Image preprocessing to remove the noise and non-even background; (2) Image segmentation to detect local maxima; (3) Ad hoc region characterization to eliminate the false-positives. This sub-section will introduce some of

the imaging algorithm involved in this program along with the development of this counting software.

1. Preprocessing

The analysis software begins with a preprocessing procedure, which can be decomposed into two major components: (1) denoising with a low-pass filter; (2) uneven background removal.

Noise can be introduced to the imaging system during the image acquisition procedure which influences the determination of the resonance wavelength shift and intensity change. For denoising procedure, a Wiener filter is applied to filter out the noise by estimating the noise variance from local neighborhood. The Wiener filter is based on the prior knowledge of the spectral properties of the original stationary signal and noise spectra assumed to be known (more precisely, the spectral properties are estimated from the image itself using local neighborhoods). A minimum mean-square error (MMSE) is used as the performance criterion in the filter design procedure which can benefit to the capability of controlling the output error to the image. Therefore, the Wiener filter can avoid the problem of singularity of the typical inverse filtering and can be designed straightforwardly. The neighborhood used has size 3-by-3, and an example phantom image with noise and the resulting filtered image are shown in Figure 4.2.

The non-uniform illumination background is another typical disruption to the image processing procedure, which is often difficult to remove completely. To estimate the uneven background, a morphological opening of the image is performed, as shown in

the Figure 4.3(a). Then by subtracting the estimated background image from the denoised image, the resulting image demonstrates a relative uniform background, as shown in Figure 4.3(b).

2. Extended Maximum Detection

The extended maxima transform is a morphological operation aiming at finding local maxima in grayscale images. It is defined as the result of the regional maxima operation applied on the H-maxima transform of the grayscale image. The H-maxima transform (where H is a non-negative scalar) locates peaks of height larger or equal to H. In particular, this discards low contrast peaks which are more likely the result of noise in the grayscale image. The regional maxima operation then segments the grayscale image into regions corresponding to the different peaks (i.e. local maxima) in the image. In the context of nanoparticle counting, this operation selects candidate regions that may correspond to nanoparticles. Further refinement will discard candidates based on region properties. The resulting segmented mask image is shown in the Figure 4.4(a).

3. Connected Components Analysis

To label and count each nanoparticle, connected components analysis (CCA) is applied to the segmented mask image. The CCA algorithm can label each object in the image and count it as one element, and then return a matrix with all of the labeled elements. Such labeling is useful, not only for counting the nanoparticles but to process them individually (by characterizing their shape and eliminating false positives as described in the next section). The CCA algorithm can be summarized by the following

steps: (1) A run-length encode (RLE) algorithm, often used in the data compression, is applied to the segmented mask image to obtain and store the sequences of the connected pixels with the same intensity values. (2) Next, all of the sequences are scanned to assign a preliminary label and record the label equivalence to each of them. (3) After the scan is finished, the equivalence classes are resolved to group the elements to one another. (4) Based on the results from resolving equivalence classes, the elements are relabeled and recounted to obtain the correct sequence number.

4. Ad hoc Nanoparticle Candidate Region Characterization

We next applied an ad hoc characterization to eliminate the false positive count, which can possibly come from noise, artifacts or segmentation inaccuracies. This step consists in measure shaping properties on each labeled region, and using empirical rules to eliminate undesirable candidates. The rules enforced are: (1) the total area of the nanoparticle region must not exceed a certain threshold, (2) the region must not be too elongated (this is measured by the long-axis to short-axis lengths ratio) and (3) the region must not extend too much in the y-direction. The last rule stems from the fact that images are degraded by stripes in the y-direction, which typically generates some false positives along the stripes. The resulting segmented mask after removal of undesirable candidates is shown in Figure 4.4(b).

5. Recount

After removing the effect from artifacts, we finally count to the nanoparticles in the resulting image. For validation, the automatic counting procedure was compared to

the numbers obtained by manual counting for a few datasets. Counting results are shown on Table 4.1 and confirm that the automatic counting algorithm provides an accurate estimate of the true count. The counting results on the phantom image of nanoparticles are shown in Figure 4.4(c), while the number of the small black circles represents that of nanoparticles.

4.3 Results

4.3.1 FDTD Simulation Results

The simulated electric-field power distributions ($|E|^2$) of the PC at the resonant wavelength with/without a TiO2 (500 nm) and Au (100 nm) nanoparticle are shown in Figure 4.5, in which a uniform plane wave illuminates the structure at normal incidence with a magnitude of E = 1 V/m. The "Empty" PC simulation (Figure 4.5(a)) demonstrates the expected establishment of an evanescent electric field at the surface with enhanced electric field magnitude that develops due to the formation of electric field standing waves. Figure 4.5(b-e) demonstrate the presence of TiO2 or Au nanoparticles at two slightly different locations on the PC biosensor surface (deposited on top of a grating tooth, or at the bottom of the gap between teeth), respectively. The presence of nanoparticles (at the bottom of gap between teeth) induces substantial changes in near-field distributions and results in a shift of resonance wavelength by $\Delta\lambda = 1.04$ nm (TiO2) and $\Delta\lambda = 0.14$ nm (Au). The predicted reduction in the resonant intensity by the presence of the TiO2 and Au nanoparticles is $\Delta I = 60\%$ and $\Delta I = 13\%$, respectively (Figure 4.6).

4.3.2 Dielectric Nanoparticle Detection

To facilitate investigation of PCEM's ability to detect individual nanoparticles with tightly controlled spatial distribution and size, we first sought to intentionally deposit patterns of polymer spots using tDPN. The principle of tDPN is to use a heated AFM tip to deposit polystyrene (PS) nano-patterns on the PC surface. We printed 3×3 arrays of PS dots (540 nm diameter, 40 nm height, and 5 μm gaps between dots) on a PC surface confirmed by AFM imaging (Figure 4.7). Figure 4.8 displays the measured PWV images of the tDPN printed nano-dots. From the spectrum of two neighboring pixels (marked with black and green circles in Figure 4.8 inset image), we can visualize a peak-wavelength shift of $\Delta\lambda = 0.5$ nm caused by the nano-dots (black line), compared to the background pixel (green line) (Figure 4.9). The PCEM-measured diameter (Figure 4.10(a)) closely matches the AFM-measured diameter (Figure 4.10(b)), except that the nano-dot dielectric permittivity slightly increases the PWV of surrounding pixels. It is important to note that the nano-dots are approximately the same size as the pixel, so a single nano-dot can partially occupy several adjacent pixels at the same time.

Having demonstrated the ability to observe and resolve dielectric-based polymer nanoparticles that were intentionally patterned on the PC, we next sought to detect dielectric TiO2 nanoparticles of approximately the same size, but distributed randomly on the PC surface (Figure 4.11). The PC surface was prepared by cleaning with isopropanol and deionized (DI) water, followed by drying using N_2. To further facilitate nanoparticle attachment, the PC was oxygen-plasma treated for five minutes after cleaning. The TiO2 nanoparticle is 500 nm in diameter (Microspheres-nanospheres, #220374-10) and

incubated in DI water on the PC surface for two hours and then imaged via PCEM. Figure 4.12 shows the measured PCEM spectra for two neighboring pixels (black line represents the location of an adsorbed TiO2 nanoparticle, while the green line represents a background pixel without an adsorbed nanoparticle). The TiO2 nanoparticle induces a highly localized and easily observed peak-wavelength shift of $\Delta\lambda = 1.12$ nm and a peak-intensity reduction of $\Delta I = 58\%$. Calculating these values for each pixel in the field of view allows us to form the PWV (Figure 4.11(a)) and PIV (Figure 4.11(b)) images for several independently adsorbed TiO2 nanoparticles.

4.3.3 Metal Nanoparticle Detection

We next sought to detect the presence of surface-adsorbed gold (Au) nanoparticles of approximately 100 nm diameter (Sigma, #742031-25ML), distributed randomly on the PC surface. The PC surface was prepared as described above. Scanning electron microscopy (SEM) images of single gold nanoparticles on the PC surface are shown in Figure 4.13, demonstrating that the particles are present as distinct individuals, rather than as clusters. Individual Au nanoparticles were observed to cause a pronounced change in the resonant reflection spectrum for only the pixels of the PCEM image where the particle was adsorbed. We observe a shift in the peak reflected wavelength of $\Delta\lambda = 0.15$ nm, and a reduction in the peak reflectance intensity of $\Delta I = 12\%$. The PWV shift (Figure 4.14(a)) is a result of the increased real part of the dielectric permittivity of gold with respect to the surrounding water medium, while the decrease in PIV (Figure 4.14(b)) is caused by the imaginary part of the refractive index of gold at the resonant wavelength of the PC, which results in highly localized optical absorption. The localized nature of

the effect can be observed by comparing spectra from neighboring pixels (black line represents a pixel from the location of an adsorbed Au nanoparticle, while the green line represents the background region without an Au particle), as shown in Figure 4.15.

4.4 Discussion

The PCEM detection instrument configuration with 10× objective lens described in this work provides a field of view of 300×300 μm^2, comprised of an array of 0.6×0.6 μm2 pixels, determined by the combined effects of the objective numerical aperture, the scan increment and the pixel size of the CCD camera within the imaging spectrometer. The resolution with which individual nanoparticles may be identified as distinct objects is partially determined by the above instrument parameters, but is also influenced by the ability of the PC surface to confine the lateral propagation of its resonant electromagnetic field standing wave. Ultimately, the resolution of our approach will not be capable of exceeding the diffraction limit, which for a wavelength of $\lambda = 620$ nm and our numerical aperture of 0.25, is d = 1518 nm. The resolution of the optical system can be calculated using Abbe's formula

$$d = (0.612 \cdot \lambda)/(n \cdot \sin\alpha), \quad (4\text{-}1)$$

where λ is the wavelength of the imaging radiation; n is the medium refraction index between the light source and the lens; α denotes half of the angular aperture of the light source. The n·sinα term in Abbe's formula represents the numerical aperture (N.A.).

Using the PCEM images of individual nanoparticles that are smaller than the pixel size, we are able to characterize the extent to which a nanoparticle can influence the resonant properties of neighboring pixels, by observing how the resonant reflectance

properties are influenced as one moves laterally across the PC surface. Because the location of a nanoparticle within a pixel of a PCEM image is random, it is important to note that a particle will always be within a diffraction limited distance of up to five adjacent pixels, and thus we would not expect to observe a single pixel with a shift in wavelength or reflected intensity. The distribution of PWV and PIV shift in the horizontal and vertical directions surrounding individual TiO2 nanoparticles in our images are plotted in Figure 4.16. The data reveals that a 500 nm diameter surface-adsorbed TiO2 nanoparticle results in a positive shift in PWV that extends approximately 6 μm in the horizontal direction (perpendicular to the PC grating lines) and 5 μm in the vertical direction (parallel to the PC grating lines). Calculating the full-width at half-maximum (FWHM) of the point spread function of ten separate TiO2 nanoparticles results in a mean FWHM = 1.56 μm, and a standard deviation of 0.26 μm in the horizontal direction and FWHM = 1.20±0.28 μm in the vertical direction. Thus, for two neighboring nanoparticles to be observed independently, they must be separated by at least 2·FWHM, approximately 3.2 μm. Interestingly, PIV-based PCEM images of the same TiO2 nanoparticles measured using the reduction in reflection efficiency results in slightly improved resolution. We measured FWHM of 0.95±0.09 μm for PIV images in the horizontal direction, and FWHM of 0.96±0.39 μm in the vertical direction. Results are summarized in Table 4.2.

Similar results are obtained when observing the point spread function of surface-adsorbed 100 nm Au nanoparticles. Observation of the variation in PWV and PIV in the horizontal and vertical directions surrounding an individual Au nanoparticle, plotted in Figure 4.17, results in a FWHM of 1.15±0.05 μm for PIV images in the horizontal

direction, and FWHM of 0.97±0.07 μm in the vertical direction. We observe that surface-adsorbed dielectric and metallic nanoparticles extend their influence to surrounding regions of the PC surface for approximately the same distance.

Our observations of the resolution of PCEM images of isolated nanoparticles (100 nm Au NP) suggest that the resonant electric field standing waves of any particular region of the PC are influenced by surrounding regions that are ~3 μm away. Fundamentally, this distance is determined by the design of the PC, as discussed in previous work [65]. The periodic grating structure results in partial back-reflection of resonantly coupled light that has its propagation vector oriented parallel to the PC surface. The modulation of the grating, determined by the grating step height, the thickness of the TiO2, and the refractive index contrast of the TiO2/polymer/water interfaces, determines the efficiency with which laterally-directed light is folded back onto itself. Because the FWHM is ~1200 nm, and the grating period is 400 nm, we estimate that ~6 back reflections are required to confine resonantly coupled light for the PC design used in this work. This factor, rather than the diffraction limit, provides the current resolution limitation of our approach. We have previously shown that PC structures with lower quality (Q) factor (broader resonant bandwidth) provide greater lateral confinement, so this may be a direction for future investigation.

A point of interest for detection of metallic nanoparticles is the overlap between the PC resonant wavelength and the resonant optical absorption spectra of the nanoparticle. In this work, no effort was directed towards aligning these two values, except the last experiment using AuNR. Previous reports [139] demonstrate that Au

nanoparticles of ~100 nm diameter have a broad absorption spectrum with a maximum of 572 nm, that extends to 700 nm. Thus, the PIV images are a result of quenching of the PC resonance due to absorption of light by the Au, but the absorption process used to obtain our PIV images is extremely inefficient. Despite this inefficiency, a single 100 nm Au nanoparticle provides easily measured resonant intensity contrast of ~10%. While the contrast is expected to be further improved either by choosing nanoparticles with resonant absorption spectra that overlaps the resonant spectrum of the PC, or by designing a PC to more closely match the absorption of the nanoparticles. Chapter 5 will address this problem by applying the AuNR with approximately the same resonance wavelength with the PC surface.

4.5 Tables

	ROI 1	ROI 2	ROI 3	ROI 4
Automatic Counting	17	19	14	12
Manual Counting	18	19	14	13

Table 4.1 The Counting Results of Automatic Nanoparticle Counting Software. The automatic counting results was compared to the numbers obtained by manual counting for four regions of interest (ROI).

	PWV FWHM (μm)		PIV FWHM (μm)	
	Horizontal	Vertical	Horizontal	Vertical
TiO_2 NP (500 nm)	1.56 ± 0.26	1.20 ± 0.28	0.95 ± 0.09	0.96 ± 0.39
Au NP (100 nm)	1.85 ± 0.81	1.34 ± 0.34	1.15 ± 0.05	0.97 ± 0.07

Table 4.2 Measured FWHM (mean ± std, in units of μm) in horizontal and vertical directions (in both PWV and PIV images) for 500 nm TiO2 NP and 100 nm Au NP.

4.6 Figures

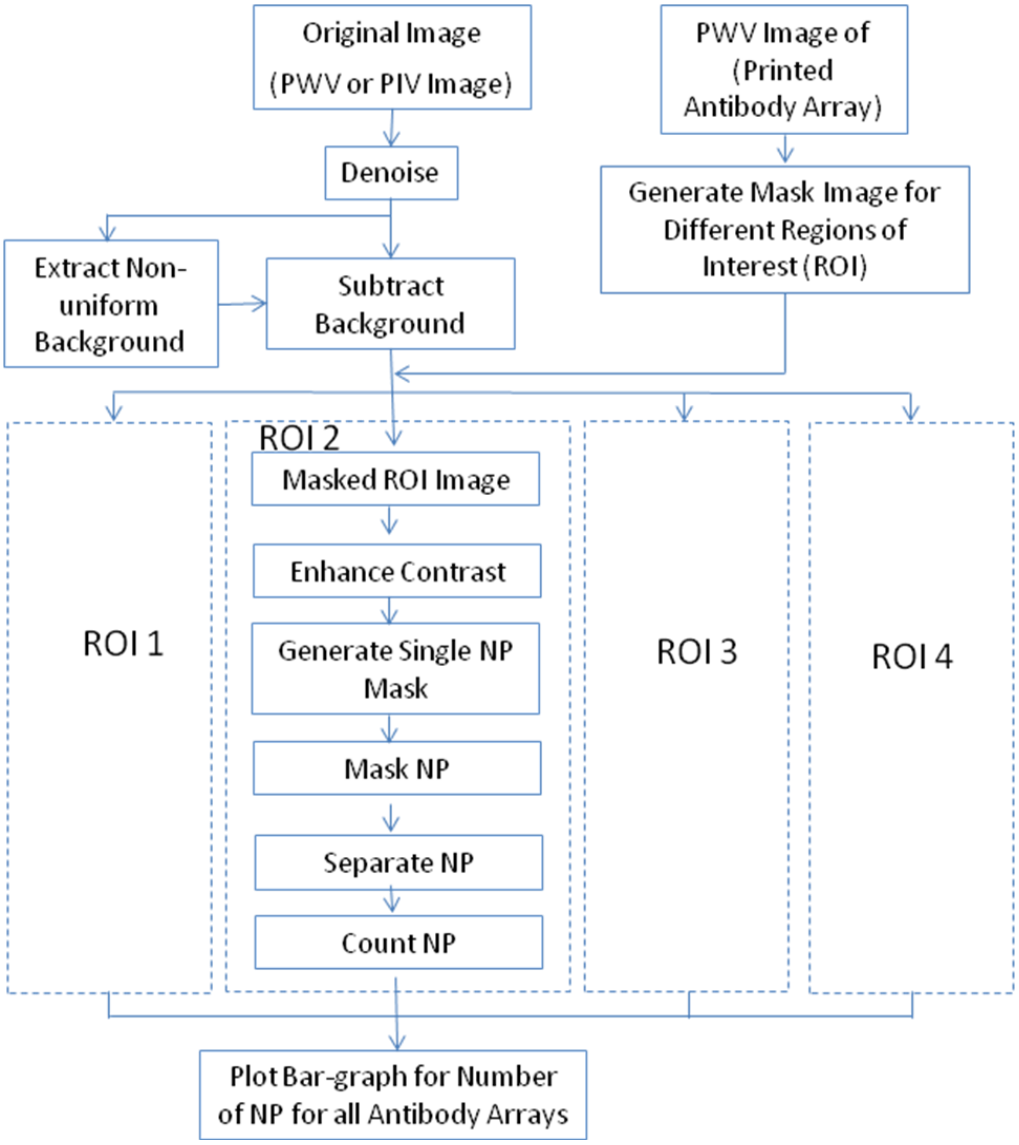

Figure 4.1 The flow chart of automatic analysis and counting for nanoparticle (NP) detection using PCEM system.

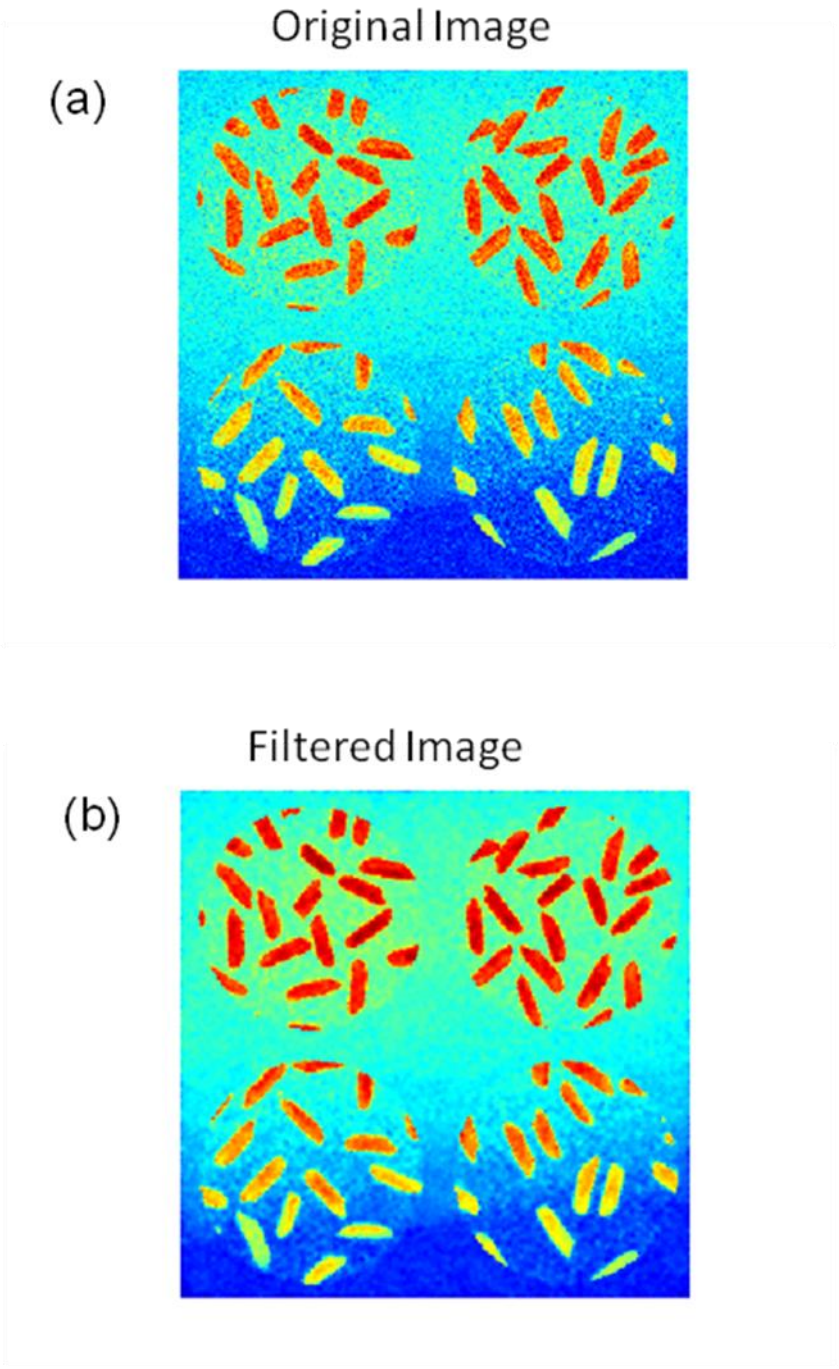

Figure 4.2 The (a) original noisy and (b) filtered phantom images for automatic nanoparticle imaging analysis.

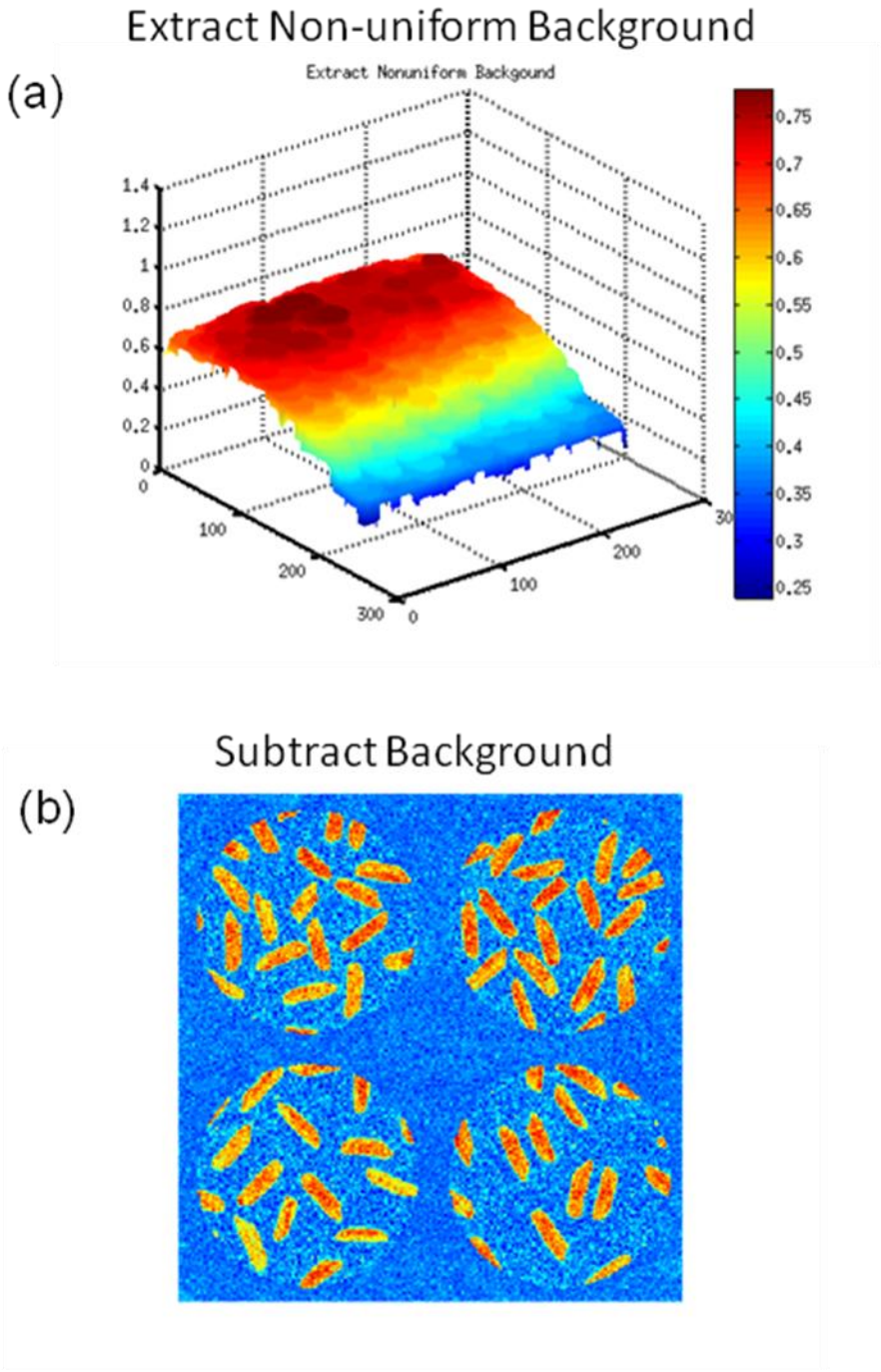

Figure 4.3 The results of removing the non-uniform background in the nanoparticle automatic counting algorithm.

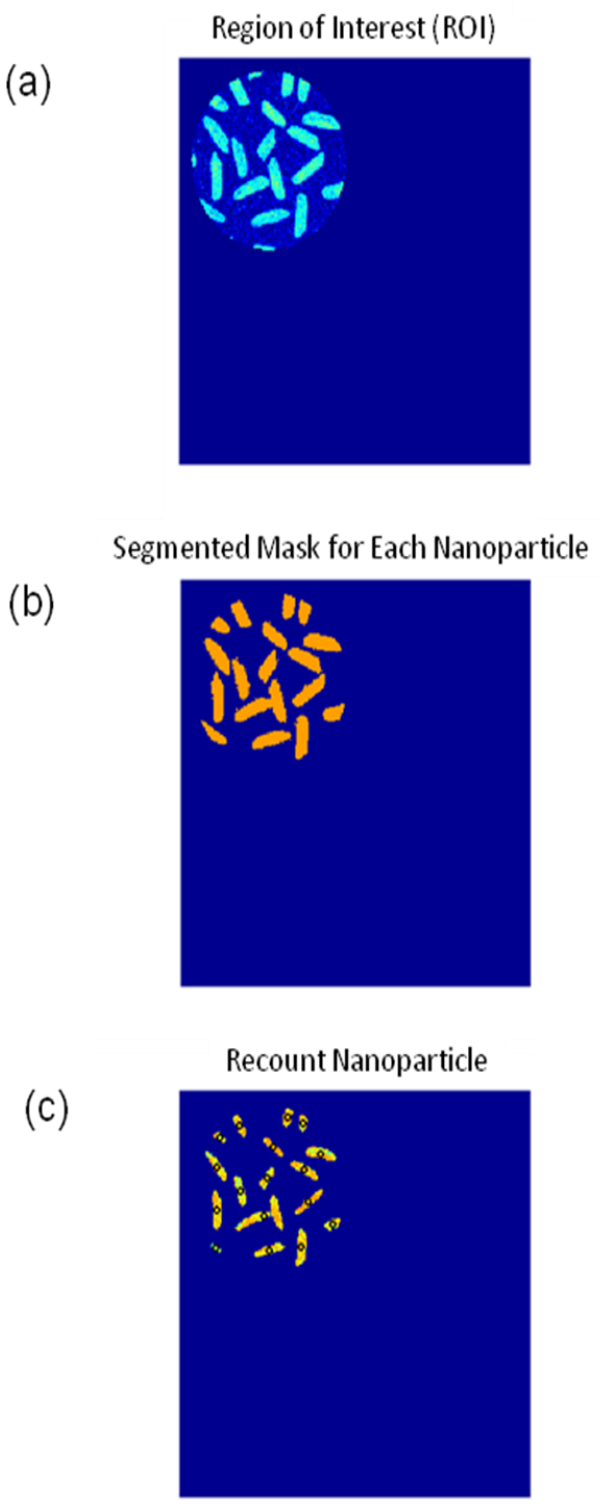

Figure 4.4 The image segmentation and counting for nanoparticle (NP) detection using PCEM system.

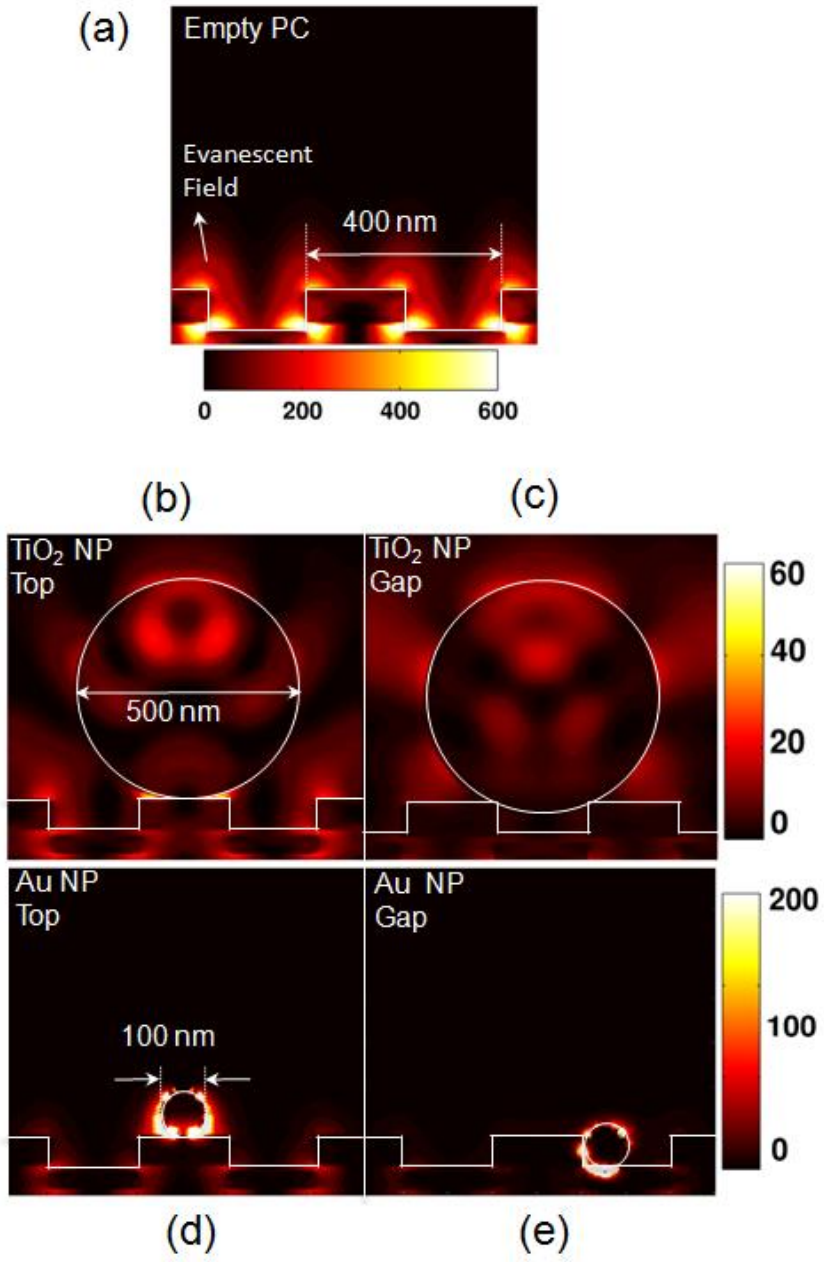

Figure 4.5 Computer simulations of reflection and near field distributions of PC without and with nanoparticles (NP). The simulations demonstrate the Finite-difference time-domain (FDTD) computed electric-field power distributions (in units of V2/m2) for different conditions: (a) Empty PC; (b-c) 500 nm TiO2 NP and (d-e)100 nm Au NP at two slightly different locations on a PC surface (deposited on top of a grating tooth, denoted by "Top", or at the bottom of the gap between teeth, denoted by "Gap").

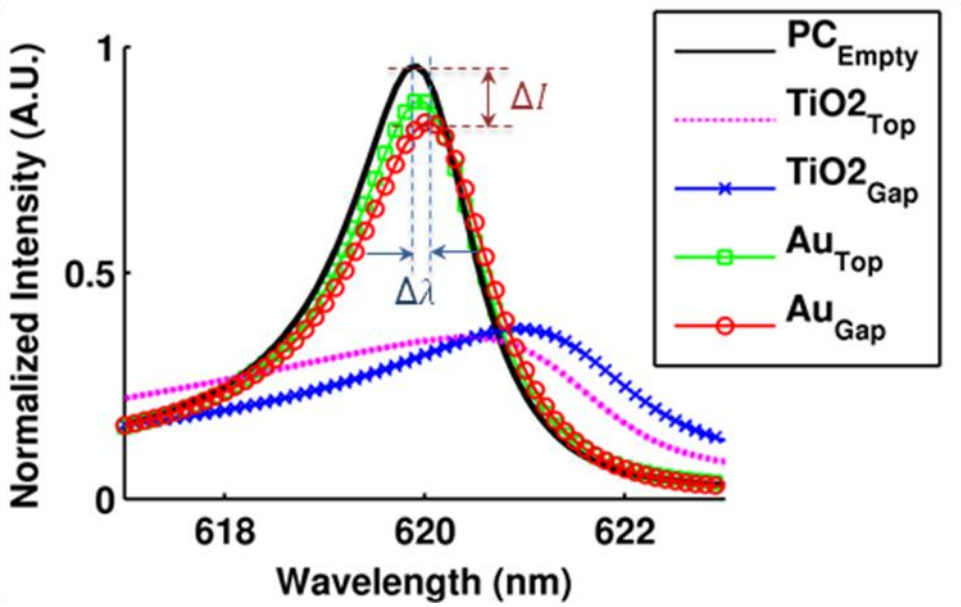

Figure 4.6 FDTD-computed reflection spectra of NPs on PC surface, predicting a clearly measurable change in reflectance wavelength and intensity with/without nanoparticles.

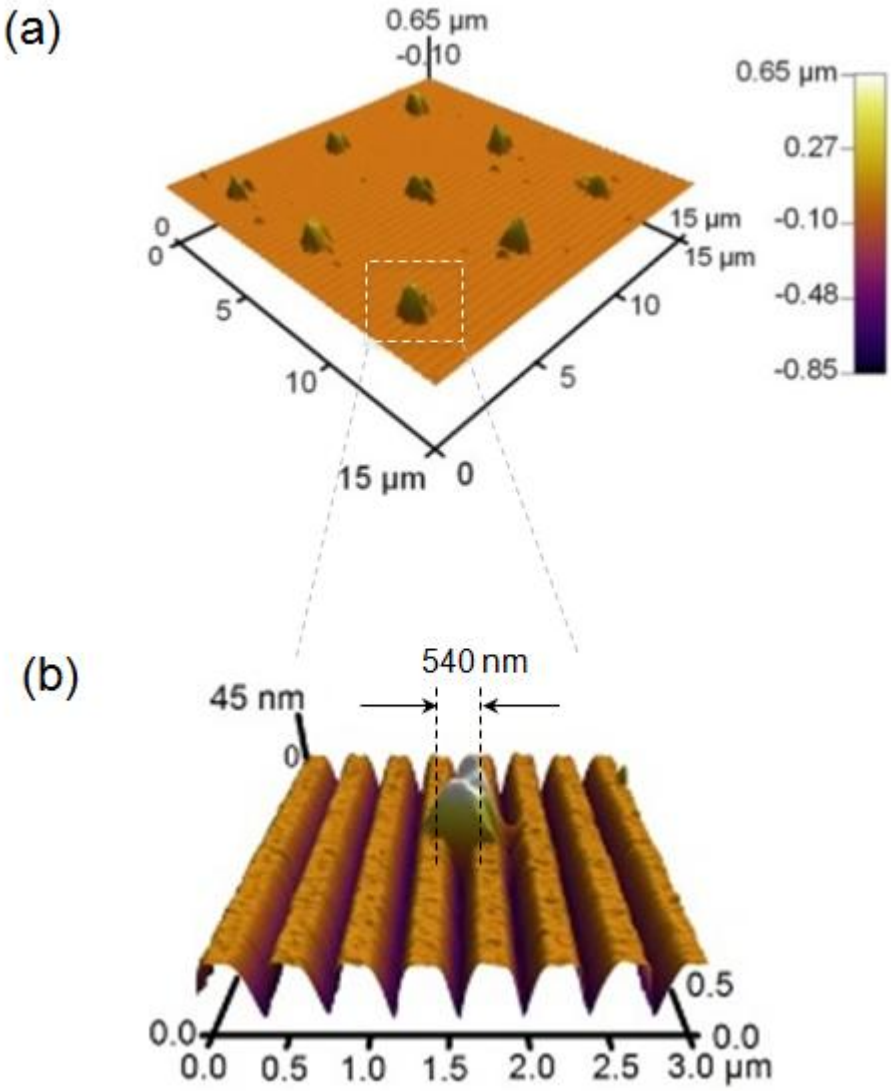

Figure 4.7 PCEM detection of nano-dots printed with thermal Dip-Pen Nanolithography (tDPN). (a) Atomic Force Microscopy (AFM) images of tDPN printed 3x3 arrays of nano-dots. (b) Zoomed in AFM images of one tDPN nano-dots in dimension of 540x540x40 nm^3.

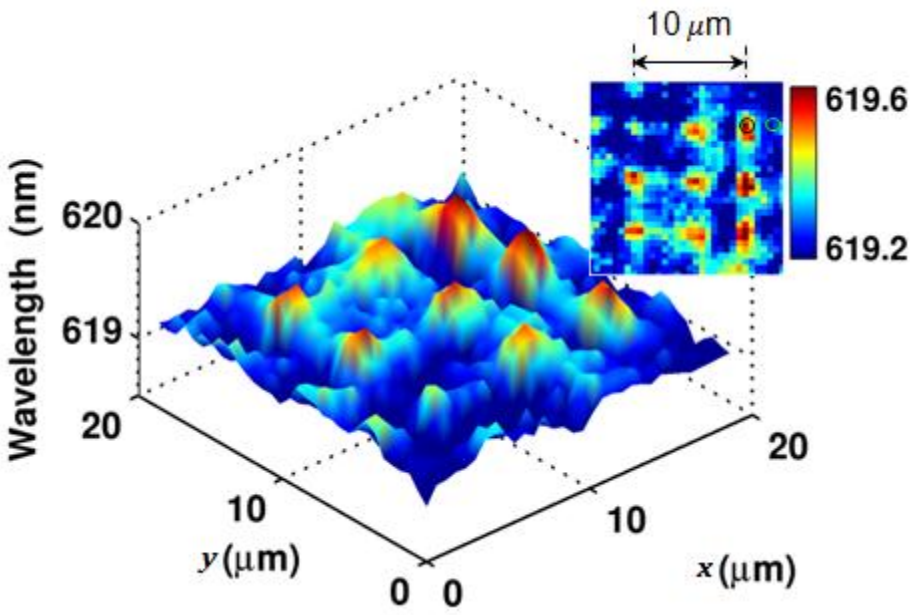

Figure 4.8 PCEM reflected PWV image of the tDPN nano-dots displayed in 3D surface plot within a 20x20 μm^2 field of view. Inset: 2D PWV image, demonstrating the ability of PCEM to resolve PWV differences in single nano-dots attachment on PC surface.

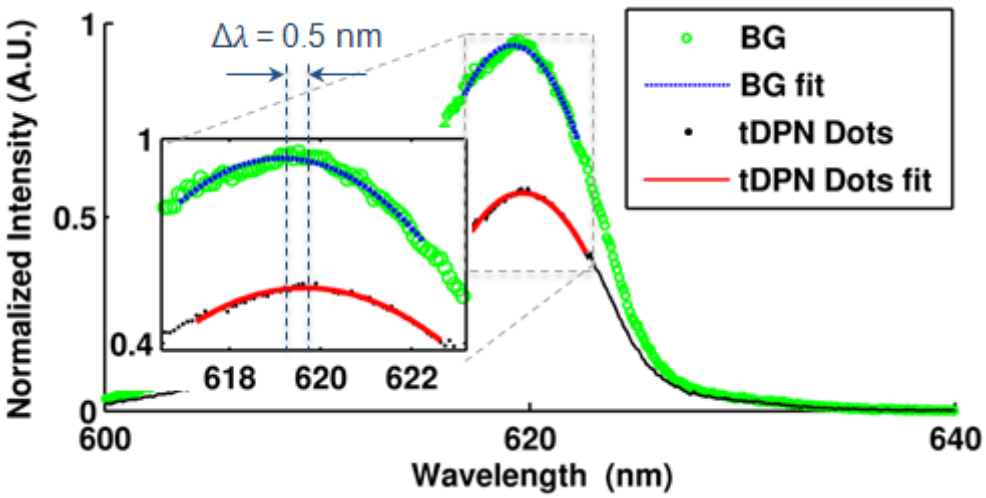

Figure 4.9 Normalized spectrum of a representative tDPN nano-dot (black line) and a background pixel (green line). Inset: Zoomed in image of the spectrum with 2D polynomial fitting (tDPN nano-dots fitting in red line, background fitting in blue line), indicating a PWV shift of $\Delta\lambda = 0.5$ nm.

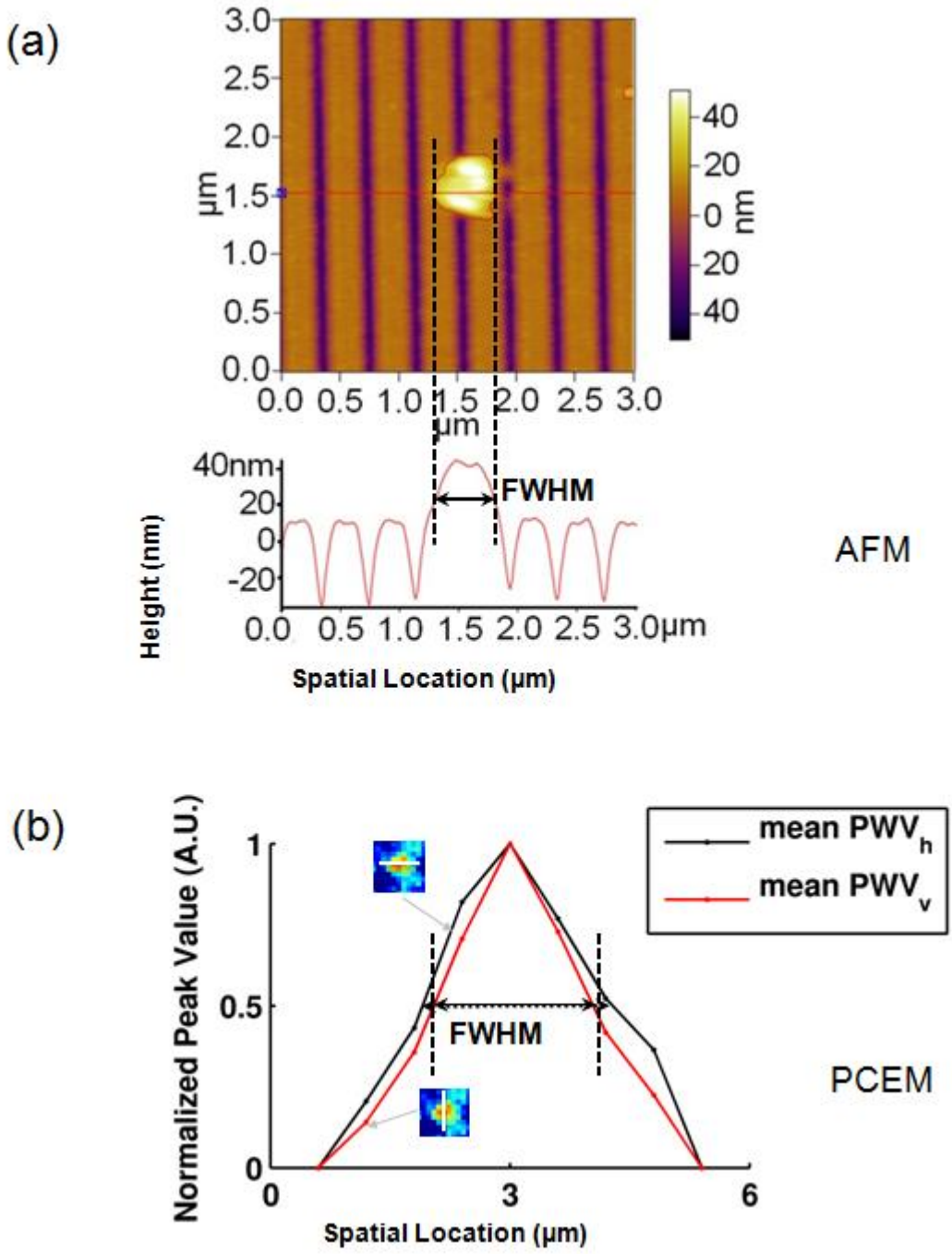

Figure 4.10 Comparison of FWHM of tDPN nano-dots on the PC surface measured by AFM and PCEM. (a) tDPN nano-dots measured by AFM, indicating a FWHM (mean) of 540 nm. (b) tDPN nano-dots measured by PCEM, indicating a FWHM (mean) of 1.20 μm in horizontal direction and 1.13 μm in vertical direction (measured from PWV image).

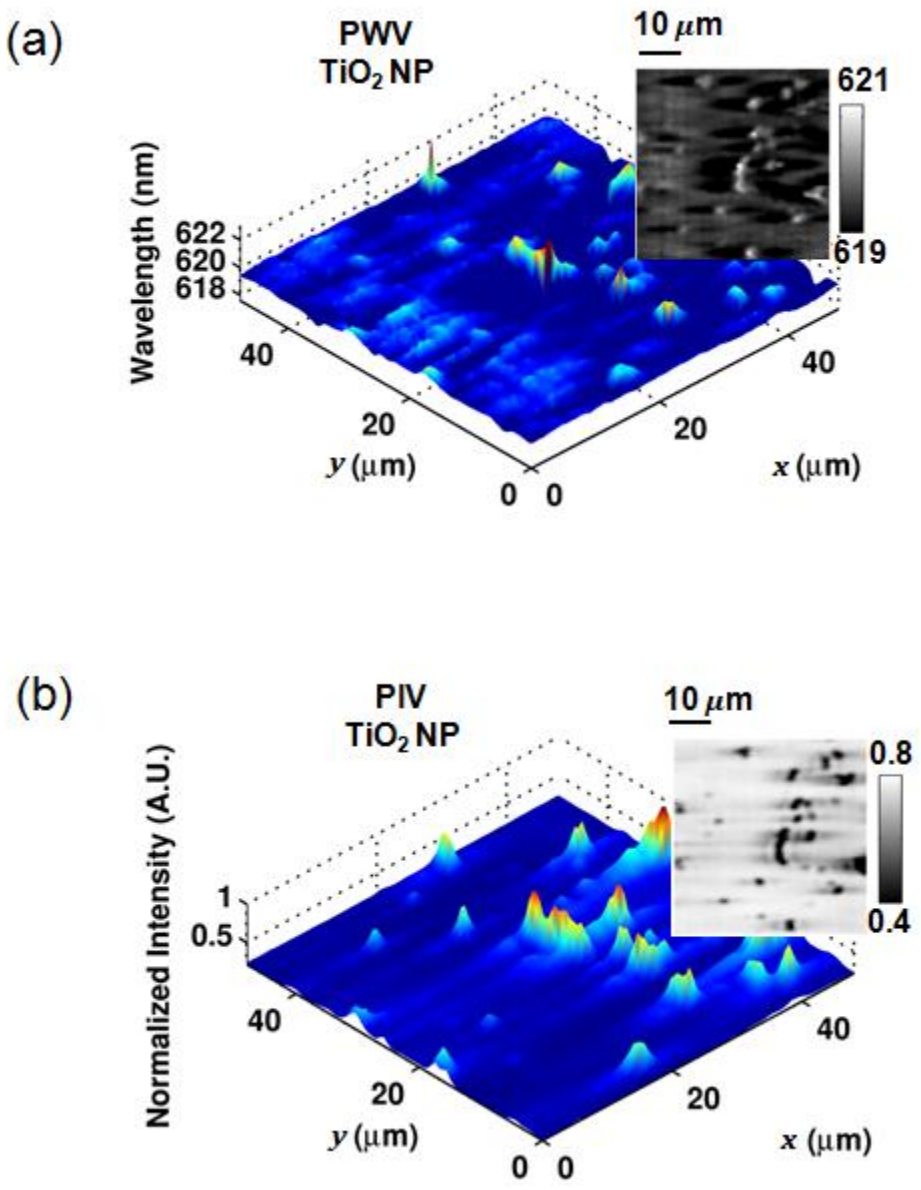

Figure 4.11 PCEM detection of randomly distributed TiO2 nanoparticles (NP). (a) PCEM detected PWV image of the TiO_2 NP displayed in 3D surface plot. Inset: 2D PWV image in gray scale. (b) PCEM detected PIV image of the TiO2 NP displayed in 3D surface plot (inversed for comparison). Inset: 2D PIV image in gray scale.

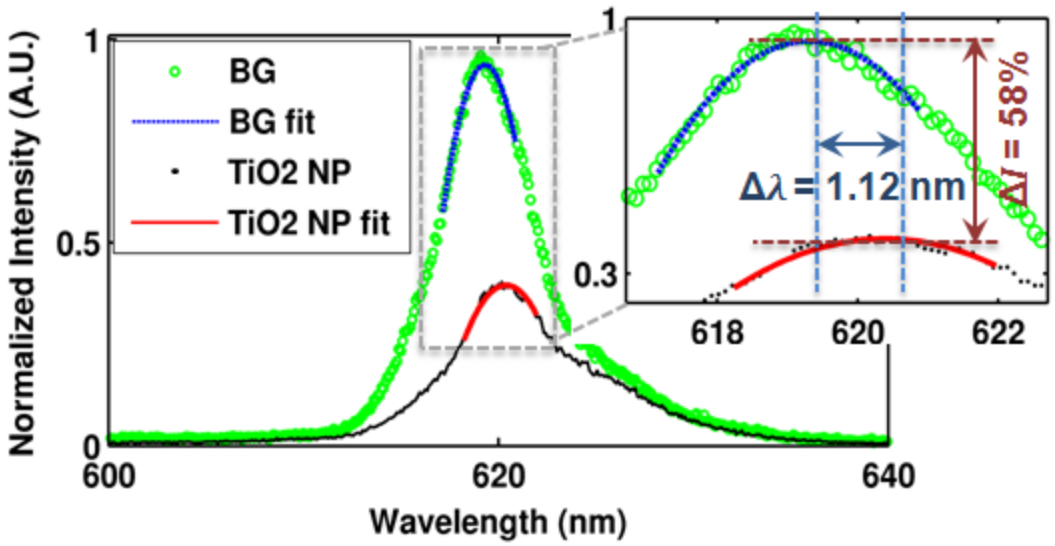

Figure 4.12 Normalized spectrum of a 500 nm TiO_2 NP and a background pixel. Inset: Zoomed in image of the normalized spectrum with 2D polynomial fitting (TiO_2 NP fitting in red line, background fitting in blue line), indicating a PWV shift of $\Delta\lambda = 1.12$ nm and a PIV reduction of $\Delta I = 58\%$ when the NP is present.

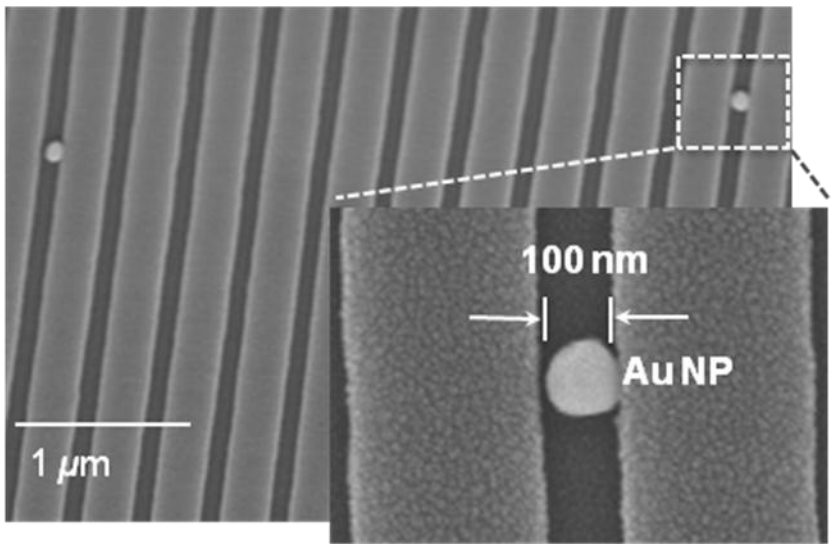

Figure 4.13 Scanning electron micrograph (SEM) of the 100 nm Au NP on PC surface. Inset: Zoomed in image.

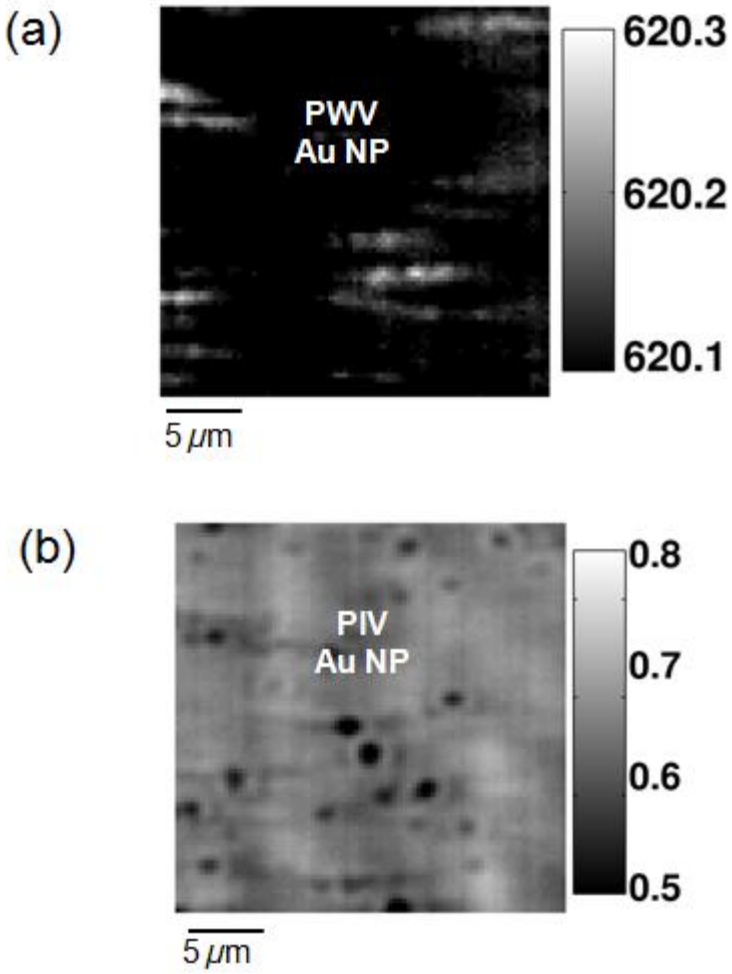

Figure 4.14 PCEM detected (a) PWV and (b) PIV images of the Au NP displayed in 2D with gray scale.

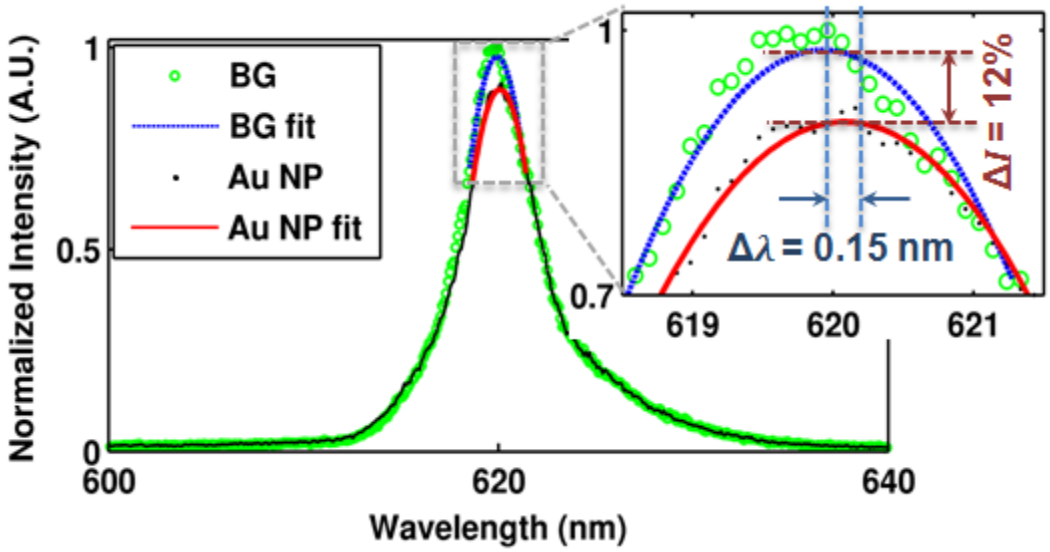

Figure 4.15 Normalized spectrum of a 100 nm Au NP and a background pixel. Inset: Zoomed in image of the normalized spectrum with 2D polynomial fitting (Au NP fitting in red line, background fitting in blue line), indicating a PWV shift of $\Delta\lambda = 0.15$ nm and a PIV reduction of $\Delta I = 12\%$ when the NP is present.

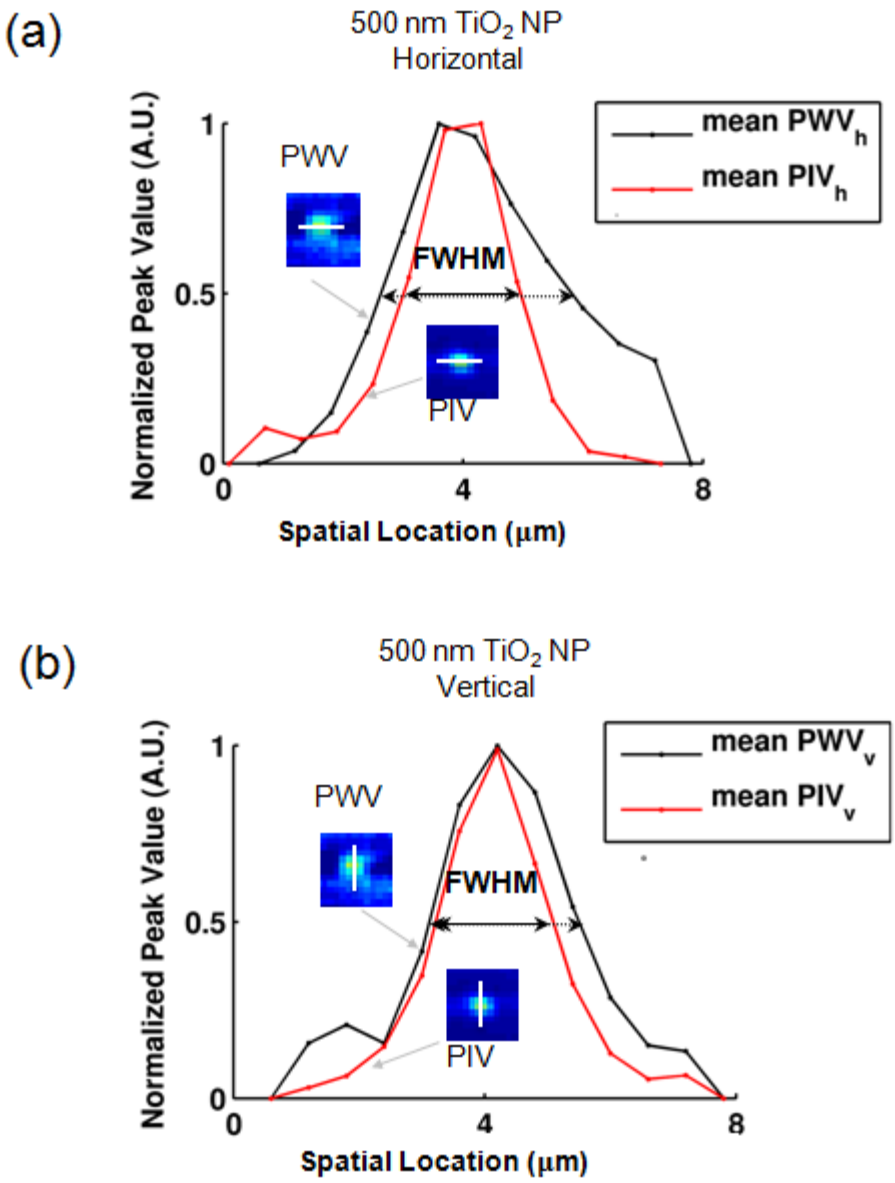

Figure 4.16 Comparison of FWHM (in horizontal and vertical directions) in PWV and PIV images detected by PCEM with randomly distributed TiO2 nanoparticles on the PC surface. FWHM (mean) in PWV and PIV images of 500 nm TiO2 NP measured by PCEM in (a) horizontal and (b) vertical directions.

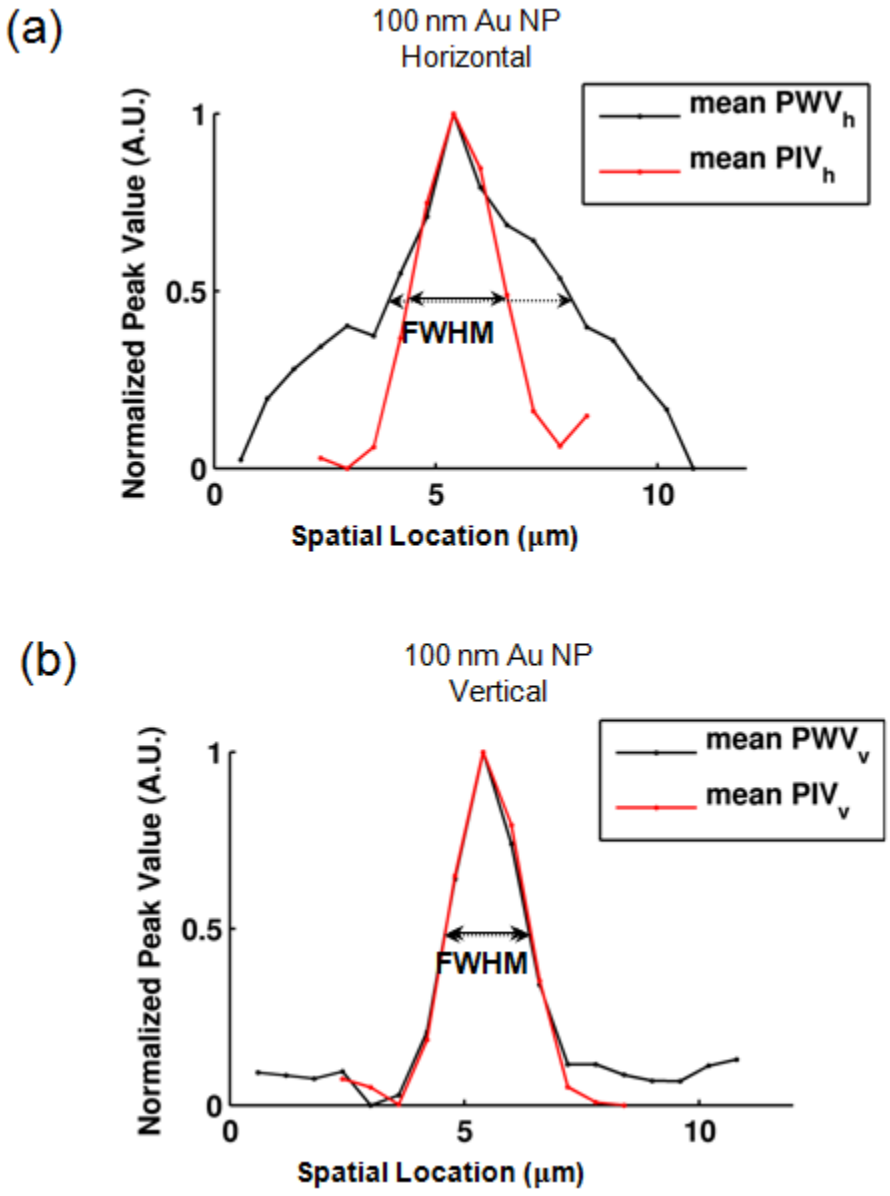

Figure 4.17 Comparison of FWHM (in horizontal and vertical directions) in PWV and PIV images detected by PCEM with randomly distributed Au nanoparticles on the PC surface. FWHM (mean) in PWV and PIV images of 100 nm Au NP measured by PCEM in (c) horizontal and (d) vertical directions.

CHAPTER 5

PROTEIN-PROTEIN BINDING DETECTION USING PCEM

5.1 Background and Motivation

Technologies to recognize the signatures of the cancer biomarkers exist for earlier cancer detection, diagnosis and pharmacological treatment, such as enzyme-linked immunosorbent assay (ELISA) [140, 141] and mass spectrometry [142]. ELISA serves as one of the important modalities for protein detection. It is based on the principle of antibody-antigen binding to recognize the target molecule and then apply fluorescence dye tag to enhance the signal. However, some restrictions exist with ELISA, such as detection limitations in terms of reliability and accuracy in earlier cancer detection which are mainly due to the insufficient sensitivity of the assay or the insufficient dynamic range needed in the low concentration of cancer biomarker detection. Conventional ELISA may detect concentration as low as several pg/mL for some protein biomarkers [143-147], but the procedure is rather complicated and may require extensive technical training. And thus it is challenging to implement it in point-of-care applications [148]. Besides, a conventional ELISA analysis typically needs more than 50 μl of blood serum, requires an expensive non-automated fluorescence detection instrument, and provides limited multiplexing capability.

Label-free methods, including surface plasmon resonance (SPR), impedance imaging, interference microscopy, phase imaging with microscopy, and photonic crystal biosensors, etc., have also been employed to detect cancer biomarkers in the past

decades. Those sensing or imaging modalities have been used for their capability of detecting or characterizing proteins in the absence of markers or fluorophore dyes. The major concept of label-free imaging methods is the use of a special transducer to capture and convert a bio-analyte's physical change into a measurable optical or electrical signal, such as a resonance wavelength shift or an electrical impedance variation. Each imaging technology has a distinct physical mechanism, and thus leads to its specific capabilities and limitations. For example, the surface plasmon resonance imaging (SPRi) is an optical detection method which usually use a prism coated with a thin metal (typically gold) layer and thus it utilizes the plasmon surface polariton fields as the illumination source instead of normal light [129]. When the incident light meet with the resonance conditions, such as certain wavelength, polarization and incident angle, the free electrons at the metal-dielectric interface will absorb the incident light photons and convert them into surface plasmon waves. Such electromagnetic modes can travel along the metal-dielectric interface as a bound, non-radiative surface wave, which has a pronounced dispersion. Its field intensity is concentrated and strongly enhanced at the interface. Those properties make SPRi sensitive to small perturbations at the metal surface which are caused by the interactions between target molecules and the probe antibodies [149]. However, low spectral resolution and long lateral propagation of SPRi hinders its usefulness for applications requiring high resolution, while photonic crystal biosensor imaging is a promising alternative for such applications.

Nanomedicine, namely applying nanotechnologies to medicine, is another emerging field which may offer new technologies to detect cancer biomarkers in earlier cancer development. Nanoparticles (NP) have great potential as biosensing tags for

protein-protein binding detection due to their nanometer scale size (comparable to biological molecules or antibodies), especially for gold nanoparticle (AuNP) with the amenability of synthesis and functionalization, less toxicity and absence of photobleaching.

In this work, we apply the PCEM system to detect the protein-protein binding upon a biosensor surface. Our ultimate goal is to apply individual nanoparticles as functionalized tags in "sandwich" style assays, which can be used to detect the presence of captured analyte attached on a PC biosensor surface (Figure 5.1). By matching the plasmon resonant frequency of the gold nanorods (AuNR) to the PC resonance substantially increases sensitivity of this biosensing approach. NP-PCEM imaging offers an attractive alternative to detection using fluorescent nanoparticles, as NP-PCEM requires only low power broadband illumination, does not suffer from photobleaching, can provide long-term time-course data, and can be utilized for any type of nanoparticle tags.

5.2 Materials and Methods

Detection of protein-protein binding, which utilizes the photonic crystal surface as the biosensor and the gold nanoparticle as sensing tags, is performed in this work. The merit of this method is to take the advantages of the high sensitivity of the photonic crystal biosensor and the capability of single nanoparticle imaging resolution of the PCEM imaging system. Moreover, metal nanoparticles, including gold nanoparticles (AuNP), scatter light intensely near their surface plasmon resonance (SPR) wavelength. The localized surface plasmon resonance (LSPR) wavelength of a gold nanoparticle can

be tuned by many factors, such as its size, aspect ratio, coating shell thickness. Hence, the LSPR wavelength of a gold nanoparticle can be conveniently tuned (see section 5.3 for more details) to match with the photonic crystal biosensor resonance to further enhance the imaging contrast.

As shown in Figure 5.2, the proposed protein-protein binding method using (NP-PCEM) can be summarized into the following steps: (1) The probe protein (e.g. Anti-IgG) is immobilized on the photonic crystal biosensor surface. (2) The target protein (e.g. IgG), which is tagged with the gold nanoparticles, is applied on the biosensor surface and will be captured by the probe protein. To tag the target protein, we use a flexible linker (e.g. SH-PEG) to link between the gold nanoparticle and the target protein. (3) After certain time of incubation of the tagged target protein with the immobilized capture protein, the unbound target protein is rinsed off and the remaining nanoparticles can be countable for protein-protein events. So the resulting photonic crystal biosensor surface is imaged with the PCEM system to measure the resonance wavelength shift and intensity variation.

5.2.1 Tuning the LSPR of Nanoparticle to Match the PC resonance

The detection efficiency will be improved if we can match the resonance wavelength of the PC biosensor with the localized surface plasmon resonance (LSPR) of the gold nanoparticle. To tune the LSPR of the nanoparticle, we can adjust its physical properties and consequently the electric-magnetic properties during the nanoparticle synthesis procedure. In this section, we introduce the Mie-Gans theory [150], which describes the relationship between the physical properties and the electric-magnetic

outcome of a non-spherical nanoparticle, to guide the gold nanoparticle synthesis procedure.

The optical extinction spectrum of a prolate metal spheroid (*e.g.* nanorod) exhibits two distinct localized surface plasmon resonances, corresponding to the two unique modes of electron oscillation along transverse and longitudinal directions. The absorption cross-section of the prolate spheroid is derived from Mie theory by Richard Gans and expressed as follows [150, 151]:

$$\sigma_{abs} = \frac{\omega}{3c}\varepsilon_m^{3/2} V \sum_j \frac{\left(1/P_j^2\right)\varepsilon_2}{\left\{\varepsilon_1 + \left[\left(1-P_j\right)/P_j\right]\varepsilon_m\right\}^2 + \varepsilon_2^2}. \tag{5-1}$$

Where, the sum over j involves the three dimensions of the nanorod. P_j (that includes P_A, P_B, and P_C) represents depolarization factors, where A>B=C for a nanorod. The depolarization values (P_j) depend on the aspect ratio of the nanorods as follows:

$$P_A = \frac{1-e^2}{e^2}\left[\frac{1}{2e}\ln\left(\frac{1+e}{1-e}\right)-1\right], \tag{5-2}$$

$$P_B = P_C = \frac{1-P_A}{2}. \tag{5-3}$$

Where e is related to aspect ratio (R) as follows:

$$e = \left(1-\frac{1}{R^2}\right)^{1/2}. \tag{5-4}$$

As evident from (5-2), the depolarization factor along the longitudinal direction (P_A) exhibits a strong dependence on aspect ratio and decreases sharply with increasing aspect ratio. The reduction in the restoring force for the longitudinal plasmon mode with increase in the aspect of ratio of AuNR results in lowering its resonance frequency (or increasing LSPR wavelength). Thus, the longitudinal plasmon band of AuNR is highly sensitive to the aspect ratio of AuNR. In aqueous solution, the longitudinal plasmon resonance wavelength (λ_{max}) is linearly proportional to the aspect ratio (R) and given by the following relationship [152, 153]:

$$\lambda_{\max} = 95R + 420. \tag{5-5}$$

Therefore, we can tune the longitudinal plasmon resonance wavelength matching with the PC resonance by tuning the aspect ratio of a gold nanorod.

5.2.2 Electromagnetic Modeling Using FDTD

The modeling of the electromagnetic field distribution around plasmonic nanorods is performed using 3D finite-difference time-domain (FDTD) technique with commercially available software (EM Explorer). FDTD simulations exploit the time and position dependence of Maxwell's equations to model electromagnetic waves in rectangular 3D cells of finite volume called Yee cells. To obtain the electromagnetic field distribution, a single AuNR of ~30×30×60 nm^3 size is modeled in a simulation domain of 300×300×200 nm^3 using p-polarized incident plane wave for illumination with Yee cell size of 2 nm. Perfectly matched layer (PML) absorbing boundary conditions are applied in all directions. The complex refractive index of gold at the extinction maximum

wavelength is set to n_{Au}=0.18+i4.96. The resulting electromagnetic distribution is shown in Figure 5.3.

5.2.3 Gold Nanoparticle Synthesis

Gold nanorods (AuNR) were synthesized using a seed-mediated approach. Seed solution was prepared by adding 0.6 mL of an ice-cold sodium borohydride solution (10 mM) into 10 mL of 0.1 M cetyltrimethylammonium bromide (CTAB) and 2.5×10^{-4} M chloroauric acid (HAuCl4) solution under magnetic stirring at room temperature. The color of the seed solution changed from yellow to brown. Growth solution was prepared by mixing 95 mL of CTAB (0.1 M), 0.5 mL of silver nitrate (10 mM), 5 mL of HAuCl4 (10 mM), and 0.55 mL of ascorbic acid (0.1 M) in the same order. The solution was homogenized by gentle stirring. To the resulting colorless solution, 0.12 mL of freshly prepared seed solution was added and aged for two weeks at room temperature. Prior to use, the AuNR solution was centrifuged at 10, 000 rpm for 10 mins to remove excess CTAB and redispersed in nanopure water (18.2 MΩ-cm). The centrifugation procedure was repeated twice.

5.2.4 PC Biosensor Surface Functionalization

The PC biosensors were functionalized using a vapor-phase aminosilane process. The aminosilane chemistry was chosen for its low background and high binding capacity to capture antibodies. The biosensors were first cleaned by isopropanol, and deionized (DI) water, dried in a stream of N_2, and then treated in an oxygen plasma system (Diener, Pico) for 10 min (power of 100 W, pressure of 0.75 mTorr). The biosensors were then

vertically placed in a glass container. At the base of the container, 100 mL of (3-aminopropyl)-dimethyl-ethoxysilane (APDMES, Sigma Aldrich, Saint Louis, MO) was placed and the top lid was securely placed over the dish. After, the glass dish with the PC biosensors was placed in a vacuum oven for an overnight incubation at a pressure of 30 Torr. After silanization, the biosensors were then washed with toluene, methanol, and DI water and dried under a stream of N_2.

5.2.5 AuNR-IgG Conjugates on PC Biosensor Surface

To a solution of heterobifunctional polyethylene glycol (SH-PEG-COOH) in water (37.5 μL, 20 μM, Mw = 5000 g/mol, Jenkem Technology), 1-ethyl-3-(3-dimethylaminopropyl) carbodiimide (EDC, Thermo Scientific), and N-hydroxy succinimide (NHS, Thermo Scientific) with the same molar ratio as SH-PEG-COOH were added followed by shaking for 1 hour. The pH of the above reaction mixture was adjusted to 7.4 by adding 10× concentrated phosphate buffered saline buffer solution, followed by the addition of rabbit immunoglobulin G (IgG) (10 μL, 75 μM, Mw = 150 kDa, Thermo Scientific). The reaction mixture was incubated for 2 h, and then filtered to remove any byproduct during the reaction using a 50 kDa filter. The final SH-PEG-IgG conjugates solution (0.75 μM) was obtained after washing with phosphate buffered saline buffer (pH 7.4) twice. AuNR-IgG conjugates solution was prepared by adding 50 μL SH-PEG-IgG conjugates solution to 1 mL twice centrifuged AuNR solution with incubation for 1 hour. The amount of SH-PEG-IgG was optimized to obtain maximum coverage of IgG on AuNR surface. Then the PC surface was exposed to AuNR-IgG

conjugates solution for 30 mins, followed by rinsing with DI water to remove the loosely bound nanorods.

5.2.6 Protein Microarray Printing

The antibodies (~5.0 mg /mL) where diluted in proprietary printing buffer (NanoInk Inc., Skokie, IL, USA); the printing buffer is formulated to keep the protein moisturized and to preserve their active and folded states. Each well atop of PC holds 4 subarrays and the glass slides hold 16 subarrays in a 4×6 format; each subarray contains 6 sets of 4 replicate spots per antibody for a total of 24 spots. Spot diameters were measured to be ~100 μm. The printed substrates were incubated in a sealed box with a desiccant for 24 hours at room temperature.

5.2.7 Nanoparticle Sandwich Immunoassay Assay

To detect the tumor necrosis factor alpha (TNF-a) antigen, the capture antibody of TNF-a with a concentration of 20 ug/mL is first immobilized on a functionalized PC biosensor. Then the different concentrations of TNF-a antigen solution is applied to biosensor surface. After certain incubation time (e.g. 3 hours in room temperature), the PC surface is rinsed off with PBST (0.01% v/v tween 20 in PBS) to remove the unbound TNF-a antigen. Then the detection antibody applied on the biosensor surface for 1 hour, followed by the incubation of streptavidin linked gold nanoparticles for 30 mins. The device is then rinsed by PBST again and then applied with DI water for imaging.

Next, the slides were placed in a 4-well format with PDMS, where each well could hold up to 20 uL. The arrays were blocked with casein blocking buffer (BioRad,

Hercules, CA) for 1 h. All incubations were performed at room temperature. The arrays were then washed three times with 0.01% (v/v) tween 20 in phosphate buffered saline (PBST) and then each well was incubated with a 10 uL mixture of different antigens concentration in casein buffer for three hours. This was followed by three rinses in PBST after the PC substrates were incubated with 10 uL of the biotinylated detection antibody mixture in each PDMS well for 1 h. The PC substrates were then washed three times with PBST, followed by the incubation with a 1 ug/ mL solution of nanoparticle conjugated streptavidin (Invitrogen) for 30 min. Finally, the devices were washed 5 times with PBST and followed by a quick dip in DI water (3 s.) to remove the salt, spin dried, and then scanned using PCEM system.

5.3 Results and Discussion

5.3.1 Detection of IgG and Anti-IgG Binding

We studied the biosensor's ability to detect target bioanalytes binding with immobilized antibody on the PC biosensor surface. To match the PC resonant wavelength, we synthesized gold nanorods (AuNR) with resonant optical absorption spectra around ~620 nm (Figure 5.4 demonstrates the TEM image of AuNR). The size of the synthesized AuNR is 66.7 nm ± 5.5 nm in length and 30.7 nm ± 4.0 nm in diameter (as analyzed in TEM images from 56 AuNRs).

Then we employed Rabbit Immunoglobulin G (IgG henceforth) as model capture biomolecule and anti-Rabbit IgG (anti-IgG) as model target bioanalyte to demonstrate the detection of antibody-antigen binding (as shown in Figure 5.2) using NP-PCEM. IgG is the one of main antibody isotypes found in the human blood and extracellular fluid to control body tissues' infection. It protects the human body from infection through many

immune mechanisms, such as binding pathogens (e.g. bacteria and viruses) and thus allowing their recognition by immune cells. IgG monomer is about 150 kDa and forms a tetrameric quaternary structure composed of four peptide chains and arranged in a "Y" shape, which contains two identical light chains (about 25 kDa) and two identical heavy chains (about 50 kDa). The two heavy chains are linked to each other and each heavy chain is linked to a light chain with disulfide bonds, which forms a shape of a "fork" containing an identical antigen binding site. In clinic, IgG can be measured and therefore considered as a diagnostic tool for certain diseases, such as hepatitis B virus, chickenpox, or mumps, etc.

Figure 5.5 illustrates the binding of biomolecules to target bioanalytes attached to the PC biosensor surface. In this setup, thiol-terminated polyethylene glycol (SH-PEG), a hydrophilic polymer, serves as a flexible linker to increase the accessibility of IgG to target bioanalyte [154, 155]. The AuNR-IgG conjugates were prepared by functionalizing AuNRs with SH-PEG-IgG molecules. Subsequently, anti-IgG was adsorbed onto the PC biosensor surface by exposing the PC to anti-IgG solution followed by thorough rinsing with PBS to remove the weakly adsorbed antibody. Exposing the PC surface to AuNR-IgG conjugates resulted in specific binding to anti-IgG (SEM images shown in Figure 5.6), which can be detected as a PIV reduction in the area absorbed with AuNR. Figure 5.7(a) shows the mathematical difference between two PIV images taken before and after AuNR-IgG attachment and selected cross-section lines in the PIV images (Figure 5.7(b)). It demonstrates that PCEM can successfully detect the intensity reduction in presence of AuNR-IgG.

5.3.2 PCEM Imaging with Microarrays of Cancer Biomarkers

A microarray is a large array of small biological material spots bound to the functionalized substrate surface. Each of the spots contains different capture molecules and the then probe molecules, typically tagged with a fluorescent dye, can be added to the array to indicate the protein-protein interactions or gene expressions. Therefore, microarray can perform high-throughput tracking of interactions and activities of proteins or DNAs and hence achieve rapid and economical detections while only consuming a small amount of samples and reagents. Sandwich antibody microarray has been reported to use a small amount of sample (e.g. 3~10 µl) to detect low concentrations of analytes (e.g. ~10 pg/ml) [38, 39]. It also demonstrates the detection capability of fast binding kinetics, lacking of assay cross-reactivity, and providing lower limits of detection. However, conventional protein microarrays can generally only be scanned a few times after the label step due to the utilizing of fluorescent dye as reporters, and thus it lacks of capability to capture kinetics information. Besides, it requires the exposure of capture antibody array to the test sample solution for a long period of time, especially for detection of low detection limits range (e.g. 1~10 pg/ml). Recently, protein microarrays, together with the use of photonic crystal biosensors to enhance fluorescence, have been shown to extend the detection limits down to the range of 0.1~1 pg/ml in our lab [156].

We next printed the microarray of biotinylated detection antibody (anti-TNF-a) with a concentration of 10 ug/ml on the photonic crystal biosensor surface. After a certain time of incubation (e.g. 24 hours), the unbound antibody is rinsed off from the biosensor surface. Then, the NHS linked gold nanoparticle solution is exposed to the biosensor surface. To compare the detection results, a control experiment is performed with a

similar procedure, except utilizing streptavidin linked Cy5 fluorescence dye (10 ug/mL) to tag the detection antibody. The measured printed spot size is around 100 um in diameter and the resulting peak intensity and wavelength shift images images are shown in Figure 5.8.

5.3.3 Detection of Cancer Biomarkers with Sandwich Assay

Next, we performed an antibody-antigen-antibody sandwich immunoassay to verify the PCEM detection performance tagged with nanoparticles. As shown in Figure 5.9, the proposed antibody-antigen-antibody binding detection modality using (NP-PCEM) can be decomposed into the following steps: (1) the capture antibody (or primary antibody) is immobilized on the photonic crystal biosensor surface; (2) the target antigen solution is applied on the biosensor surface and will be captured by the capture antibody; (3) then the solution of detection antibody (secondary antibody) is applied to the mixture solution in step 2 to bind with the antigen; (4) finally the gold nanoparticles are applied to the mixture solution in step 3.

Detection of tumor necrosis factor alpha (TNF-a) is demonstrated in this section as an example. TNF-a is an adipokine involved in systemic inflammation and can be produced by activated macrophages. It is also an endogenous pyrogen and can regulate the immune cells through inducing fever, cell apoptosis, or inhibiting tumorigenesis. TNF-a contains 212 amino acids and is a cellular transmembrane protein which can activate the NF-κB and MARK pathways or induce death in cell signaling pathways. Failure of normal TNF-a regulation can lead to severe diseases, such as cancer, depression, Alzheimer's disease, just to name a few.

Photonic crystal biosensors were mounted with the PDMS well and four replicate microspots with capture antibodies for TNF-a were printed on the biosensor surface in each well using a nanoplotter system. A TNF-a antigen was assayed in these wells over a range of 6 concentrations (in a 3-fold dilution series) starting with 0.1 ng/mL. PIV images for the nanopartile were acquired using the PCEM imaging system, as shown in Figure 5.10. Figure 5.11 demonstrates the dose-dependent response of each antigen assays. Currently the lowest concentration of TNF-a detected on the PC surface was about 10 ng/mL. The results demonstrate that NP-PCEM can successfully detect the dose-dependent response of the target antigen. However, the low concentration response lacks of accuracy and it is likely due to the linker (NHS) between the gold nanoparticle and the detection antibody is not specific binding. This non-specific binding may result the binding of nanoparticle with the capture antibody. Future work can be extended to switch the non-specific linker to linker between a pair of specific molecules. For example, biotin and streptavidin which are known having one of the strongest non-covalent interactions in nature, can be used as a pair of linking proteins to link between the detection antibody and the gold nanoparticle.

5.4 Figures

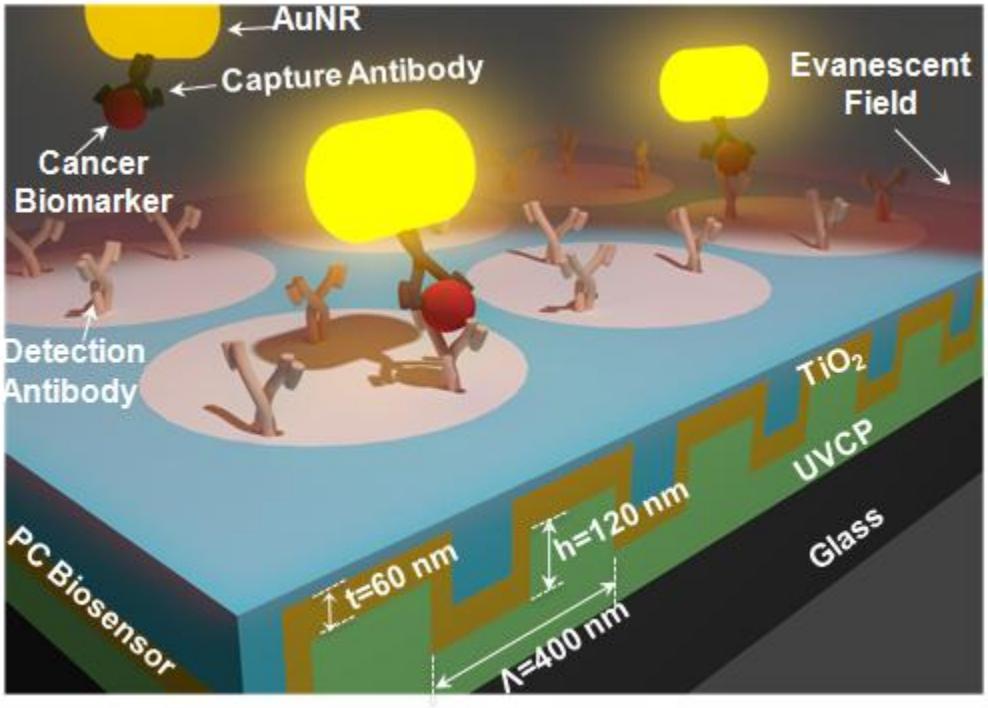

Figure 5.1 The Schematic Diagram of PCEM detection of protein-protein binding.

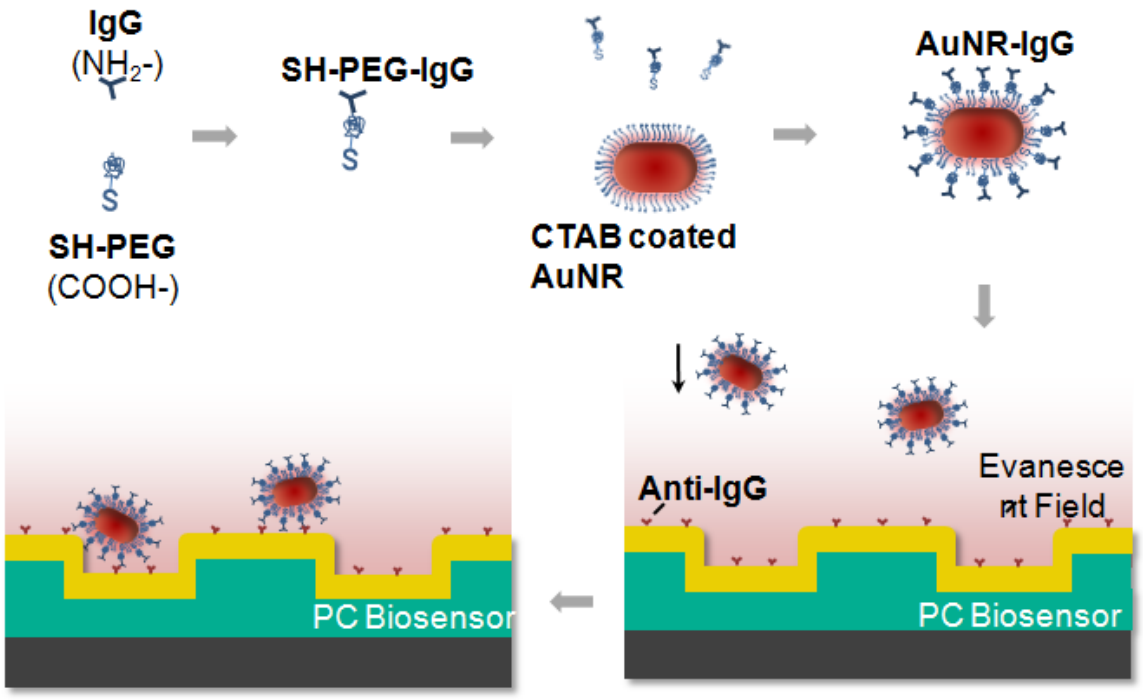

Figure 5.2 The Schematic Diagram of Protein-protein Binding Method using (NP-PCEM): The probe protein (e.g. Anti-IgG) is immobilized on the photonic crystal biosensor surface. Then the target protein (e.g. IgG) is tagged with the gold nanoparticles and applied on the biosensor surface and will be captured by the probe protein. After incubation of the tagged target protein on PC surface, the unbound target protein is rinsed off and the remaining nanoparticles can be countable for protein-protein events.

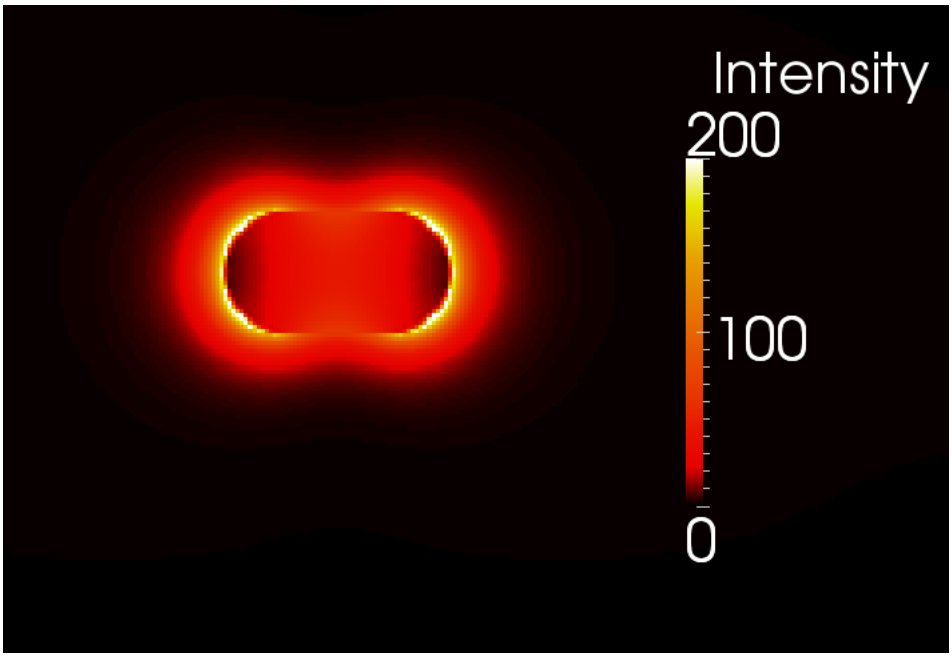

Figure 5.3 The result of computer simulation for electromagnetic distribution of a single nanorod.

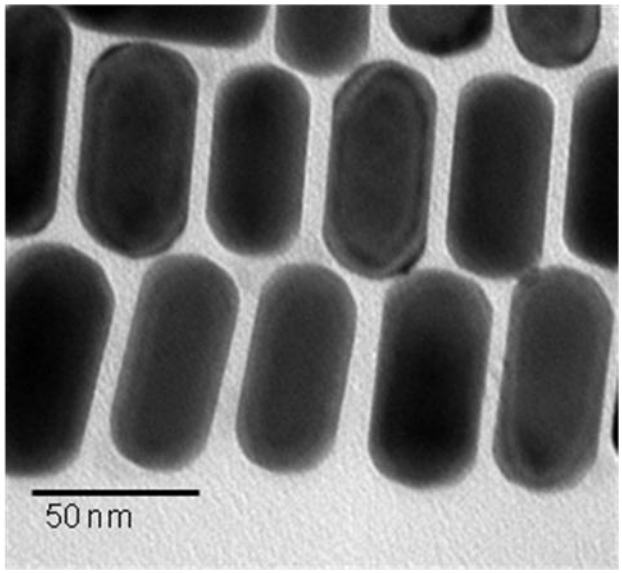

Figure 5.4 Transmission electron microscopy (TEM) images of synthesized gold nanorods (AuNR).

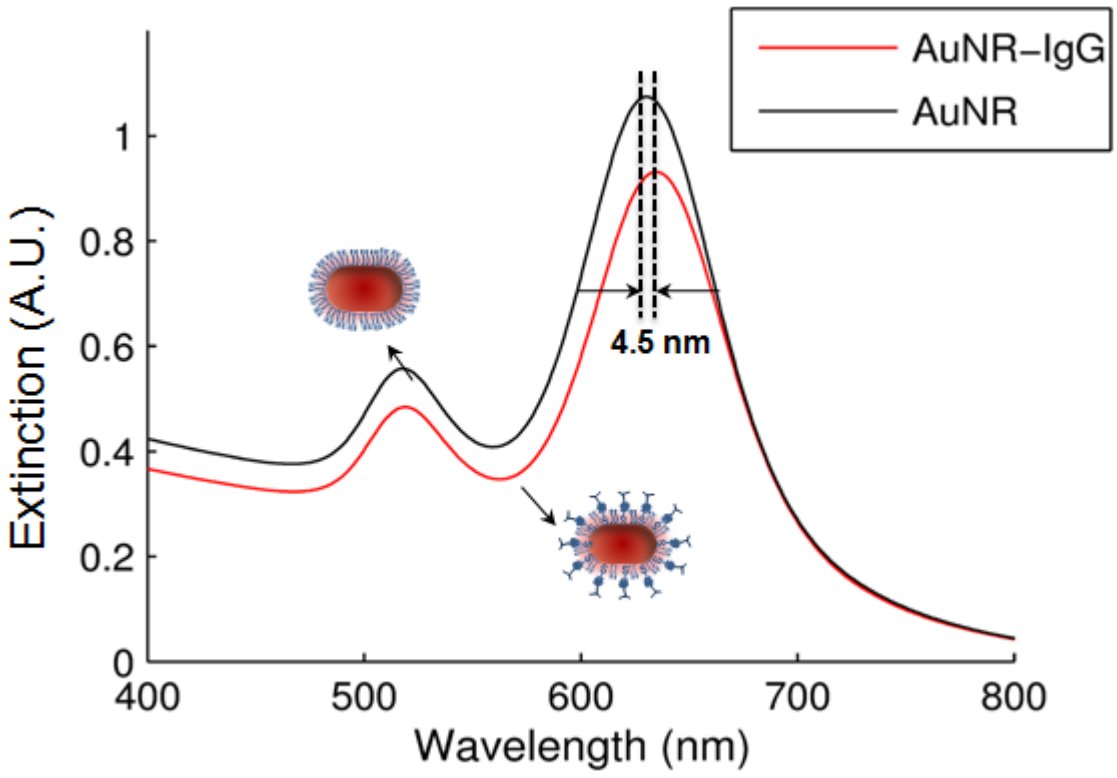

Figure 5.5 UV-vis extinction spectra confirm the conjugation between AuNR and SH-PEG-IgG.

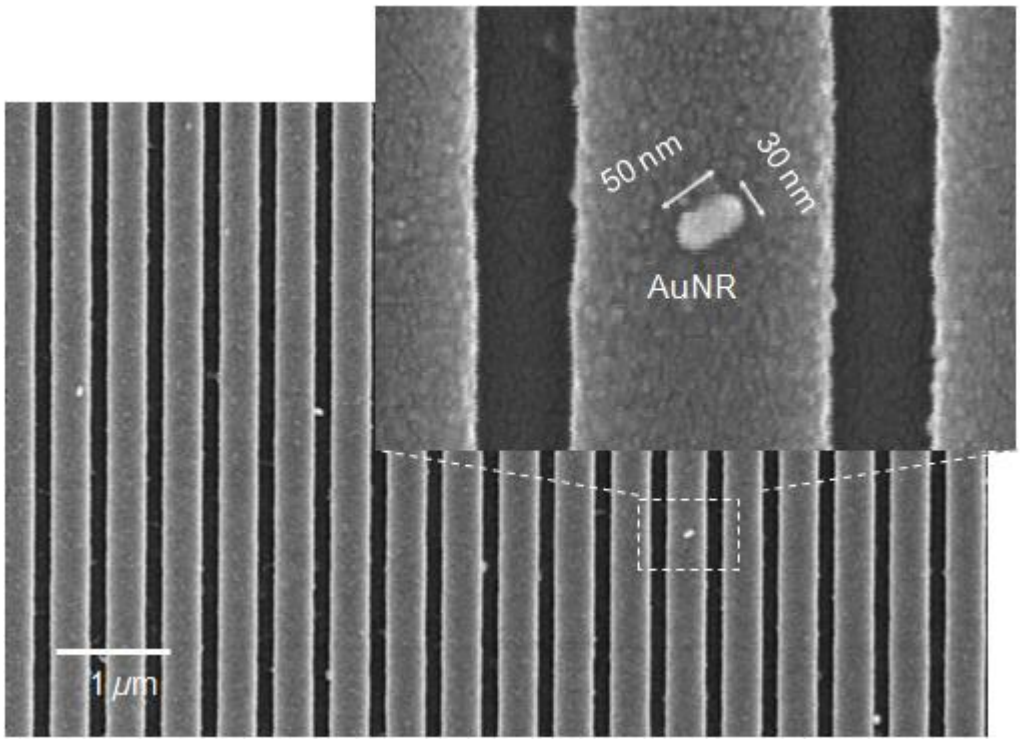

Figure 5.6 Scanning electron microscope (SEM) images of AuNR-IgG attached on PC biosensor surface. Inset: Zoomed in SEM image.

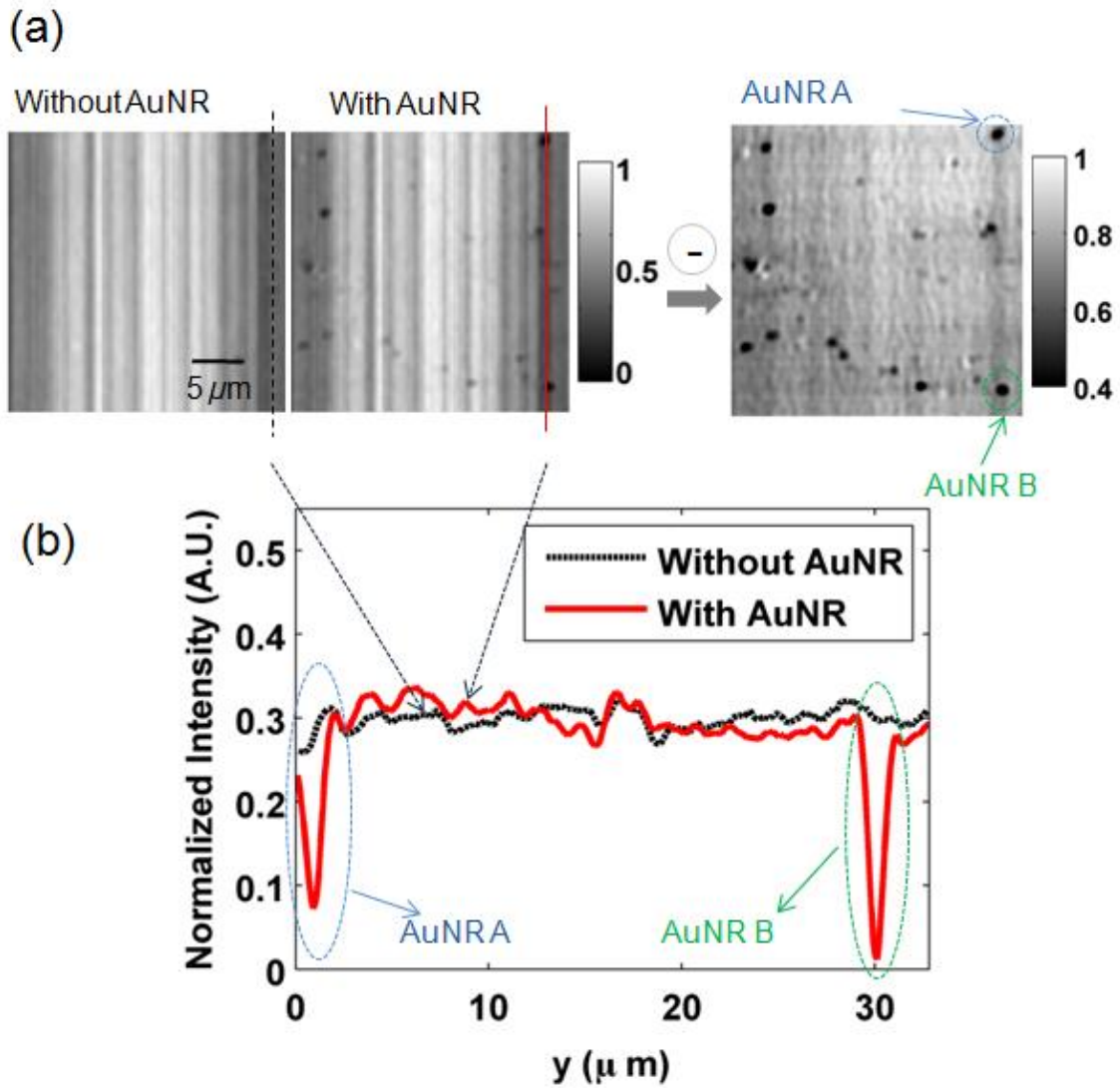

Figure 5.7 PCEM detection of protein-protein binding. (a) PCEM detected PIV images (in gray scale) for the difference between without and with AuNR-IgG on PC surface. (b) Two representative cross-section lines of the normalized intensity images for without and with two AuNRs-IgG on PC surface.

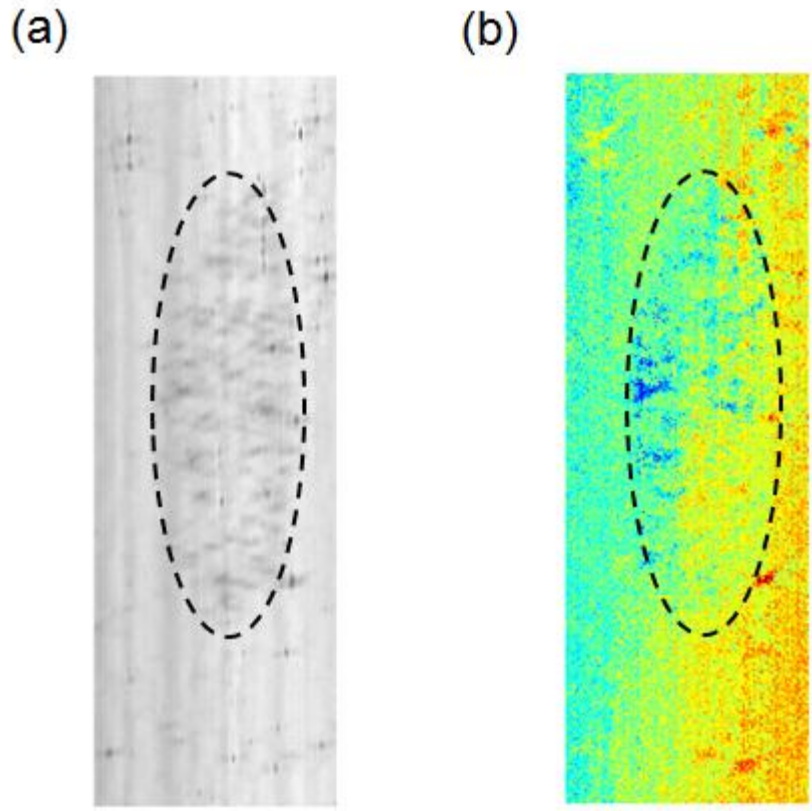

Figure 5.8 PCEM detection of anti-TNF-a with nanoparticles in printed microspots (a) peak intensity change (in gray scale) and (b) peak wavelength shift images.

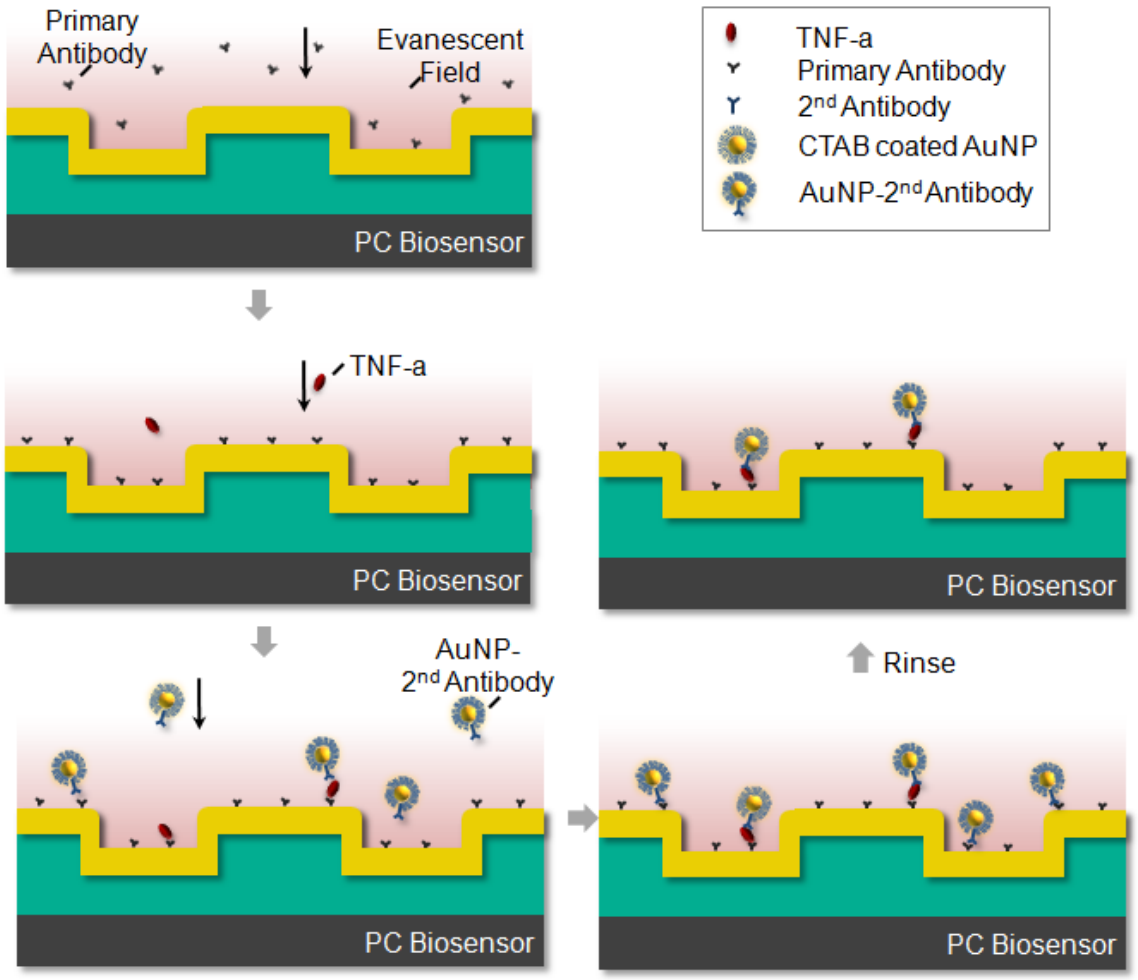

Figure 5.9 The Proposed Protein-protein Binding Method using (NP-PCEM). (a) the capture antibody is immobilized on the biosensor surface; (b) the target antigen solution is applied on the biosensor surface and will be captured by the capture antibody; (c) the solution of gold nanoparticles tagged detection antibody is applied on the sensor surface; (d) The detection antibody bind with the antigen; (e) Rinse off the unbound detection antibody.

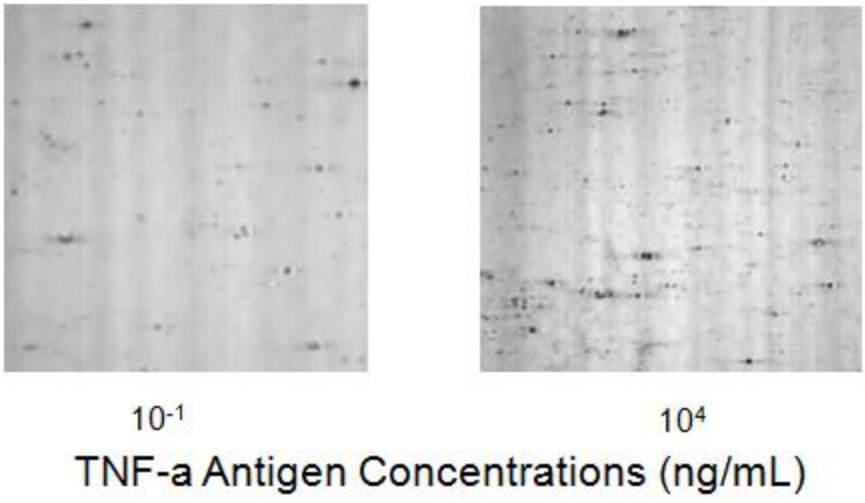

Figure 5.10 PIV images for the nanoparticle were acquired using the PCEM imaging system.

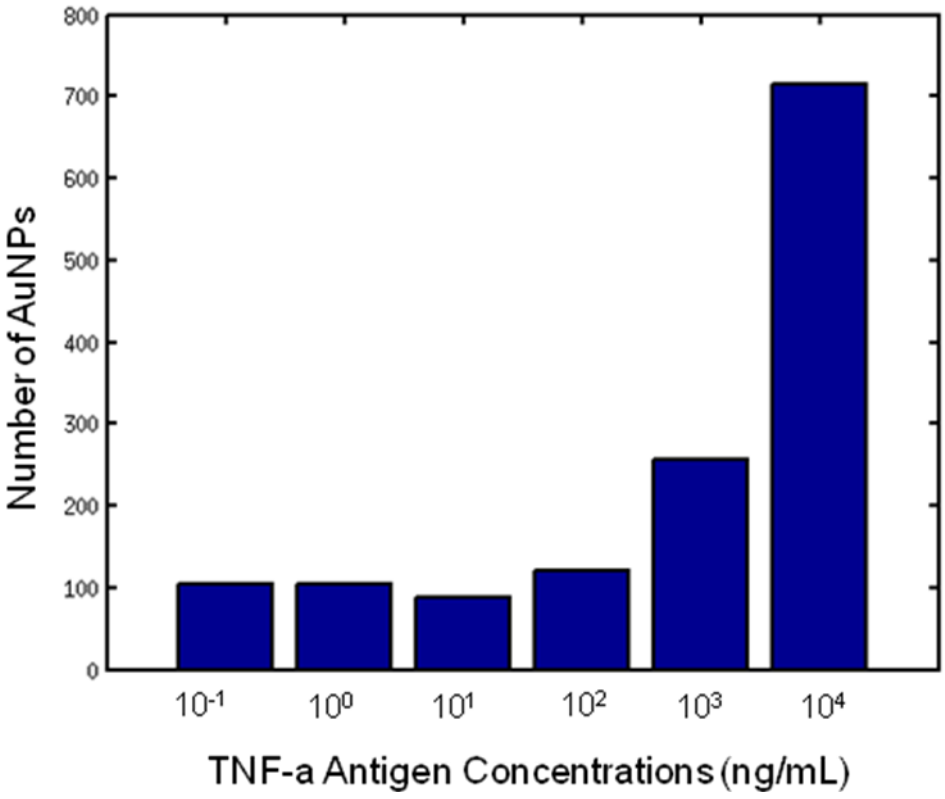

Figure 5.11 The dose-dependent response of each TNF-a antigen assays detected using PCEM system.

CHAPTER 6

CONCLUSIONS AND FUTURE OUTLOOK

6.1 Conclusions

Our group has previously proposed the use of photonic crystal as a versatile biosensor. In this work, we applied this tool to imaging of live cells, nanoparticles and protein-protein binding. In the process, we have extended the acquisition system to adapt to the specific requirements of each problem. Namely, we have integrated bright-field imaging for cell imaging (crucial to validate the detection of adhering cells), reduced the acquisition time by optimizing the scanning procedure and developed image analysis tools to allow the calculation of quantitative measurements (cell displacement and nanoparticle counting). Results from live-cell imaging suggest that the photonic crystal can successfully detect live cell during adhesion, migration and differentiation. The temporospatial analysis software offers movel measures of the dynamic change of cell plasma membrane during cellular activity. Owing to the narrow spectra resolution and short lateral propagation, photonic crystal biosensor is able to detect the particles in nanometer scale without any labeling. This novel technique can be utilized to detect protein-protein binding (tagged with nanoparticle) while avoiding the photobleach issue which would otherwise appear if using fluorescence tagged biosensing techniques. Each of these studies is a stepping stone towards to the ultimate goal of sensing for biological phenomena and it is expected to provide guidance to the future development of the biosensing technology.

6.2 Future Outlook

One of the ultimate goals of a biosensor is to detect or monitor the interaction among biological samples in their nature format with high sensitivity. Photonic crystal biosensor shows great promise to this goal and can potentially serve as the candidate for the next generation biosensing modality. The experimental results and the imaging analysis in this dissertation make a strong case for the application of the photonic crystal enhanced microscopy as an ideal scheme for biosensing and bioimaging, especially for live cell imaging and protein-protein binding detection. Nevertheless, there is room for the further improvement of the PCEM imaging system, such as:

- Improving the signal-to-noise ratio:

The signal in label-free nanoparticle detection, due to the presence of reacting particles on the top of the surface, currently measured at the output spectrometer is degraded by noise, which can sometimes have a comparable level with the signal itself. Therefore, any improvement in the imaging contrast, including changes to the optical light path, would result in a net gain in system's accuracy.

- Integration of multi-illumination and imaging modality:

Iin order to validate the results from cell-imaging, it would be useful to have the ability to combine fluorescence and label-free PCEM imaging of the same cell simultaneously.

- Continued improvements to the imaging acquisition and analysis software:

While the current tools proved satisfactory for this work, cell tracking could benefit from more robustness. If the spline mapping operation can be improved, the level-set method would not be necessary and thus resulting in faster boundary tracking. Similarly, the nanoparticle counting procedure is limited when dealing with clustered nanoparticles. Such case are typically challenging segmentation problems, for which extensive research has be done, advanced methods may therefore be applied to improve the robustness of the imaging and analysis system.

Future applications will incorporate the above points and further advance the photonic crystal enhanced microscopy system.

REFERENCES

[1] N. J. Boudreau and P. L. Jones, "Extracellular matrix and integrin signalling: the shape of things to come," *Biochem. J.*, vol. 339, pp. 481-488, 1999.

[2] M. Barczyk, S. Carracedo, and D. Gullberg, "Integrins," *Cell Tissue Res.*, vol. 339, pp. 269-280, 2010.

[3] B. D. Hoffman, C. Grashoff, and M. A. Schwartz, "Dynamic molecular processes mediate cellular mechanotransduction," *Nature*, vol. 475, pp. 316-23, Jul 21 2011.

[4] T. Pawson, "Protein modules and signalling networks," *Nature*, vol. 373, pp. 573-80, Feb 16 1995.

[5] D. A. Fletcher and R. D. Mullins, "Cell mechanics and the cytoskeleton," *Nature*, vol. 463, pp. 485-92, Jan 28 2010.

[6] R. H. Pritchard, Y. Y. Huang, and E. M. Terentjev, "Mechanics of biological networks: from the cell cytoskeleton to connective tissue," *Soft Matter*, vol. 10, pp. 1864-84, Mar 28 2014.

[7] N. Khatibzadeh, A. A. Spector, W. E. Brownell, and B. Anvari, "Effects of plasma membrane cholesterol level and cytoskeleton F-actin on cell protrusion mechanics," *PLoS One*, vol. 8, p. e57147, 2013.

[8] T. Zhang, "Cytoplasmic motion induced by cytoskeleton stretching and its effect on cell mechanics," *Mol Cell Biomech*, vol. 8, pp. 169-93, Sep 2011.

[9] S. Wang, H. Arellano-Santoyo, P. A. Combs, and J. W. Shaevitz, "Actin-like cytoskeleton filaments contribute to cell mechanics in bacteria," *Proc Natl Acad Sci U S A*, vol. 107, pp. 9182-5, May 18 2010.

[10] I. Titushkin and M. Cho, "Regulation of cell cytoskeleton and membrane mechanics by electric field: role of linker proteins," *Biophys J*, vol. 96, pp. 717-28, Jan 2009.

[11] S. Gruenheid and B. B. Finlay, "Microbial pathogenesis and cytoskeletal function," *Nature*, vol. 422, pp. 775-81, Apr 17 2003.

[12] J. Howard and A. A. Hyman, "Dynamics and mechanics of the microtubule plus end," *Nature*, vol. 422, pp. 753-8, Apr 17 2003.

[13] S. W. Moore and M. P. Sheetz, "Biophysics of Substrate Interaction: Influence on Neural Motility, Differentiation, and Repair," *Dev Neurobiol.*, vol. 71, pp. 1090-1101, 2011.

[14] M. P. Sheetz, "Cell control by membrane-cytoskeleton adhesion," *Nat Rev Mol Cell Biol.*, vol. 2, pp. 392-396, 2001.

[15] J. T. Parsons, A. R. Horwitz, and M. A. Schwartz, "Cell adhesion: integrating cytoskeletal dynamics and cellular tension," *Nat Rev Mol Cell Biol*, vol. 11, pp. 633-43, Sep 2010.

[16] P. Roca-Cusachs, T. Iskratsch, and M. P. Sheetz, "Finding the weakest link – exploring integrin-mediated mechanical molecular pathways," *J Cell Sci.*, vol. 125, pp. 3025-3038, 2012.

[17] S. K. Mitra, D. A. Hanson, and D. D. Schlaepfer, "Focal adhesion kinase: in command and control of cell motility," *Nat Rev Mol Cell Biol,* vol. 6, pp. 56-68, Jan 2005.
[18] M. R. Morgan, M. J. Humphries, and M. D. Bass, "Synergistic control of cell adhesion by integrins and syndecans," *Nat Rev Mol Cell Biol,* vol. 8, pp. 957-69, Dec 2007.
[19] J. C. Kuo, "Mechanotransduction at focal adhesions: integrating cytoskeletal mechanics in migrating cells.," *J Cell Mol Med.,* vol. 17, pp. 704-712, 2013.
[20] K. H. Nakayama, L. Hou, and N. F. Huang, "Role of extracellular matrix signaling cues in modulating cell fate commitment for cardiovascular tissue engineering," *Adv Healthc Mater,* vol. 3, pp. 628-41, May 2014.
[21] S. V. Plotnikov and C. M. Waterman, "Guiding cell migration by tugging," *Curr Opin Cell Biol,* vol. 25, pp. 619-26, Oct 2013.
[22] B. P. Head, H. H. Patel, and P. A. Insel, "Interaction of membrane/lipid rafts with the cytoskeleton: impact on signaling and function: membrane/lipid rafts, mediators of cytoskeletal arrangement and cell signaling," *Biochim Biophys Acta,* vol. 1838, pp. 532-45, Feb 2014.
[23] S. Stehbens and T. Wittmann, "Targeting and transport: how microtubules control focal adhesion dynamics.," *J Cell Biol.,* vol. 198, pp. 481-489, 2012.
[24] J. A. Spudich, "How molecular motors work," *Nature,* vol. 372, pp. 515-518, 1994.
[25] L. A. Liotta and E. C. Kohn, "The microenvironment of the tumour-host interface," *Nature,* vol. 411, pp. 375-9, May 17 2001.
[26] H. T. McMahon and J. L. Gallop, "Membrane curvature and mechanisms of dynamic cell membrane remodelling," *Nature,* vol. 438, pp. 590-6, Dec 1 2005.
[27] M. C. Raff, "T and B lymphocytes and immune responses," *Nature,* vol. 242, pp. 19-23, Mar 2 1973.
[28] M. Baggiolini, "Chemokines and leukocyte traffic," *Nature,* vol. 392, pp. 565-8, Apr 9 1998.
[29] H. E. Huxley, "Muscular contraction and cell motility," *Nature,* vol. 243, pp. 445-9, Jun 22 1973.
[30] T. Graf and T. Enver, "Forcing cells to change lineages," *Nature,* vol. 462, pp. 587-94, Dec 3 2009.
[31] I. J. Fox, G. Q. Daley, S. A. Goldman, J. Huard, T. J. Kamp, and M. Trucco, "Stem cell therapy. Use of differentiated pluripotent stem cells as replacement therapy for treating disease," *Science,* vol. 345, p. 1247391, 2014.
[32] C. Blanpain and E. Fuchs, "Stem cell plasticity. Plasticity of epithelial stem cells in tissue regeneration," *Science,* vol. 344, p. 1242281, Jun 13 2014.
[33] M. H. Sieweke and J. E. Allen, "Beyond stem cells: self-renewal of differentiated macrophages," *Science,* vol. 342, p. 1242974, Nov 22 2013.
[34] C. Furusawa and K. Kaneko, "A dynamical-systems view of stem cell biology," *Science,* vol. 338, pp. 215-7, Oct 12 2012.
[35] F. Geissmann, M. G. Manz, S. Jung, M. H. Sieweke, M. Merad, and K. Ley, "Development of monocytes, macrophages, and dendritic cells," *Science,* vol. 327, pp. 656-61, Feb 5 2010.

[36] J. P. Medema and L. Vermeulen, "Microenvironmental regulation of stem cells in intestinal homeostasis and cancer," *Nature,* vol. 474, pp. 318-26, Jun 16 2011.
[37] A. J. Engler, S. Sen, H. L. Sweeney, and D. E. Discher, "Matrix elasticity directs stem cell lineage specification," *Cell,* vol. 126, pp. 677-89, Aug 25 2006.
[38] J. H. Wen, L. G. Vincent, A. Fuhrmann, Y. S. Choi, K. C. Hribar, H. Taylor-Weiner, S. Chen, and A. J. Engler, "Interplay of matrix stiffness and protein tethering in stem cell differentiation," *Nat Mater,* vol. 13, pp. 979-87, Oct 2014.
[39] W. L. Murphy, T. C. McDevitt, and A. J. Engler, "Materials as stem cell regulators," *Nature Materials,* vol. 13, pp. 547-557, 2014.
[40] A. N. Bhatt, R. Mathur, A. Farooque, A. Verma, and B. S. Dwarakanath, "Cancer biomarkers - current perspectives," *Indian J Med Res,* vol. 132, pp. 129-49, Aug 2010.
[41] K. Mabert, M. Cojoc, C. Peitzsch, I. Kurth, S. Souchelnytskyi, and A. Dubrovska, "Cancer biomarker discovery: current status and future perspectives," *Int J Radiat Biol,* vol. 90, pp. 659-77, Aug 2014.
[42] M. R. Mehan, R. Ostroff, S. K. Wilcox, F. Steele, D. Schneider, T. C. Jarvis, G. S. Baird, L. Gold, and N. Janjic, "Highly multiplexed proteomic platform for biomarker discovery, diagnostics, and therapeutics," *Adv Exp Med Biol,* vol. 735, pp. 283-300, 2013.
[43] H. J. Issaq, S. D. Fox, K. C. Chan, and T. D. Veenstra, "Global proteomics and metabolomics in cancer biomarker discovery," *J Sep Sci,* vol. 34, pp. 3484-92, Dec 2011.
[44] P. Indovina, E. Marcelli, P. Maranta, and G. Tarro, "Lung cancer proteomics: recent advances in biomarker discovery," *Int J Proteomics,* vol. 2011, p. 726869, 2011.
[45] J. E. Bibault, I. Fumagalli, C. Ferte, C. Chargari, J. C. Soria, and E. Deutsch, "Personalized radiation therapy and biomarker-driven treatment strategies: a systematic review," *Cancer Metastasis Rev,* vol. 32, pp. 479-92, Dec 2013.
[46] J. A. Ludwig and J. N. Weinstein, "Biomarkers in cancer staging, prognosis and treatment selection," *Nat Rev Cancer,* vol. 5, pp. 845-56, Nov 2005.
[47] A. K. Füzéry, J. Levin, M. M. Chan, and D. W. Chan, "Translation of proteomic biomarkers into FDA approved cancer diagnostics: issues and challenges.," *Clin Proteomics,* vol. 10, p. 13, 2013.
[48] M. T. Weigel and M. Dowsett, "Current and emerging biomarkers in breast cancer: prognosis and prediction," *Endocr Relat Cancer,* vol. 17, pp. R245-62, Dec 2010.
[49] E. P. Diamandis, "The failure of protein cancer biomarkers to reach the clinic: why, and what can be done to address the problem?," *BMC Med.,* vol. 10, 2012.
[50] E. J. Ambrose, "A surface contact microscope for the study of cell movements," *Nature,* vol. 178, p. 1194, Nov 24 1956.
[51] D. Axelrod, "Cell-substrate contacts illuminated by total internal reflection fluorescence," *J Cell Biol,* vol. 89, pp. 141-5, Apr 1981.
[52] Y. Sako, S. Minoghchi, and T. Yanagida, "Single-molecule imaging of EGFR signalling on the surface of living cells," *Nat Cell Biol,* vol. 2, pp. 168-72, Mar 2000.

[53] A. J. Cunningham, *Introduction to Bioanaytical Sensors*. New York: John Wiley & Sons, 1998.
[54] M. Nirschl, F. Reuter, and J. Vörös, "Review of Transducer Principles for Label-Free Biomolecular Interaction Analysis," *Biosensors,* vol. 1, pp. 70-92, 2011.
[55] F. Hook, J. Voros, M. Rodahl, R. Kurrat, P. Boni, J. J. Ramsden, M. Textor, N. D. Spencer, P. Tengvall, J. Gold, and B. Kasemo, "A comparative study of protein adsorption on titanium oxide surfaces using in situ ellipsometry, optical waveguide lightmode spectroscopy, and quartz crystal microbalance/dissipation," *Colloids and Surfaces B: Biointerfaces,* vol. 24, p. 155, 2002.
[56] D. S. Ballantine, R. M. White, S. J. Martin, A. J. Ricco, E. T. Zellers, G. C. Frye, and H. Wohltjen, *Acoustic Wave Sensors: Theory, Design, and Physico-Chemical Application*. San Diego: Academic Press, 1997.
[57] X. Fan, I. M. White, S. I. Shopova, H. Zhu, J. D. Suter, and Y. Sun, "Sensitive optical biosensors for unlabeled targets: a review," *Anal Chim Acta,* vol. 620, pp. 8-26, Jul 14 2008.
[58] H. M. Haake, A. Schutz, and G. Gauglitz, "Label-free detection of biomolecular interaction by optical sensors," *Fresenius J Anal Chem,* vol. 366, pp. 576-85, Mar-Apr 2000.
[59] G. Gauglitz and G. Proll, "Strategies for label-free optical detection," *Adv Biochem Eng Biotechnol,* vol. 109, pp. 395-432, 2008.
[60] J. Homola, S. S. Yee, and G. Gauglitz, "Surface plasmon resonance sensors: review," *Sensors and Actuators B: Chemical,* vol. 54, pp. 3-15, 1999.
[61] J. Homola, "Present and future of surface plasmon resonance biosensors," *Anal Bioanal Chem,* vol. 377, pp. 528-39, Oct 2003.
[62] X. D. Hoa, A. G. Kirk, and M. Tabrizian, "Towards integrated and sensitive surface plasmon resonance biosensors: a review of recent progress," *Biosens Bioelectron,* vol. 23, pp. 151-60, Sep 30 2007.
[63] J. Homola, "Surface plasmon resonance sensors for detection of chemical and biological species," *Chem Rev,* vol. 108, pp. 462-93, Feb 2008.
[64] B. Liedberg, C. Nylander, and I. Lunström, "Surface plasmon resonance for gas detection and biosensing," *Sensors and Actuators,* vol. 4, p. 299, 1983.
[65] I. D. Block, L. L. Chan, and B. T. Cunningham, "Photonic crystal optical biosensor incorporating structured low-index porous dielectric," *Sensor Actuators B-Chem,* vol. 120, pp. 187-193, Dec 14 2006.
[66] W. Chen, K. D. Long, M. Lu, V. Chaudhery, H. Yu, J. S. Choi, J. Polans, Y. Zhuo, B. A. Harley, and B. T. Cunningham, "Photonic crystal enhanced microscopy for imaging of live cell adhesion," *Analyst,* vol. 138, pp. 5886-94, Oct 21 2013.
[67] B. T. Cunningham, P. Li, B. Lin, and J. Pepper, "Colorimetric resonant reflection as a direct biochemical assay technique," *Sensor Actuators B-Chem,* vol. 81, pp. 316-328, Jan 5 2002.
[68] B. T. Cunningham, P. Li, S. Schulz, B. Lin, C. Baird, J. Gerstenmaier, C. Genick, F. Wang, E. Fine, and L. Laing, "Label-free assays on the BIND system," *J Biomol Screen,* vol. 9, pp. 481-490, Sep 2004.

[69] B. T. Cunningham, B. Lin, J. Qiu, P. Li, J. Pepper, and B. Hugh, "A plastic colorimetric resonant optical biosensor for multiparallel detection of label-free biochemical interactions," *Sensor Actuators B-Chem,* vol. 85, pp. 219-226, Jul 25 2002.
[70] N. Ganesh, I. D. Block, and B. T. Cunningham, "Near ultraviolet-wavelength photonic-crystal biosensor with enhanced surface-to-bulk sensitivity ratio," *Applied Physics Letters,* vol. 89, pp. 023901-023903, Jul 2006.
[71] P. C. Mathias, S. I. Jones, H. Y. Wu, F. Yang, N. Ganesh, D. O. Gonzalez, G. Bollero, L. O. Vodkin, and B. T. Cunningham, "Improved Sensitivity of DNA Microarrays Using Photonic Crystal Enhanced Fluorescence," *Analytical Chemistry,* vol. 82, pp. 6854-6861, Aug 15 2010.
[72] D. Threm, Y. Nazirizadeh, and M. Gerken, "Photonic crystal biosensors towards on-chip integration," *J Biophotonics,* Jun 8 2012.
[73] B. Lin, P. Li, and B. T. Cunningham, "A Label-Free Biosensor-Based Cell Attachment Assay for Characterization of Cell Surface Molecules," *Sensors and Actuators B,* vol. 114, pp. 559-564, 2006.
[74] R. W. Wood, "On a remarkable case of uneven distribution of light in a diffraction grating spectrum," *Philosophical Magazine,* vol. 4, pp. 396-402, 1902.
[75] S. S. Wang, R. Magnusson, J. S. Bagby, and M. G. Moharam, "Guided-mode resonances in planar dielectric-layer diffraction gratings," *JOSA A,* vol. 7, pp. 1470-1474, 1990.
[76] R. Magnusson and S. S. Wang, "New principle for optical filters," *Appl. Phys. Lett.,* vol. 61, p. 1022, 1992.
[77] S. S. Wang and R. Magnusson, "Theory and applications of guided-mode resonance filters," *Appl Opt,* vol. 32, pp. 2606-13, May 10 1993.
[78] W. Suh and F. Shanhui "All-pass transmission or flattop reflection filters using a single photonic crystal slab " *Applied Physics Letters,* vol. 84, pp. 4905-4907, 2004.
[79] A. Rosenberg, M. Carter, J. Casey, M. Kim, R. Holm, R. Henry, C. Eddy, V. Shamamian, K. Bussmann, S. Shi, and D. Prather, "Guided resonances in asymmetrical GaN photonic crystal slabs observed in the visible spectrum," *Optics Express,* vol. 13, pp. 6564-71, Aug 22 2005.
[80] S. Fan and J. D. Joannopoulos, "Analysis of guided resonances in photonic crystal slabs," *Physical Review B,* vol. 65, p. 235112, 2002.
[81] S. Peng and G. M. Morris, "Resonant scattering from two-dimensional gratings," *JOSA A,* vol. 13, pp. 993-1005, 1996.
[82] S. Boonruang, A. Greenwell, and M. G. Moharam, "Multiline two-dimensional guided-mode resonant filters," *Appl Opt,* vol. 45, pp. 5740-7, Aug 1 2006.
[83] E. A. Lidstone, V. Chaudhery, A. Kohl, V. Chan, T. Wolf-Jensen, L. B. Schook, R. Bashir, and B. T. Cunningham, "Label-free imaging of cell attachment with photonic crystal enhanced microscopy," *Analyst,* vol. 136, pp. 3608-15, Sep 21 2011.
[84] M. G. Moharam and T. K. Gaylord, "Rigorous Coupled-Wave Analysis of Planar-Grating Diffraction," *J Opt Soc Am,* vol. 71, pp. 811-818, 1981.

[85] T. L. Frandsen, B. E. Boysen, S. Jirus, M. Spang-Thomsen, K. Dano, and E. W. Thompson, "Experimental models for the study of human cancer cell invasion and metastasis," *Fibrinolysis,* vol. 6, pp. 71-76, 1992.
[86] W. J. Rosoff, J. S. Urbach, M. A. Esrick, R. G. McAllister, L. J. Richards, and G. J. Goodhill, "A new chemotaxis assay shows the extreme sensitivity of axons to molecular gradients.," *Nat Neurosci.,* vol. 7, pp. 678-682, 2004.
[87] Y. D. Su, K. C. Chiu, N. S. Chang, H. L. Wu, and S. J. Chen, "Study of cell-biosubstrate contacts via surface plasmon polariton phase microscopy," *Optics Express,* vol. 18, pp. 20125-35, Sep 13 2010.
[88] A. W. Peterson, M. Halter, A. Tona, K. Bhadriraju, and A. L. Plant, "Surface plasmon resonance imaging of cells and surface-associated fibronectin," *BMC Cell Biol,* vol. 10, p. 16, 2009.
[89] G. Binnig, C. F. Quate, and C. Gerber, "Atomic force microscope," *Phys Rev Lett,* vol. 56, pp. 930-933, Mar 3 1986.
[90] B. Rothenhausler and W. Knoll, "Surface–plasmon microscopy," *Nature,* vol. 332, pp. 615-617, 1988.
[91] M. E. Caldwell and E. M. Yeatman, "Surface-plasmon spatial light modulators based on liquid crystal," *Appl Opt,* vol. 31, pp. 3880-91, Jul 10 1992.
[92] F. Bardin, A. Bellemain, G. Roger, and M. Canva, "Surface plasmon resonance spectro-imaging sensor for biomolecular surface interaction characterization," *Biosens Bioelectron,* vol. 24, pp. 2100-5, Mar 15 2009.
[93] L. S. Jung, C. T. Campbell, T. M. Chinowsky, M. N. Mar, and S. S. Yee, "Quantitative interpretation of the response of surface plasmon resonance sensors to adsorbed films," *Langmuir,* vol. 14, pp. 5636-5648, 1998.
[94] M. Machacek and G. Danuser, "Morphodynamic profiling of protrusion phenotypes," *Biophys J,* vol. 90, pp. 1439-52, Feb 15 2006.
[95] M. Machacek, L. Hodgson, C. Welch, H. Elliott, O. Pertz, P. Nalbant, A. Abell, G. L. Johnson, K. M. Hahn, and G. Danuser, "Coordination of Rho GTPase activities during cell protrusion," *Nature,* vol. 461, pp. 99-103, Sep 3 2009.
[96] J. S. Choi and B. A. Harley, "The combined influence of substrate elasticity and ligand density on the viability and biophysical properties of hematopoietic stem and progenitor cells," *Biomaterials,* vol. 33, pp. 4460-8, Jun 2012.
[97] D. Gupta, H. P. Shah, K. Malu, N. Berliner, and P. Gaines, "Differentiation and characterization of myeloid cells," *Curr Protoc Immunol,* vol. 104, p. Unit 22F 5, 2014.
[98] K. J. Williams, A. A. Picou, S. L. Kish, A. M. Giraldo, R. A. Godke, and K. R. Bondioli, "Isolation and characterization of porcine adipose tissue-derived adult stem cells," *Cells Tissues Organs,* vol. 188, pp. 251-8, 2008.
[99] R. Dariolli, V. Bassaneze, J. S. Nakamuta, S. V. Omae, L. C. G. Campos, and J. E. Krieger, "Porcine Adipose Tissue-Derived Mesenchymal Stem Cells Retain Their Proliferative Characteristics, Senescence, Karyotype and Plasticity after Long-Term Cryopreservation," *Plos One,* vol. 8, p. e67939, 2013.
[100] H. Li, A. Ramachandran, Q. Gao, S. Ravindran, Y. Song, C. Evans, and A. George, "Expression and function of NUMB in odontogenesis," *Biomed Res Int,* vol. 2013, p. 182965, 2013.

[101] S. Kawano, T. Morotomi, T. Toyono, N. Nakamura, T. Uchida, M. Ohishi, K. Toyoshima, and H. Harada, "Establishment of dental epithelial cell line (HAT-7) and the cell differentiation dependent on Notch signaling pathway," *Connect Tissue Res,* vol. 43, pp. 409-12, 2002.
[102] K. T. Thurn, T. Paunesku, A. Wu, E. M. Brown, B. Lai, S. Vogt, J. Maser, M. Aslam, V. Dravid, R. Bergan, and G. E. Woloschak, "Labeling TiO2 nanoparticles with dyes for optical fluorescence microscopy and determination of TiO2-DNA nanoconjugate stability," *Small,* vol. 5, pp. 1318-25, Jun 2009.
[103] D. Ishii, K. Kinbara, Y. Ishida, N. Ishii, M. Okochi, M. Yohda, and T. Aida, "Chaperonin-mediated stabilization and ATP-triggered release of semiconductor nanoparticles," *Nature,* vol. 423, pp. 628-32, Jun 5 2003.
[104] R. A. Sperling, P. R. Gil, F. Zhang, Z. M., and W. J. Parak, "Biological applications of gold nanoparticles," *Chem Soc Rev,* vol. 37, pp. 1896-1908, 2008.
[105] P. M. Winter, A. M. Morawski, S. D. Caruthers, R. W. Fuhrhop, H. Zhang, T. A. Williams, J. S. Allen, E. K. Lacy, J. D. Robertson, G. M. Lanza, and S. A. Wickline, "Molecular Imaging of Angiogenesis in Early-Stage Atherosclerosis With αvβ3-Integrin−Targeted Nanoparticles," *Circulation,* vol. 108, pp. 2270-4, Nov 4 2003.
[106] J. N. Anker, W. P. Hall, O. Lyandres, N. C. Shah, J. Zhao, and R. P. Van Duyne, "Biosensing with plasmonic nanosensors," *Nat Mater,* vol. 7, pp. 442-53, Jun 2008.
[107] A. Mitra, B. Deutsch, F. Ignatovich, C. Dykes, and L. Novotny, "Nano-optofluidic Detection of Single Viruses and Nanoparticles," *ACS Nano,* vol. 4, pp. 1305-1312, Mar 2010.
[108] R. V. Olkhov, J. D. Fowke, and A. M. Shaw, "Whole serum BSA antibody screening using a label-free biophotonic nanoparticle array," *Anal Biochem,* vol. 385, pp. 234-241, Feb 15 2009.
[109] C. Novo, A. M. Funston, and P. Mulvaney, "Direct observation of chemical reactions on single gold nanocrystals using surface plasmon spectroscopy," *Nature Nanotechnology,* vol. 3, pp. 598-602, Oct 2008.
[110] G. J. Nusz, S. M. Marinakos, A. C. Curry, A. Dahlin, F. Hook, A. Wax, and A. Chilkoti, "Label-free plasmonic detection of biomolecular binding by a single gold nanorod," *Analytical Chemistry,* vol. 80, pp. 984-989, Feb 15 2008.
[111] K. M. Mayer, F. Hao, S. Lee, P. Nordlander, and J. H. Hafner, "A single molecule immunoassay by localized surface plasmon resonance," *Nanotechnology,* vol. 21, p. 255503, Jun 25 2010.
[112] K. M. Mayer, S. Lee, H. Liao, B. C. Rostro, A. Fuentes, P. T. Scully, C. L. Nehl, and J. H. Hafner, "A label-free immunoassay based upon localized surface plasmon resonance of gold nanorods," *ACS Nano,* vol. 2, pp. 687-692, Apr 2008.
[113] T. Sannomiya, C. Hafner, and J. Voros, "In situ Sensing of Single Binding Events by Localized Surface Plasmon Resonance," *Nano Lett,* vol. 8, pp. 3450-3455, Oct 2008.
[114] S. M. Marinakos, S. Chen, and A. Chilkoti, "Plasmonic detection of a model analyte in serum by a gold nanorod sensor," *Analytical Chemistry,* vol. 79, pp. 5278-5283, Jul 15 2007.

[115] C. Sonnichsen, B. M. Reinhard, J. Liphardt, and A. P. Alivisatos, "A molecular ruler based on plasmon coupling of single gold and silver nanoparticles," *Nat Biotechnol,* vol. 23, pp. 741-745, Jun 2005.
[116] S. Schultz, D. R. Smith, J. J. Mock, and D. A. Schultz, "Single-target molecule detection with nonbleaching multicolor optical immunolabels," *Proc Natl Acad Sci U S A,* vol. 97, pp. 996-1001, Feb 1 2000.
[117] R. C. Bailey, J. M. Nam, C. A. Mirkin, and J. T. Hupp, "Real-time multicolor DNA detection with chemoresponsive diffraction gratings and nanoparticle probes," *J Am Chem Soc,* vol. 125, pp. 13541-7, Nov 5 2003.
[118] M. F. Miller, B. P. Masters, and M. E. Lundstrom, "Method and apparatus for detection of analyte using a flexural plate wave device and magnetic particles," *US Patent,* vol. US 7300631, p. B2, 2007.
[119] Y. Wang, H. Chen, S. Dong, and E. Wang, "Surface-enhanced Raman scattering of silver-gold bimetallic nanostructures with hollow interiors," *J Chem Phys,* vol. 125, p. 44710, Jul 28 2006.
[120] L. Cognet, C. Tardin, D. Boyer, D. Choquet, P. Tamarat, and B. Lounis, "Single metallic nanoparticle imaging for protein detection in cells," *Proc Natl Acad Sci U S A,* vol. 100, pp. 11350-5, Sep 30 2003.
[121] J. Lee, W. Shen, K. Payer, T. P. Burg, and S. R. Manalis, "Toward attogram mass measurements in solution with suspended nanochannel resonators," *Nano Lett,* vol. 10, pp. 2537-42, Jul 14 2010.
[122] M. R. Lee and P. M. Fauchet, "Nanoscale microcavity sensor for single particle detection," *Opt Lett,* vol. 32, pp. 3284-6, Nov 15 2007.
[123] J. Zhu, S. K. Ozdemir, Y. Xiao, L. Li, L. He, D. Chen, and L. Yang, "On-chip single nanoparticle detection and sizing by mode splitting in an ultrahigh-Q microresonator (vol 4, pg 46, 2010)," *Nature Photonics,* vol. 4, pp. 46-49, Feb 2010.
[124] A. Gupta, D. Akin, and R. Bashir, "Single virus particle mass detection using microresonators with nanoscale thickness," *Applied Physics Letters,* vol. 84, pp. 1976-1978, Mar 15 2004.
[125] M. L. Juan, R. Gordon, Y. Pang, F. Eftekhari, and R. Quidant, "Self-induced back-action optical trapping of dielectric nanoparticles," *Nat Phys,* vol. 5, pp. 915-919, 2009.
[126] A. Kotnala, D. DePaoli, and R. Gordon, "Sensing nanoparticles using a double nanohole optical trap," *Lab on a Chip,* vol. 13, pp. 4142-4146, 2013.
[127] S. Nie and S. R. Emory, "Probing single molecules and single nanoparticles by surface-enhanced Raman scattering," *Science,* vol. 275, pp. 1102-1106, Feb 21 1997.
[128] W. Zhang, L. Huang, C. Santschi, and O. J. F. Martin, "Trapping and Sensing 10 nm Metal Nanoparticles Using Plasmonic Dipole Antennas," *Nano Lett,* vol. 10, pp. 1006-1011, Mar 10 2010.
[129] S. Wang, X. Shan, U. Patel, X. Huang, J. Lu, J. Li, and N. Tao, "Label-free imaging, detection, and mass measurement of single viruses by surface plasmon resonance," *Proc Natl Acad Sci U S A,* vol. 107, pp. 16028-32, Sep 14 2010.

[130] J. O. Grepstad, P. Kaspar, O. Solgaard, I. R. Johansen, and A. S. Sudbo, "Photonic-crystal membranes for optical detection of single nano-particles, designed for biosensor application," *Optics Express,* vol. 20, pp. 7954-7965, Mar 26 2012.
[131] R. Vedula, G. Daaboul, A. Reddington, E. Ozkumur, D. A. Bergstein, and M. S. Unlu, "Self-referencing substrates for optical interferometric biosensors," *J Mod Opt,* vol. 57, pp. 1564-1569, Sep 20 2010.
[132] G. G. Daaboul, A. Yurt, X. Zhang, G. M. Hwang, B. B. Goldberg, and M. S. Unlu, "High-throughput detection and sizing of individual low-index nanoparticles and viruses for pathogen identification," *Nano Lett,* vol. 10, pp. 4727-31, Nov 10 2010.
[133] M. R. Monroe, G. G. Daaboul, A. Tuysuzoglu, C. A. Lopez, F. F. Little, and M. S. Unlu, "Single nanoparticle detection for multiplexed protein diagnostics with attomolar sensitivity in serum and unprocessed whole blood," *Analytical Chemistry,* vol. 85, pp. 3698-706, Apr 2 2013.
[134] S. Person, B. Deutsch, A. Mitra, and L. Novotny, "Material-specific detection and classification of single nanoparticles," *Nano Lett,* vol. 11, pp. 257-61, Jan 12 2011.
[135] P. E. Sheehan, L. J. Whitman, W. P. King, and B. A. Nelson, "Nanoscale deposition of solid inks via thermal dip pen nanolithography " *Applied Physics Letters,* vol. 85, pp. 1589-1591, Aug 2004.
[136] J. R. Felts, S. Somnath, R. H. Ewoldt, and W. P. King, "Nanometer-scale flow of molten polyethylene from a heated atomic force microscope tip," *Nanotechnology,* vol. 23, p. 215301, Jun 1 2012.
[137] H. Hu, P. K. Mohseni, L. Pan, X. Li, S. Somnath, J. R. Felts, M. A. Shannon, and W. P. King, "Fabrication of arbitrarily-shaped silicon and silicon oxide nanostructures using tip-based nanofabrication," *J Vac Sci Technol B,* vol. 31, p. 06FJ01, 2013.
[138] W. P. King, B. Bhatia, J. R. Felts, H. J. Kim, B. Kwon, B. Lee, S. Somnath, and M. Rosenberger, "Heated Atomic Force Microscope Cantilevers and their Applications," *Annu Rev Heat Transfer,* vol. 16, pp. 287-326, 2013.
[139] K. Yu, Y. Tian, and T. Tatsuma, "Size effects of gold nanaoparticles on plasmon-induced photocurrents of gold-TiO2 nanocomposites," *Phys Chem Chem Phys,* vol. 8, pp. 5417-5420, Dec 14 2006.
[140] R. S. Yalow and S. A. Berson, "Immunoassay of endogenous plasma insulin in man," *J Clin Invest,* vol. 39, pp. 1157-75, Jul 1960.
[141] S. X. Leng, J. E. McElhaney, J. D. Walston, D. Xie, N. S. Fedarko, and G. A. Kuchel, "ELISA and multiplex technologies for cytokine measurement in inflammation and aging research," *J Gerontol A Biol Sci Med Sci,* vol. 63, pp. 879-84, Aug 2008.
[142] C. Dass, " Fundamentals of Contemporary Mass Spectrometry," *John Wiley & Sons,* p. p.5, 2007.
[143] H. Lilja, D. Ulmert, and A. J. Vickers, "Prostate-specific antigen and prostate cancer: prediction, detection and monitoring," *Nat Rev Cancer,* vol. 8, pp. 268-78, Apr 2008.

[144] F. Riedel, I. Zaiss, D. Herzog, K. Gotte, R. Naim, and K. Hormann, "Serum levels of interleukin-6 in patients with primary head and neck squamous cell carcinoma," *Anticancer Res,* vol. 25, pp. 2761-5, Jul-Aug 2005.
[145] S. F. Kingsmore, "Multiplexed protein measurement: technologies and applications of protein and antibody arrays," *Nat Rev Drug Discov,* vol. 5, pp. 310-20, Apr 2006.
[146] T. I. Williams, K. L. Toups, D. A. Saggese, K. R. Kalli, W. A. Cliby, and D. C. Muddiman, "Epithelial ovarian cancer: disease etiology, treatment, detection, and investigational gene, metabolite, and protein biomarkers," *J Proteome Res,* vol. 6, pp. 2936-62, Aug 2007.
[147] A. M. Ward, J. W. Catto, and F. C. Hamdy, "Prostate specific antigen: biology, biochemistry and available commercial assays," *Ann Clin Biochem,* vol. 38, pp. 633-51, Nov 2001.
[148] J. F. Rusling, C. V. Kumar, J. S. Gutkind, and V. Patel, "Measurement of biomarker proteins for point-of-care early detection and monitoring of cancer," *Analyst,* vol. 135, pp. 2496-511, Oct 2010.
[149] R. D'Agata and G. Spoto, "Surface plasmon resonance imaging for nucleic acid detection," *Anal Bioanal Chem,* vol. 405, pp. 573-84, Jan 2013.
[150] R. Gans, "Über die Form ultramikroskopischer Goldteilchen," *Annalen der Physik,* vol. 342, pp. 881-900, 1912.
[151] K. M. Mayer and J. H. Hafner, "Localized surface plasmon resonance sensors," *Chem Rev,* vol. 111, pp. 3828-57, Jun 8 2011.
[152] S. Link, M. B. Mohamed, and M. A. El-Sayed, "Simulation of the Optical Absorption Spectra of Gold Nanorods as a Function of Their Aspect Ratio and the Effect of the Medium Dielectric Constant," *J. Phys. Chem. B,* vol. 103, pp. 3073-3077, 1999.
[153] A. Brioude, X. C. Jiang, and M. P. Pileni, "Optical Properties of Gold Nanorods: DDA Simulations Supported by Experiments," *J. Phys. Chem. B,* vol. 109, pp. 13138-13142, 2005.
[154] L. Tian, E. Chen, N. Gandra, A. Abbas, and S. Singamaneni, "Gold Nanorods as Plasmonic Nanotransducers: Distance-Dependent Refractive Index Sensitivity," *Langmuir,* vol. 28, pp. 17435-17442, Dec 18 2012.
[155] L. Tian, J. J. Morrissey, R. Kattumenu, N. Gandra, E. D. Kharasch, and S. Singamaneni, "Bioplasmonic paper as a platform for detection of kidney cancer biomarkers," *Analytical Chemistry,* vol. 84, pp. 9928-9934, 2012.
[156] S. George, V. Chaudhery, M. Lu, M. Takagi, N. Amro, A. Pokhriyal, Y. Tan, P. Ferreira, and B. T. Cunningham, "Sensitive Detection of Protein and miRNA Cancer Biomarkers using Silicon-Based Photonic Crystals and A Resonance Coupling Laser Scanning Platform," *Lab on a Chip,* vol. 13, pp. 4053-4064, 2013.